

Nina Borsheim

Ammonia Spray Characterization

Experimental Investigation of Ammonia as Fuel
in Internal Combustion Engines

Master's thesis in Mechanical Engineering

Supervisor: Terese Løvås

Co-supervisor: Karl Oskar Pires Bjørgen

June 2023

Nina Borsheim

Ammonia Spray Characterization

Experimental Investigation of Ammonia as Fuel in
Internal Combustion Engines

Master's thesis in Mechanical Engineering
Supervisor: Terese Løvås
Co-supervisor: Karl Oskar Pires Bjørgen
June 2023

Norwegian University of Science and Technology
Faculty of Engineering
Department of Energy and Process Engineering



Problem Description

Injecting ammonia directly into the cylinder raises research questions related to the internal fluid flow of ammonia in the injector, where cavitation can occur, potentially deteriorating the discharge coefficient of the nozzle. Furthermore, the ammonia spray is affected by the internal flow pattern, thereby affecting the mixing with air inside the cylinder and the combustion process. This is important information needed as input to numerical simulations of ammonia combustion in engines. This master thesis will focus on characterizing ammonia injection under engine-like conditions. The primary objective of the master thesis is to measure the mass flux and momentum flux through a GDI injector injecting liquid ammonia. The subsequent objective is to investigate liquid ammonia sprays in the constant volume chamber.

- Conducting a literature review for ammonia sprays in engine applications and the methods used.
- Preparing the experimental equipment for measuring the momentum flux of an ammonia injection.
- Preparing equipment for measuring the injected mass per injection.
- Comparing results with numerical simulation performed by the group.

Abstract

Increasing awareness of the consequences of pollution and a desire to decarbonise internal combustion engines (ICE) have made ammonia a fuel of interest for the shipping industry. To optimize the ICE performance, it is necessary to investigate the behaviour of ammonia out of the injector. Due to the high vapour pressure of ammonia compared to carbon-based fuels, an increased tendency of cavitation in the injector nozzle is expected [1]. Cavitation is predicted to limit the injected mass of ammonia and give ammonia a different spray behaviour out of the injector. To this date, there is little experimental data on this subject, and further investigation into fuel characterisation is needed.

This master thesis is part of a larger study where the main objective is to develop a deeper understanding of the characteristics of liquid ammonia sprays, with the experimental investigation to support numerical simulations. In this thesis, the spray characteristics of ammonia through a Gasoline Direct Injection (GDI) injector into a high-pressure chamber filled with nitrogen were investigated.

The momentum flux, injected ammonia mass, instantaneous mass flow, discharge coefficient, spray angle, spray penetration length and spray penetration velocity have been measured and examined. The momentum flux was obtained using a force transducer, and the injected mass was found by including a weight in the ammonia fuel system. From the results obtained, an increase in ambient pressure from 2 bar to 20 bar resulted in a decrease in the discharge coefficient from 0.56 to 0.51 for an injection pressure of 200 bar. The spray behaviour out of the injector was captured using the shadowgraph imaging technique. The spray penetration length and velocity were found to be highly dependent on the chamber pressure, with an increasing ambient density resulting in a lower spray penetration velocity. The flash boiling conditions also influenced the spray behaviour, where at flare flashing conditions, the shape of the spray changed significantly. The angle of the ammonia spray out of the injector was found to be dependent on the flash boiling conditions.

Sammendrag

Det er et økende fokus på å få ned klimautslipp, og et ønske om å minske forurensning knyttet til transport og forbrenning. Dette har gjort ammoniakk til et potensielt lovende karbonfritt drivstoff for forbrenningsmotoren, særlig innen skipsfart.

Per nå er det lite informasjon hvordan ammoniakk oppfører seg i forbrenningsmotoren, spesielt oppførselen ut av injektoren. Det er forventet en høyere grad av kavitasjon gjennom injektoren grunnet ammoniakks høye fordampningstrykk, som videre er forventet å påvirke spray-oppførselen og mengden masse injisert. For å optimalisere motorytelsen er det av interesse å undersøke strømmingen av ammoniakk ut av injektoren, hvor det for øyeblikket er lite eksperimentelle data.

Denne masteroppgaven er en del av en større studie hvor formålet er å oppnå en bedre forståelse av egenskapene til flytende ammoniakk-spray, hvor eksperimentelle resultater skal støtte opp numeriske simuleringer. I dette eksperimentelle arbeidet har egenskapene til ammoniakk blitt undersøkt i et høytrykkskammer, hvor ammoniakk har blitt testet under ulike kammertrykk og injeksjonstrykk. En kraftsensor, vekt og høyhastighets-kamera har blitt benyttet under forsøkene. Sprayens kraft, moment, hvor mye masse som injiseres, massefluks, sprayform, spraylengde, sprayens hastighet og vinkel er egenskaper som har blitt undersøkt.

Resultater fra denne oppgaven viser at et økende kammertrykk fra 2 bar til 20 bar gir en lavere C_d (Discharge coefficient) fra 0.56 til 0.51, ved et injeksjonstrykk på 200 bar. Det er også vist en sammenheng mellom spraylengde og kammertrykk, hvor et høyere kammertrykk gir en lavere hastighet av sprayen. Sprayens oppførsel ble også påvirket av fenomenet flash boiling, hvor spray-formen ble betydelig påvirket ved lavere kammertrykk.

Preface

This thesis is the conclusion of a five-year Master's program in Mechanical Engineering, with a specialization in Energy and Process Engineering at the Norwegian University of Science and Technology.

I want to extend my sincerest gratitude to Karl Oskar Pires Bjørgen, a postdoctoral researcher at NTNU. Without him, not a single aspect of this thesis would have been accomplished. I would also like to thank my other supervisor, Terese Løvås, for her continuous availability and guidance.

I would like to thank my classmates for engaging and supportive conversations. Finally, I would like to thank my partner Trond Oftedal Veggeberg for his moral support, for reading through my work and for advising me on language and writing techniques.

Contents

Nomenclature

1	Introduction	1
1.1	Objective	2
1.2	Previous work	2
1.3	Thesis structure	3
2	Theory	4
2.1	Internal Combustion Engines	4
2.2	Ammonia	5
2.3	Ammonia for Power	6
2.4	Cavitation	8
2.5	Optical diagnostic	9
2.6	Momentum flux	11
3	Methodology	15
3.1	High-pressure chamber	15
3.2	GDI Injector	16
3.3	Operating conditions	17
3.4	Ammonia fuel system	18
3.4.1	Charging the system	19
3.4.2	Discharging the system	21
3.5	Momentum Test Rig	22
3.5.1	Piezoelectric force transducer	22
3.5.2	Testing different spray target sizes	24
3.5.3	Testing spray target at different positions	25
3.6	Mass flux	26
3.7	Shadowgraph	28
3.8	Camera	31

3.8.1	Momentum flux	32
3.8.2	Shadowgraph	32
3.9	Post-processing	32
3.9.1	Momentum flux	32
3.9.2	Mass flux	34
3.9.3	Shadowgraph imaging	34
3.10	Single-hole GDI	36
4	Results and Discussion	38
4.1	Momentum Flux	38
4.2	Alignment of the Piezoelectric Sensor	41
4.2.1	Spray target size	41
4.2.2	Effect of distance to the spray target	43
4.2.3	Effect of spray target angle	44
4.3	Momentum flux results	46
4.3.1	Varying the injection pressure	46
4.3.2	Varying the ambient pressure	48
4.3.3	Injection energizing	49
4.3.4	Injection timing and delay	50
4.4	Mass injected	52
4.5	Mass flux and discharge coefficient	54
4.6	Shadowgraph imaging	56
4.6.1	Spray shapes	57
4.6.2	Spray penetration length and velocity	61
4.6.3	Angle of spray out of injector	65
4.6.4	Spray angle at half penetration length	67
5	Conclusion	71
6	Further Work	73
	References	76

List of Figures

1	Illustration of Port Fuel Injection and Gasoline Direct Injection.	5
2	Illustration of the fluid flow through the nozzle hole with cavitation.	8
3	Illustration of flash boiling and its effect on spray behaviour, from	10
4	Arbitrary flow profile [2].	12
5	Simplification of flow profile [2].	12
6	Illustration of the control volume for the momentum flux measurements. P_{inj} = injection pressure, P_{amb} = ambient pressure, CV = control volume, \dot{M} = the momentum flux of the spray, F = measured force.	13
7	Illustration of the high-pressure chamber.	15
8	Pictures of the cross-section of the GDI injector obtained through CT scanning	17
9	P&ID diagram of the ammonia fuel system.	20
10	Illustration of the spray momentum rig.	23
11	Illustration of the force transducer set-up with the spray target presented to the emerging fuel spray.	25
12	Picture of the camera settings used to ensure that the piezoelectric sensor remained in the same position when changing spray targets.	26
13	Illustration of the components shown in Figure 12, with labels	26
14	Illustration and pictures of varying position of spray target.	27
15	Illustration of injected mass measurements.	28
16	Illustration of the optical setup.	29
17	Picture demonstrating the double image effect during misalignment.	30
18	Pictures from the shadowgraph setup.	31
19	Post-processing of shadowgraph with liquid ammonia spray at an injection pressure of 100 bar and ambient pressure of 10 bar as an example.	35
20	Definition of spray characteristic for the ammonia spray.	35
21	Pictures of the GDI injector.	37
22	Spray Momentum.	38

23	Ammonia spray development out of the injector, with a spray target presented to the emerging spray.	39
24	Graphs representing the average of 15 injections with an injection duration of 1 ms, p_{inj} at 200 bar and p_{amb} at 2 bar.	40
25	Graphs representing the average of 15 injections with an injection duration of 1 ms, p_{inj} at 200 bar and p_{amb} at 2 bar.	41
26	Graphs representing measurements performed with different target sizes, where each graph is calculated for a single hole of the GDI injector at a target size ranging from 4 mm to 9 mm.	42
27	Momentum results from varying the distance between the spray target and injector tip. Each point represents one position, which is the average of 15 injections in the given position, for $p_{inj} = 205$ bar, $p_{amb} = 2$ bar. A line is included to show the maximum momentum obtained.	44
28	Momentum results from varying the angle of the spray target relative to the injector tip. Each point represents one position, taking an average of 15 injections of said position, for $p_{inj} = 200$ bar, $p_{amb} = 2$ bar. The graph includes $M_{max} \sin(\beta)$: the theoretical measurement of the momentum, and the green point represents M_{max}	45
29	Varying the angle of the sensor relative to the spray, β , from a steep (a) to a perpendicular (b) to an obtuse (c) angle. In the figures, vector S is equal to the actual momentum flux of the spray, and F equals the momentum flux measured by the piezoelectric sensor.	45
30	Graphs representing the average of 15 injections with an injection duration of 1 ms and p_{amb} at 2 bar, with varying injection pressure.	46
31	Graphs representing the average of 15 injections with an injection duration of 1 ms and p_{inj} at 200 bar, with varying ambient pressure.	48
32	Spray momentum flux at different energizing durations, varying from 1 ms to 3 ms.	50
33	Graphs to review any correlations between delay and chamber pressure or injection pressure.	52

34	Pictures from shadowgraph imaging at the end of injection.	53
35	The injected mass of ammonia, where each of the coloured markers represents the average injected mass for 500 injections. One exception of the black point which represents the average of 2500 injections	54
36	Graphs showing calculations of mass flow rate and discharge coefficient for $p_{inj}=200$ bar with a chamber pressure at 2 bar, 10 bar and 20 bar.	55
37	Pictures of the injector orientation.	57
38	Summary of the different spray shapes for the different flash boiling conditions: flare flashing, transitional flashing, initial flashing and above critical conditions. All pictures are for an injection pressure of 200 bar at 0.5 ms after SOI.	61
39	Example from the post-processing of the spray penetration length for an injection pressure of 200 bar at 0.25 ms after SOI, at different ambient pressures.	62
40	The spray penetration length and velocity of ammonia at different ambient pressures for an injection pressure of 200 bar.	63
41	Illustration of the spray post-processing, for chamber pressures of 2 bar and 4 bar, at 0.13 ms and 0.25 ms after SOI. In the pictures, to achieve a higher sensitivity of the spray penetration length, the length has the unit of pixel lengths.	65
42	Example from the post-processing of the angle of the spray near the injector at an injection pressure of 200 bar at 3.0 ms after SOI, at different ambient pressures.	66
43	Graphs representing the spray angle near the injector. Here, the x-axis shows the ambient pressure, the y-axis is the angle in degrees. The three graphs represent the angles for different moments of the injection, 1 ms, 3 ms and 5 ms after the start of injection.	66
44	Spray angle at half penetration length at an injection pressure of 200 bar. The actual measurements in the background of the plots.	68

45	Pictures to explain the fluctuating tendency of the curve for fully flashing spray in Figure 44. The pictures portray the spray at a chamber pressure of 1 bar and injection pressure of 200 bar, displaying how the vapour zone with droplets surrounding the liquid core periodically gets detected in the script. The pictures are at different instants after the start of energizing, from 1.25 ms to 3.25 ms after SOI.	69
46	Picture of the high-pressure chamber during the momentum flux testing. Showing the position of the camera and the LED light.	83
47	Picture of the high-pressure chamber during the momentum flux testing. Showing the position of the camera and the LED light.	84
48	Pictures of the cylindrical fuel tank on the weight (to the left), the ammonia supply tank (grey in the centre) and the nitrogen supply tanks (blue and black, to the right).	84
49	Pictures of the injector employed.	85
50	Picture of the different spray targets.	85
51	Pictures of some leakages that occurred during testing: a leakage from the single-hole GDI, an initial leakage from the high-pressure chamber (found by using soap water and later fixed), and a smaller leakage from the cable to the force transducer (found by using soap water).	86

List of Tables

1	Thermophysical properties of ammonia, diesel and iso-octane ((a) in liquid phase, (b) at 20°C, (c) boiling point for hydrocarbons C9-C20, (d) at 15°C).	6
2	The measured dimension of the GDI injector using CT images	16
3	Key parameters of the experimental conditions.	18
4	Equipment employed in shadowgraph imaging.	29
5	Summary of the camera settings.	32
6	Comparison of spray shape at 0.25 ms, 0.5 ms, 0.75 ms, 1 ms, 3 ms and 5 ms after the start of injection (SOI) for an injection pressure of 200 bar.	58
7	Comparison of spray shape at 0.25 ms, 0.5 ms, 0.75 ms, 1 ms, 3 ms and 5 ms after the start of injection (SOI) for an injection pressure of 100 bar.	59

Nomenclature

Abbreviations

AFR	Air-fuel ratio
ASE	After the start of energizing
CO	Carbon monoxide
DI	Direct injection
EOI	End of injection
fsp	Frames per second
GDI	Gasoline direct injection
ICE	Internal combustion engine
IMO	International Maritime Organization
LED	Light-emitting diode
NTNU	Norwegian University of Science and Technology
NO _x	Nitrogen oxides
PM	Particulate matter
P&ID	Piping and instrumentation
PFI	Port fuel injection
$\frac{1}{2}$ SP	Half penetration length
RCCI	Reactivity-controlled compression ignition
R _p	Saturation-to-ambient pressure ratio
SOI	Start of injection
SP	Penetration length

Symbols

A	Area
A	Area differential
ΔP	Change in pressure
ρ	Density
Cd	Discharge coefficient
F	Force
\dot{M}	Momentum flux
P	Pressure
P _{amb}	The ambient pressure
P _{inj}	The injection pressure
\dot{m}	The instantaneous mass flow rate
Δt	Time step
u	Velocity
dV	Volume differential

1 Introduction

Growing awareness of the consequences of pollution and greenhouse emissions is a driving force to change the transportation sector. There is an increasing focus on reducing carbon emissions and utilizing carbon-free fuels instead of fossil fuels. This has pushed the maritime industry to search for new combustion systems, where ammonia is a fuel of interest to enable the decarbonization of internal combustion engines (ICE).

Ammonia contains a large amount of hydrogen, with hydrogen constituting approximately 17.7% of ammonia by weight. Ammonia is liquefied at moderate temperatures and low pressures, making it easier to store and transport compared to other carbon-free fuels such as hydrogen [3]. These storage capabilities, combined with having a high hydrogen content with no carbon, make ammonia a promising fuel for ICE.

Several engine manufacturers are currently working on concepts implementing ammonia as fuel in ICEs [4] [5] [6]. One of these concepts is based on utilizing a high-pressure multi-hole injector to directly inject the ammonia into the engine cylinder. By employing a direct injection technique, there is no need to evaporate ammonia prior to injection. Hence, the hypothesis is the unburned ammonia emissions will decrease compared to port-injected ammonia, where premixed air-fuel combustion leads to a higher degree of flame quenching on the engine walls and ammonia mass trapped in the crevices [7] [8] [9]. Additionally, by employing direct injection, more options to fuel mixing are possible, where premixed, partially premixed and non-premixed combustion can be achieved depending on the energy ratio of ammonia and diesel.

However, there are challenges in employing ammonia as fuel in ICEs related to its poor combustion properties, having a high ignition energy and temperature, low flame speed and low adiabatic flame temperature in comparison to diesel [7]. Additionally, ammonia has a different fuel behaviour related to its higher volatility, lower viscosity and high vapour pressure, which is expected to influence its behaviour through the injector nozzle and in the chamber.

1.1 Objective

Investigation into the behaviour of ammonia out of the injector is of interest to optimize the ICE performance. Having little experimental data on this subject, a deeper investigation into fuel characterization is needed.

This master thesis presents the experimental results to give a better understanding of the internal flow through a Gasoline Direct Injection (GDI) injector operating with ammonia. The project explores the use of rate of momentum to characterize the internal flow, which is important for predicting the mixing potential of the injection process. When combined with mass measurements, it is possible to compute the nozzle performance under different conditions. Additionally, shadowgraph has been employed to investigate the spray characteristics optically, acquiring the spray angle, spray penetration length and spray penetration velocity under non-flash and flash boiling conditions. Finding these parameters is a motivation for the study, as they are significant for engine performance and pollutant formation. This thesis fits into a larger study where the main objective is to develop a better understanding of the characteristics of liquid ammonia sprays, with the experimental investigation to support the numerical simulations.

The thesis focuses on the experimental setup and uncertainties in the results. The experiments are conducted in a high-pressure chamber filled with nitrogen. A force transducer is used to measure the force out of the nozzle, a weight is added to the ammonia fuel system to measure the injected mass and the spray behaviour is captured using a high-speed camera system. The test rig was first set with nitrogen before being operated with ammonia.

1.2 Previous work

This master thesis is a continuation of the project thesis, submitted in the fall of 2022. In the project thesis, a single-hole GDI injector was investigated. A literature review was conducted, the experimental equipment for the momentum flux measurements was assembled, and the post-processing methodology for the momentum flux was initiated. First, the rig was operated using decane before changing the fuel to ammonia. When operating with ammonia, it was discovered the single-hole GDI was unable to seal; hence a leakage occurred. Due to

this leakage, only one experiment was executed using ammonia, and no measurements were obtained for injected ammonia mass.

1.3 Thesis structure

The thesis begins with a theoretical background where relevant equations are presented. In the following section, the methods for the experiments are explained with the given equipment and techniques before presenting the results with a discussion. The final section draws conclusions gathered throughout the project and provides recommendations for future work. Considering the master thesis is a continuation of the project thesis, some of the sections are similar for both theses [10].

2 Theory

A description of the relevant theoretical background will be made in this chapter. Considering the master thesis is a continuation of the project thesis, some of the sections are similar for both theses [10].

2.1 Internal Combustion Engines

An increasing focus on emission control has resulted in intensive research to optimize the efficiency of combustion engines. The most common injection system for Otto engines is Port Fuel Injection (PFI), however, the use of Gasoline Direct Injection (GDI) engines is expected to grow over the years [2]. In Figure 1, illustrations of the injection systems are displayed, with the injector highlighted in pink. As portrayed to the left in the figure, the fuel is injected into the intake port for PFI engines. Having combustion of an air-fuel homogeneous mixture at relatively low temperatures, the PFI engines typically release less toxic emissions and pollutants [11]. With strict emission regulations for engines and a desire to enhance efficiency, performance and fuel economy, GDI systems are viewed as the successor.

In GDI engines, the fuel is injected directly into the combustion chamber, as depicted to the right in Figure 1. Without the need to pump fuel into the intake port, pumping and mechanical losses are reduced significantly, resulting in the fuel being used more efficiently [2]. In GDI engines, the fuel is injected at a higher pressure, making fuel droplet sizes significantly smaller than for PFI engines, resulting in an enhanced liquid-air interface. Consequently, GDI engines deliver a higher power output for the same amount of fuel. However, GDI systems have drawbacks such as emissions, complexity and costs, and to overcome the deficiencies and challenges, a fundamental understanding of all characteristics of the spray, fuel development and interaction between the main affecting parameters has to be gained.

If ammonia is employed in shipping, it would possibly require the use of a diesel injector due to the higher pressures involved. However, since this technology has not yet been developed, it presents a greater level of uncertainty regarding its implementation. GDI injectors can be operated at lower fuel pressures than diesel injectors, and there is no return line for the fuel. Consequently, due to practicality, a GDI injector has been chosen for this project.

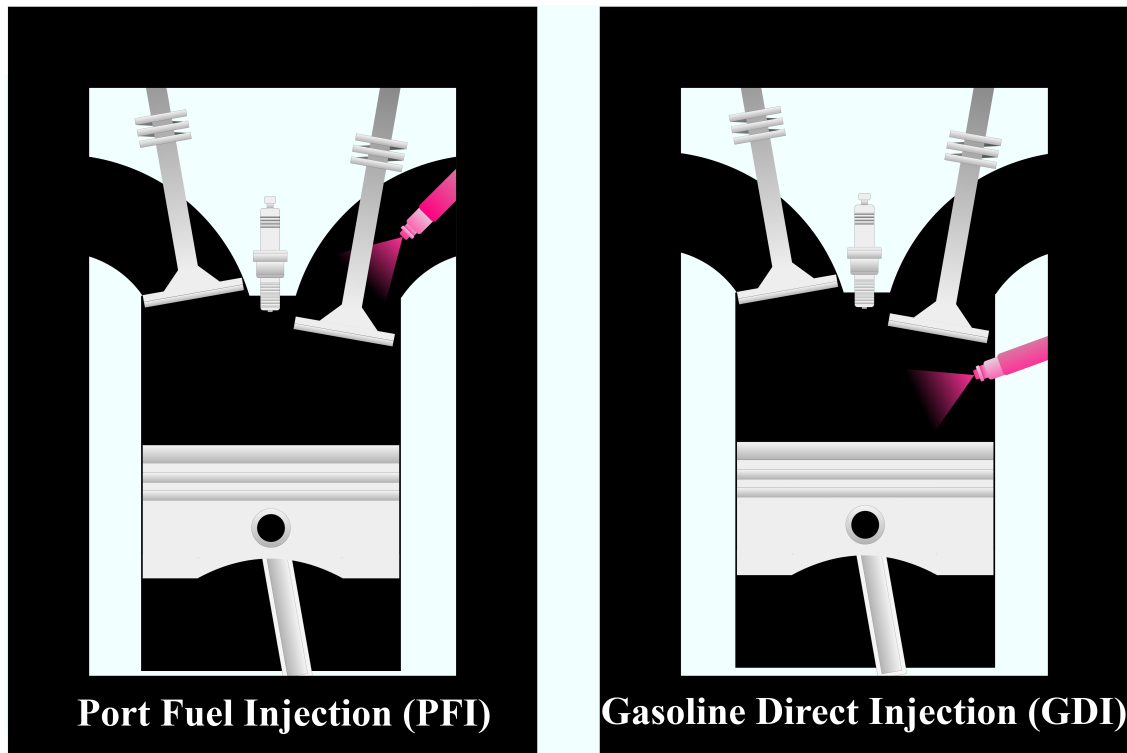


Figure 1: Illustration of Port Fuel Injection and Gasoline Direct Injection.

2.2 Ammonia

The IMO (International Maritime Organization) 2023 regulation focuses on vessel efficiency and carbon emissions [12]. It is part of the International Maritime Organization’s Greenhouse Gas Strategy (GHG) working on a reduction of ocean freight carbon emissions. To reach these ambitions, technical and operational energy efficiency measures will be essential, but not adequate by themselves. Consequently, low-carbon or carbon-free fuels need to be implemented in the fuel mix, where ammonia has attracted wide interest as a carbon-free fuel.

Ammonia is an inorganic compound of nitrogen and hydrogen, with the chemical formula NH_3 . Ammonia contains a large amount of hydrogen, where hydrogen constitutes approximately 17.7% by weight. It is liquefied at moderate temperatures and low pressures: at atmospheric pressure, ammonia turns liquid at -33.3°C , while at ambient temperatures of 20°C , ammonia turns liquid at 8.57 bar. Having these properties makes ammonia easier to store compared to other carbon-free fuels such as hydrogen, hence the cost of storage per energy unit is significantly cheaper.

The thermophysical properties of ammonia are summarized in Table 1. Diesel is included in the table as an example of conventional fuel, while iso-octane is included as a reference GDI fuel, as it has been investigated in several previous studies [13][14]. From the table, it is noted that ammonia has a significantly lower boiling point than the other fuels, at a temperature below ambient conditions. It is also observed that ammonia has under half of the lower heating value of the other fuels, while five times higher latent heat of vaporization. However, ammonia has a much lower stoichiometric air-to-fuel ratio (AFR), at less than half of the AFR of diesel. This implies that given the same amount of air, the total energy output would be comparable for both fuels.

Table 1: Thermophysical properties of ammonia, diesel and iso-octane ((a) in liquid phase, (b) at 20°C, (c) boiling point for hydrocarbons C9-C20, (d) at 15°C). [15][16][17][18] [19]

Fuel type	Ammonia	Diesel	Iso-octane
Chemical formula	NH ₃	-	C ₈ H ₁₈
Density [kg/m ³]	602.8 ^(a)	830 ^(b)	698 ^(d)
Lower heating value [MJ/kg]	18.6	42.5	44.6
Latent heat of vaporization [kJ/kg]	1270	250	272
Cetane Number	-	≥49	-
Ignition temperature [°C]	651	210	530
Stoichiometric air-fuel ratio (AFR)	6.1	14.3	14.7
Boiling point [°C]	-33.3	163-357 ^(c)	99.2
Vapour pressure [bar]	8.57 ^(b)	-	-

2.3 Ammonia for Power

In ICE so far, most ammonia applications have been executed using PFI, with ammonia in the gaseous phase being premixed with air [20][21][22], also known as reactivity-controlled compression ignition (RCCI), or low pressure dual fuel (LPDF) engine. As mentioned in section 2.1, injecting fuel directly can improve efficiency due to better filling. Regarding ammonia application, this could potentially reduce ammonia slip: giving less unburned ammonia in the exhaust [23]. Using a direct injection (DI) with ammonia in a liquid phase, ammonia must either be pressurized to approximately 9 bar (at ambient temperature) or cooled down to temperatures below -34 °C (at ambient pressure), referring to Table 1. Direct injection of ammonia can affect the engine stability due to the decrease of in-cylinder temperature

[1]. Research suggests that a low in-cylinder temperature combined with ammonia's high resistance to auto-ignition can result in a delayed start of combustion, and further, unsuccessful combustion causing a high amount of unreacted species such as NO, CO and PM [24]. Another concern with ammonia as a fuel for ICEs is related to the high saturation pressure, hence, flash boiling may occur: when a subcooled liquid is rapidly depressurized to a pressure below its liquid saturation pressure [1].

Having both low specific energy and low laminar burning velocity, combined with high auto-ignition temperature and elevated ignition energy, makes ammonia difficult to burn in pure form. Thus, studies have suggested that ammonia needs to be mixed with other fuels as combustion promoters to make it a viable fuel for ICEs [25]. Projects exploring this dual-fuel approach show that ammonia-fueled engines have low power losses, while no more corrosion or higher consumption of lubricant than conventional fuels.

Modifying a diesel ICE to a combination of diesel and ammonia, with diesel acting as the combustion promoter, has shown promising results. Results from studies gathered by Valera-Medina et al. show that peak engine torque could be achieved by using different combinations of diesel and ammonia [25]. From these reports, the same torque output was achieved for a systematic ammonia increase, leading to a monotonic CO₂ reduction. In addition, for fuel mixtures not exceeding 60 per cent ammonia as energy substitution, lower NO_x emissions were measured [26].

For determining engine performance and emission control in diesel engines, injection strategies including injection timing and pressure play an important role [27]. It is reported that early injection causes lower soot and higher NO_x emissions than a late injection. By having advanced injection timing and high fuel injection pressure, more efficient and cleaner combustion can be obtained [28], and employing an advanced start of injection with engines operating with ammonia, the major benefit of complete combustion of the ammonia is reported [15]. Consequently, having an understanding of the timing and delays of the current injector is of interest.

To implement ammonia in power devices, a further understanding of its combustion behaviour is needed. Therefore, a deeper understanding of ammonia spray characteristics and internal flow behaviour through a GDI injector is required to optimize the ICE performance.

2.4 Cavitation

In primary spray breakup and development processes, cavitation and turbulence inside the injector play a critical role. Hence, to capture the injection process with accuracy, it is important to understand the cavitation phenomenon. Cavitation is the phase transition of fluid from liquid to vapour due to low pressure. For the injector, cavitation will likely appear in the inlet of the nozzle hole due to the sharp edges, significant change in cross-section and change in flow direction [29].

Figure 2 shows a simplified sketch of the fluid flow through the injector nozzle hole. In the figure, the vena contracta is noted as being the point in a fluid stream where the diameter is the least and fluid velocity is at its highest [29]. According to the Bernoulli principle, this causes a reduction in the local static pressure. Thus, due to the acceleration of the fluid, a pressure depression occurs, making this the point in the nozzle where the vapour recirculation zone will appear. If the static pressure falls below the vapour pressure of the fluid, cavitation will appear, giving a vapour zone as illustrated in Figure 2.

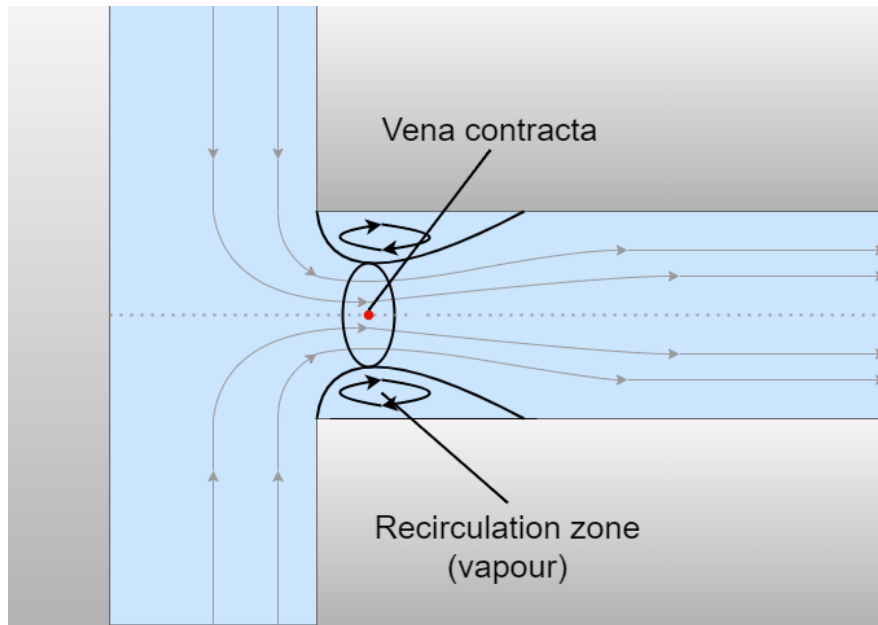


Figure 2: Illustration of the fluid flow through the nozzle hole with cavitation.

Consequently, due to this cavitation phenomenon, cavitation bubbles can be formed inside the nozzle, and be injected into the combustion chamber. As mentioned in section 2.1,

introducing smaller droplets to the combustion chamber can improve the spray break up, which again can reduce exhaust emissions. When the spray out of the nozzle is exposed to the chamber pressure, the bubbles can implode and contribute to a further break up of the spray, which again leads to finer droplets of fuel and faster evaporation of the fuel [30].

However, cavitation can be destructive and can damage the nozzle material by vapour bubbles collapsing under high pressure, causing a shockwave [23]. Two energy sources can cause fuel vapour formation inside the injector: kinetic energy and heating of the fuel. Studies performed on identical injectors with different fuels have shown that cavitation appears at a varying degree and is much dependent on the type of fuel utilized and its physical properties. Experiments have shown that spray formation is impacted by the in-nozzle flow cavitation for traditional fuels, while it remains unknown how ammonia behaves during the injection. Having an untypical spray characteristic, further insight into how ammonia behaves during injection is desired.

2.5 Optical diagnostic

An optical diagnostic is an important tool for additional insight into how the ammonia behaves out of the injector at different operating conditions. The density variations in a fluid can be visualized and highlight the changes in the fluid's refractive index.

For ammonia, the saturation pressure is, as mentioned in Table 1, 8.57 bar at 20°C. When injecting ammonia into a chamber with a pressure below the saturation pressure, flash boiling may occur. Flash boiling is when a subcooled liquid is rapidly depressurized to a pressure below its liquid saturation pressure [1]. This rapid reduction of the pressure will cause the superheated liquid jet to undergo a two-phase region with spontaneous bubble nucleation [31]. When the nucleated bubbles burst, smaller droplets will be ejected along with the vapour gas into the surroundings simultaneously. Compared to traditional non-flashing liquid spray, flash boiling will accelerate both the atomization and evaporation process of the spray. Accordingly, the intensity and the efficiency of the flashing process are heightened compared to simple evaporation. An illustration of flash boiling and its effect on spray behaviour is included in Figure 3.

For an injector, flash boiling can be divided into different stages based on the character-

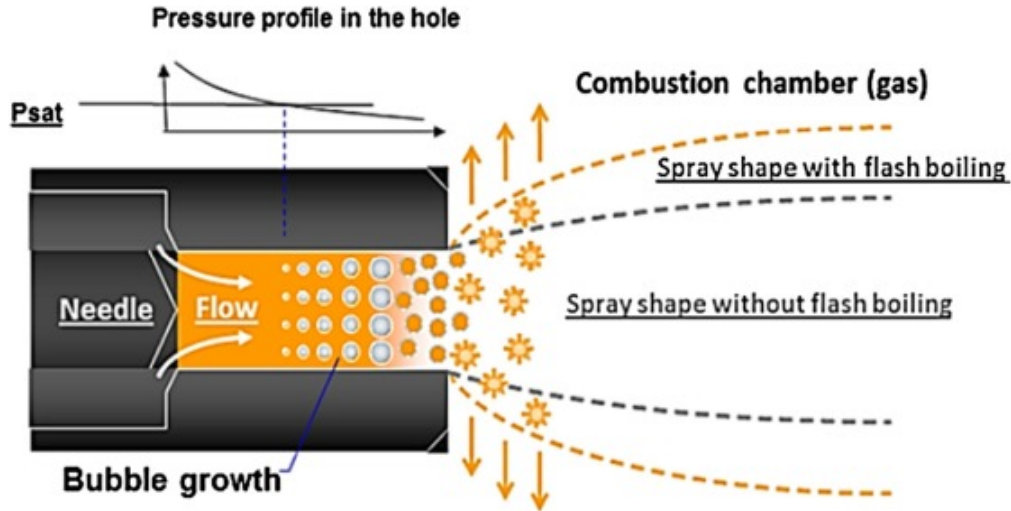


Figure 3: Illustration of flash boiling and its effect on spray behaviour, from [32].

istics of the inner flow from the injector, the spray atomization and evaporation. Critical flashing is referred to when the ambient pressure is equal to the saturation pressure[31]. The transition of flashing can be divided into three stages, first initial flashing, then transitional flashing, before fully flashing, also referred to as flare-flashing.

The spray characteristics of ammonia have been optically investigated by, e.g. [31] [1]. Li et al.[31] defined the initial-flashing region for ammonia to be $1.0 < R_p < 2.0$, transitional-flashing region for $2.0 < R_p < 5.0$ and flare-flashing region for $R_p > 5.0$, with R_p being the saturation-to-ambient pressure ratio. The evolution process of the ammonia spray penetration was found to be similar for ammonia and traditional diesel spray under critical- and initial-flashing conditions, while the bubble behaviour gradually dominated the penetration evolution under transitional- and flare-flashing conditions. Pele et al.[1] found that the geometry of ammonia spray differs from the other fuels investigated (gasoline and ethanol), being thinner under most conditions. The spray angle at half penetration length was found to be maximum at the saturation pressure of ammonia, and ammonia was found to be more sensitive to both temperature and air density than the other fuels.

The physics of flashing is still poorly understood, posing challenges for its prediction and analysis [31]. An optical investigation into the behaviour of ammonia under non-flash and flash boiling conditions is beneficial towards optimizing the design of injection systems employing ammonia and supporting numerical research.

2.6 Momentum flux

Momentum flux is important when it comes to predicting the mixing potential of the injection process. Combined with measurements for the injected mass, it is possible to determine the discharge coefficient of the injector.

Under cavitation conditions, the flow in the injector will consist of both liquid and vapour, giving a two-phase flow and two-phase dependent density. At the outlet section of the nozzle, the velocity profile will have an arbitrary flow profile, as shown in Figure 4, inspired by [2]. From Payri et al., the mass flow rate in this situation is defined as the instantaneous mass of the fuel, \dot{m} , with density ρ and velocity u passing through a nozzle hole with cross-sectional area A_0 . The mass flow rate can be written as Equation 1.

$$\dot{m} = \int_{A_0} u \rho dA \quad (1)$$

The momentum flux is defined as the mass flow rate multiplied by the velocity, as given in Equation 2.

$$\dot{M} = \int_{A_0} u^2 \rho dA \quad (2)$$

The arbitrary flow profile has complex velocity and density profiles, which can be simplified by looking at an effective, uniform velocity profile, u_{eff} , where all the fluid is flowing through an effective area, A_{eff} , in liquid phase, giving a density profile only dependent on the liquid density, ρ_l . This simplified model is shown in Figure 5, inspired by [2]. Here the effective velocity is the momentum flux divided by mass flux, as given by Equation 3.

$$u_{eff} = \frac{\dot{M}}{\dot{m}} \quad (3)$$

The effective area, A_{eff} , is the mass flow divided by the liquid density and effective velocity, resulting in a smaller area than the cross-sectional area A_0 . The effective area is given by Equation 4 [2].

$$A_{eff} = \frac{\dot{m}}{\rho_l u_{eff}} = \frac{\dot{m}^2}{\rho_l \dot{M}} \quad (4)$$

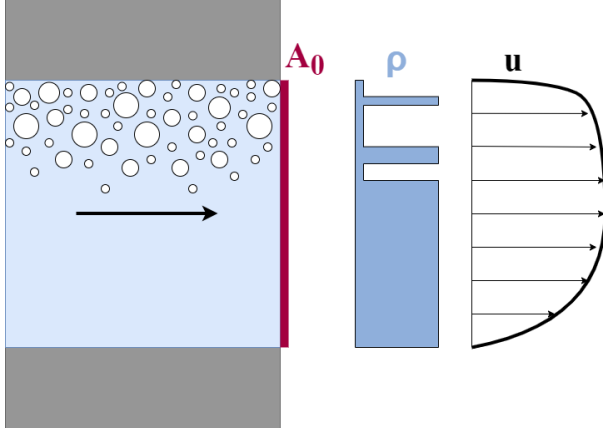


Figure 4: Arbitrary flow profile [2].

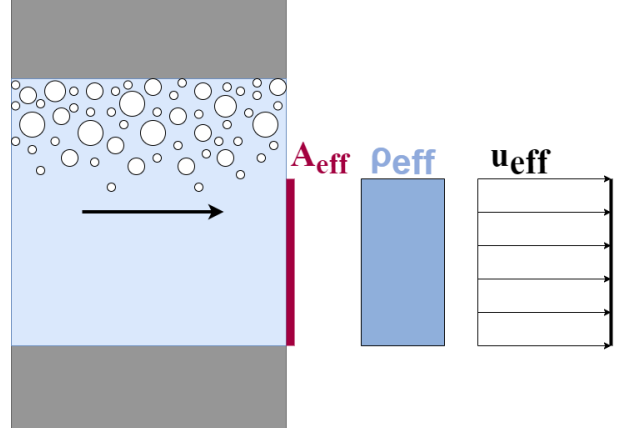


Figure 5: Simplification of flow profile [2].

Wanting to compare the effective flow characteristics to the theoretical characteristics, Bernoulli's equation can be utilized to obtain an expression with the theoretical velocity out of the nozzle:

$$P_i = P_b + \frac{1}{2}\rho_l u_{th}^2 \rightarrow u_{th} = \sqrt{\frac{2\Delta P}{\rho_l}} \quad (5)$$

In a nozzle, the discharge coefficient is a non-dimensional parameter for the ratio of the actual discharge to the ideal discharge [33]. It is defined as the ratio of the actual mass flow rate through an orifice to the theoretical mass flow rate through the orifice, for the same fluid at the same pressure drop. Now procuring expressions for both the theoretical and effective conditions, the discharge coefficient can be obtained by dividing the actual mass flow by the theoretical mass flow.

$$C_d = \frac{\dot{m}}{\dot{m}_{th}} = \frac{\dot{m}}{A_0 \rho_f u_{th}} = \frac{\dot{m}}{A_0 \sqrt{2\rho_l \Delta P}} \quad (6)$$

With A_0 being the outlet area of the nozzle. The discharge coefficient is used to understand the influence of cavitation, as cavitation leads to a reduction of the mass out of the injector, hence a reduction of the discharge coefficient. If the discharge coefficient is 1, this means that the actual mass flow is equal to the theoretical mass flow. A low discharge coefficient implies that there are more losses in the system, thus less mass is injected.

The mass flow rate out of the injector can be estimated by measuring the momentum flux of the fuel spray combined with measuring the injected mass:

$$\dot{m}(t) = \frac{\sqrt{\dot{M}}}{\int \sqrt{\dot{M}_{th}(t)}} m_{inj} \quad (7)$$

The momentum flux of a fuel spray can be found indirectly by experimentally measuring the impact force of the spray. The impact force is found by placing a piezoelectric force transducer coupled to a spray target in front of the injector nozzle. The measurement principle is shown in Figure 6. This technique has been applied in a number of other works, e.g. [34][33]. The spray target is placed close to the nozzle exit and perpendicular to the spray axis. By looking at the spray's control volume (CV), pictured as the red square in the figure, the spray momentum flux can be calculated using the momentum conservation, given by Equation 8 [33].

$$F = \frac{\partial}{\partial t} \int_{CV} \rho u dV + \int_A u^2 \rho dA \quad (8)$$

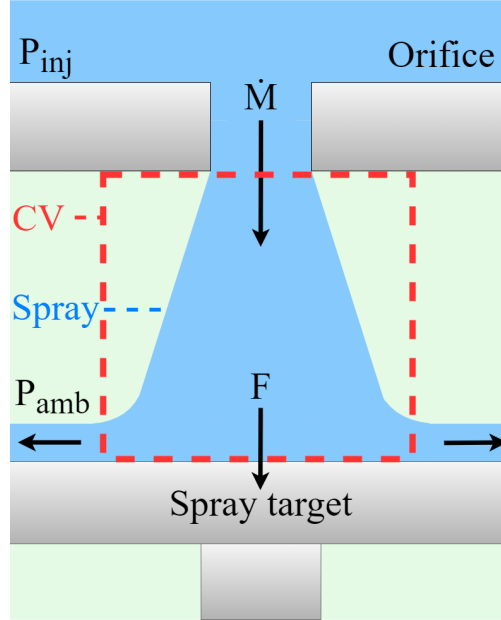


Figure 6: Illustration of the control volume for the momentum flux measurements. P_{inj} = injection pressure, P_{amb} = ambient pressure, CV = control volume, \dot{M} = the momentum flux of the spray, F = measured force.

Here, u is the velocity in the control volume, ρ is the density in the control volume, dV is the volume differential, and dA is the area differential. Simplifications were made to the momentum conservation in Equation 8 [33]. The spray was considered perpendicular to the

piezoelectric sensor. The splattered spray was considered orthogonal to the spray central axis, thus not having momentum on the same axis as the original spray. The air entrainment was considered perpendicular to the spray axis, hence not adding or subtracting momentum from the spray. There was considered a negligible mass of fluid accelerating and effects due to gravity were considered minor. The liquid jet area exiting the orifice was considered equal to the orifice area, thus assuming no cavitation, and the velocity of the jet was considered to have a uniform velocity, v_{eff} . Equation 9 displays the momentum conservation equation with these simplifications, resulting in the measured force F being equal to the momentum flux \dot{M} .

$$F = \int_{A_0} u_{eff}^2 \rho dA = \dot{M} \quad (9)$$

3 Methodology

The experiments were conducted in a high-pressure chamber built in the Motorlab at NTNU Department of Energy and Process Engineering. A description of tools and chosen approach will be made in this section.

3.1 High-pressure chamber

An illustration of the high-pressure chamber and its components are shown in Figure 7, while actual images of the experimental rig are shown in Appendix A.1.

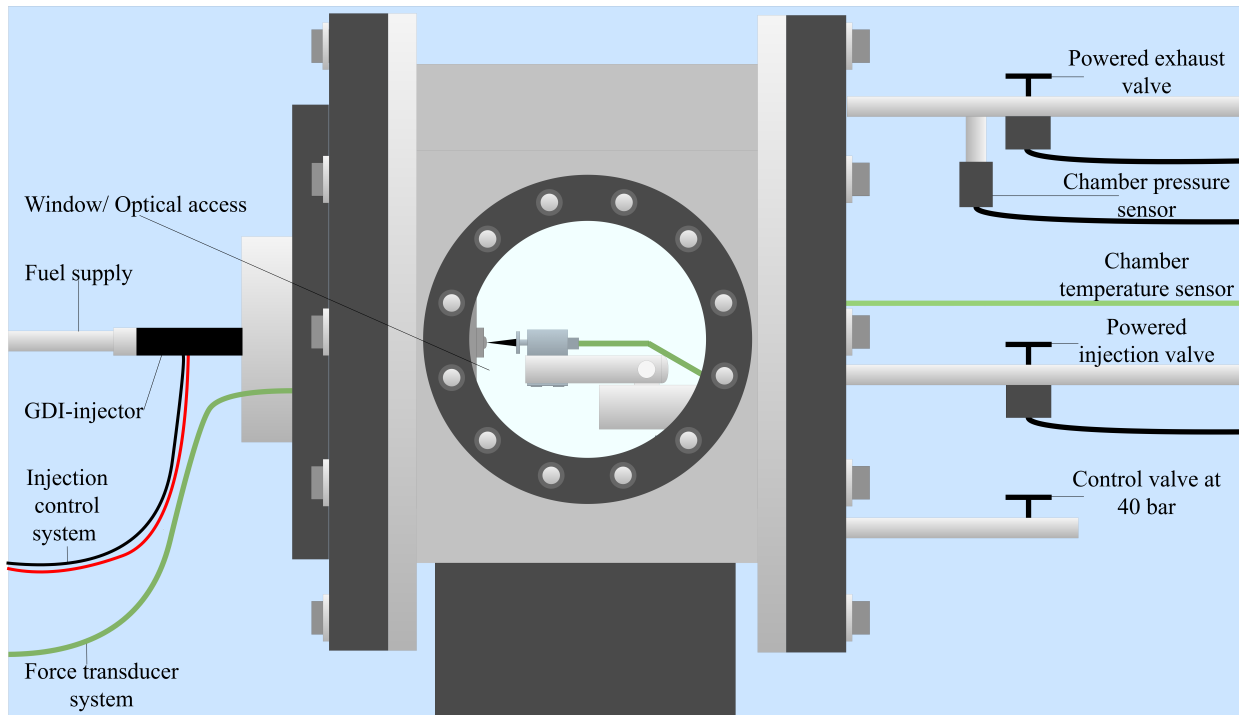


Figure 7: Illustration of the high-pressure chamber.

Throughout the experiments, the ambient pressure ranged from 1 bar up to 30 bar, hence a chamber with sufficient strength to withstand rapid pressure changes was needed. The ambient pressure in the chamber was set using a gas supply system operating on nitrogen. A pressure sensor and a temperature sensor were connected to the chamber, both monitored and logged using a Labview program. The chamber had a powered injection valve for nitrogen and a powered exhaust valve, both ports having solenoid valves controlled via Labview,

thus enabling an automated operation. In addition, a pressure release valve ensured the pressure in the chamber did not exceed 40 bar. The experiments required optical access in order to capture the spray development, hence two quartz windows with a diameter of 65 mm were used. The injector was controlled using a GDI driver from Life Racing via the Labview program. No heating or cooling elements were added to the chamber or the injector. Furthermore, for the momentum flux measurements, a force transducer was included, monitored and logged via Labview.

3.2 GDI Injector

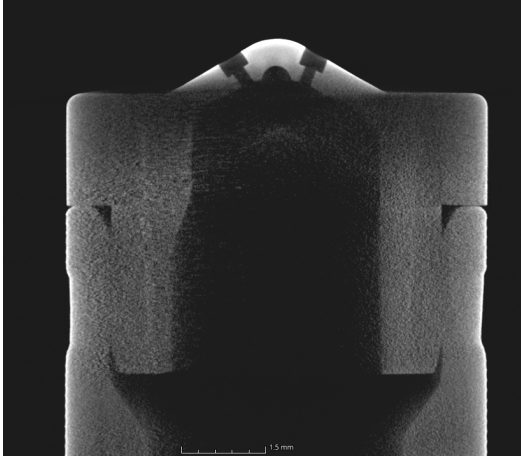
The injector investigated is a six-hole gasoline direct injection (GDI) injector (BOSCH 0 261 500 063 Injector) purposely made for passenger vehicles. As the internal flow through the injector is closely linked to its internal geometry, a deeper investigation into the internal geometry is of interest.

Previously this year, the internal geometry of this particular injector was investigated, presented in article [9]. A picture of the CT scan of the GDI injector is shown in Figure 8a, depicting the cross-section of two holes in the injector. As mentioned in the paper, the injector has a counterbore geometry, with a smaller diameter inside (d2) and a larger diameter outside (d1). Figure 8b shows the CT scan, where the green lines demonstrate the diameters. A summary of the findings obtained through the CT scanning is reproduced in Table 2.

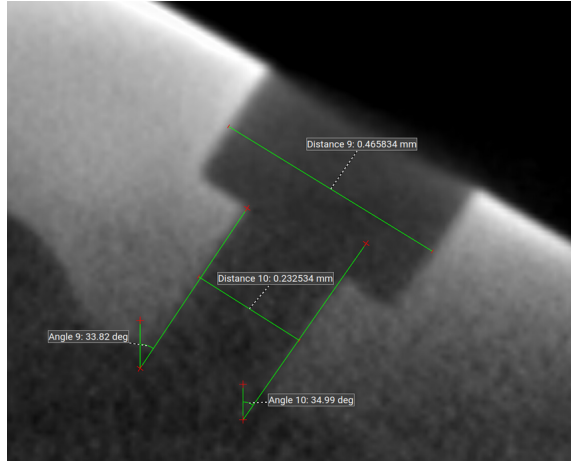
Table 2: The measured dimension of the GDI injector using CT images (reproduced from [9])

	Position [deg]	d1 [mm]	d2 [mm]	Axis angle [deg]
Hole 1	0.0	0.460491	0.23505	28.755
Hole 2	62.0	0.466225	0.22385	23.235
Hole 3	127.5	0.461275	0.22763	22.220
Hole 4	190.0	0.468065	0.21655	22.475
Hole 5	245.5	0.465834	0.23253	34.405
Hole 6	300	0.471265	0.22836	34.280
Average		0.465559	0.22733	27.562
Stdev		0.003684	0.00600	5.268

As portrayed in Table 2, there is a slight deviation in the geometry of the different holes,



(a) CT scan showing the cross-section of two of six holes.



(b) CT scan up close of one hole, with the diameters marked.

Figure 8: Pictures of the cross-section of the GDI injector obtained through CT scanning [9].

and an average is computed. Further on, the average from these findings will be used for the calculations.

3.3 Operating conditions

First, the rig was set using nitrogen. Nitrogen was employed to ensure that there were no leakages in the system, as well as to optimize the placement of the piezoelectric sensor. Thereafter, the fuel was changed to ammonia.

The conditions for the fuels are shown in Table 3. The experiments have been parted into three sub-parts, this is to clarify the slightly different operating conditions between the experiments. The same injection pressure has been employed for all experiments, 100 and 200 bar. As there were no heating or cooling elements added to the chamber or the injector, the temperatures were kept close to constant. The fuel for the experiments has been ammonia, with the exception of the momentum flux initially employing nitrogen to optimize the spray target position. The same ambient pressures have been used for each subpart, testing at 2, 10 and 20 bar. The reason for choosing the given pressures was to investigate the ammonia characteristics under three different conditions, at a pressure far above (20 bar), close to (10 bar) and far below (2 bar) its saturation pressure. 2 bar was chosen instead of 1 bar to be

able to have continuous flushing of the system during the experiments while remaining at a constant pressure. In addition to these pressures, 1, 4, 8 and 30 bar were investigated for the shadowgraph imaging experiment. The injection duration has been 1 millisecond (ms), but additionally, the effect and behaviour of a longer injection duration have been examined for the momentum flux and shadowgraph imaging experiments.

Table 3: Key parameters of the experimental conditions.

Parameter	Momentum flux	Mass flux	Shadowgraph
Injection pressure (P_{inj} , bar)	100, 200		
Ambient temperature (T_{amb} , °C)	18		
Fuel temperature (T_f , °C)	18		
Ambient gas	Nitrogen gas, N ₂		
Injection fuel	Liquid ammonia, NH ₃ , Nitrogen gas, N ₂	Liquid ammonia, NH ₃	
Ambient pressure (P_{amb} , bar)	2, 10, 20	2, 10, 20	1, 2, 4, 8, 10, 20, 30
Injection energizing time (ms)	1, 2, 3	1	1, 5

3.4 Ammonia fuel system

An in-house developed nitrogen-pressurized system has been used to feed the liquid ammonia to the GDI injector. A piping and instrumentation (P&ID) diagram for the ammonia fuel system is shown in Figure 9. The system consists of 6 mm Swagelok connections and ball valves. The ammonia is supplied from a bottle holding 13.8 kg of ammonia into a 0.5 L fuel tank, before being pressurized to the desired pressure using nitrogen up to 200 bar.

Considering the hazardous nature of ammonia [35], having appropriate safety measures is important. Accordingly, having powerful room ventilation is needed. The room where the experiments have taken place has ventilation made to continually move air out of the room, thus depressurizing and creating negative room pressure. In this manner, the risk of contamination to neighbouring rooms is minimized and any potential leakage of ammonia is quickly removed from the room [36]. In preparation for filling the system with ammonia, a leakage test is executed using nitrogen. This is to find and fix any occurring leakages, thus minimising the possibility of ammonia leakage into the room. During the experiment, the executor stays in the neighbouring room, monitoring and controlling the experiment

through a Labview program, thereby minimising the risk of exposure. However, during the charging and discharging of the system, physical accessibility to the system is needed, and safety precautions such as a protective mask and portable gas detector have been utilised. Its toxicity also makes the pressurising process more complex for ammonia. The methods used for charging and discharging the system will be explained in the following sections.

3.4.1 Charging the system

The first step when charging the system is to purge the system using nitrogen. In this manner, any residues from the system are taken into the floor water tank, thus avoiding contamination. The procedure begins by first confirming that all valves are in the correct position: looking at Figure 9 this means that all valves are closed (called V-valves in the diagram) while all safety-valves are in an open position (named S-valves in the chart). The nitrogen regulator is opened and set to a pressure below 50 bar. Then the valves are opened to enable purging: first opening the valve for the nitrogen bottle, V5, then opening the line into the pressure cylinder, V2, followed by opening the line from the cylinder to the injector, V3, before slowly opening the injection valve, V8. This will clear out residues from the system into the tank, and bubbles will appear in the water. Then, the system is cleansed for approximately one minute before closing all the valves in the same order: V5, V2, V3 and V8. After the purging, the cylinder contains nitrogen at atmospheric pressure.

Now the system is ready to be filled with ammonia. Referring to Figure 9, filling the system is achieved by first opening the ammonia bottle and its valve, V7. Following, V1 is opened. As the cylinder was at atmospheric pressure, the pressure difference between the cylinder and the ammonia causes some ammonia to flow into the cylinder and slightly increase its pressure. Now having compressed nitrogen gas in the cylinder, the next part is to vent out nitrogen into the water tank, hence opening the valves from the nitrogen line to the water tank: opening V2 and V6 before slightly opening NV1. Using the ammonia vapour pressure at room temperature, nitrogen flows out of the cylinder and the cylinder starts filling up with ammonia. When approaching the desired amount of ammonia, closing NV1 will stop the flow of nitrogen out of the system. After approximately a minute, the pressure in the cylinder stabilizes and the ammonia inflow stops. Following, the other valves

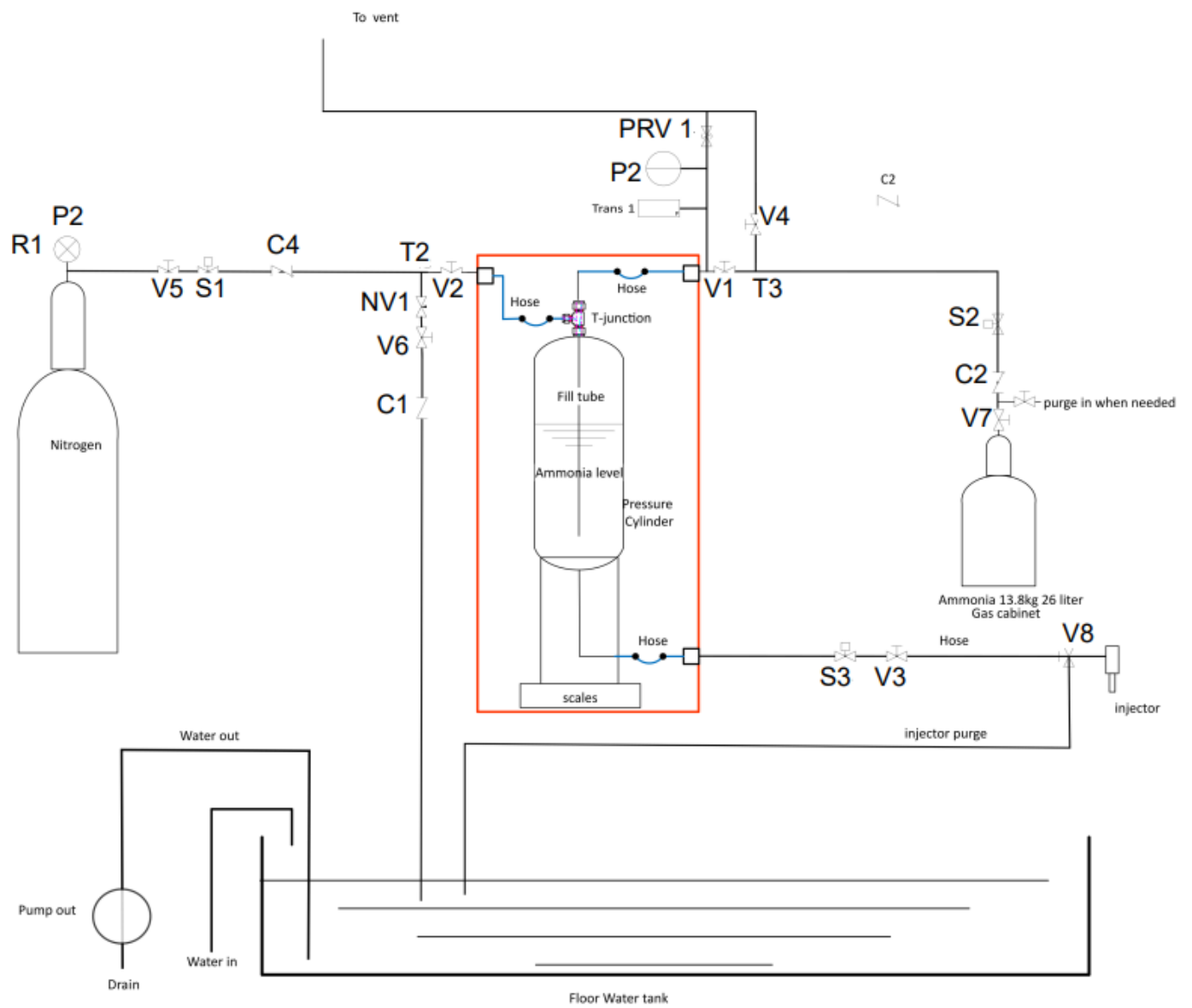


Figure 9: P&ID diagram of the ammonia fuel system.

get closed, V6, V2, V1 and V7, before closing the ammonia bottle. Now the cylinder is filled with ammonia.

The next part is to fill the injection line with ammonia and pressurize. This is done by first opening the valve for ammonia out of cylinder, V3, referring to Figure 9. Thereafter, V8 is slowly opened to discharge the gas from the line into the water tank. Now, the injection line is primed with ammonia. The following step is to pressurize the system using nitrogen, but as opening V8 has a cooling effect on the valve (V8), to avoid any leakages, waiting five minutes for the valve to again reach room temperature has been conducted. Subsequently, pressurizing the ammonia has been achieved by opening the nitrogen bottle, regulating it to 20 bar, then opening the valve for the nitrogen bottle, V5, and opening the line into the cylinder, V2. Thereafter, gradually regulating to the desired pressure.

Now the system is filled with ammonia, pressurized and ready for experiments. From Figure 9, the open valves are V2, V3 and V5, this is to keep the system pressurized throughout the testing.

3.4.2 Discharging the system

After conducting the experiments, correct discharging of the system is important. The first step is releasing the system's pressure to around 8 bar. Beginning by closing V5, referring to Figure 9, hence closing the nitrogen supply. Then the line for nitrogen to the water tank is opened by opening V6, before slowly opening NV1 to depressurize.

The next step is to clean out the ammonia from the system. Beginning with slowly opening V8, thus making the ammonia flow through the injector purge line to the water tank, leaving the cylinder at atmospheric pressure. Afterwards, it is desired to clean out any residues of ammonia by purging the system with nitrogen. This is achieved by first regulating the pressure of nitrogen to be below 50 bar. Then slowly opening V5, making nitrogen flow through the system. Continuing, V1 is opened. The system is now purging. To clean out the residues, the system is purged for five minutes before closing all valves.

The final step is to change the water in the floor tank by running the pump and filling it with fresh water.

3.5 Momentum Test Rig

Based on the rig setup made by Payri et al. in [29], a momentum flux measurement rig was assembled. A piping and instrumentation (P&ID) diagram of the experimental setup is shown in Figure 10.

During the experiments, the data acquisition and injection control system set up in Lab-View was used to monitor the chamber temperature, chamber pressure, fuel injection pressure and force measurements. From this program, the injection duration and chamber pressure were set while enabling the logging of measurements, flushing of the system and camera activation. After each injection, the chamber was flushed with nitrogen to remove any ammonia residues. The fuel was injected into the chamber using the ammonia fuel system. The injections were captured using a high-speed camera with a LED light source placed on the opposite side of the chamber. The injection duration varied from 1 ms to 3 ms, the chamber pressure varied from 2 bar to 20 bar, and the pressure of the fuel injected varied from 100 bar to 200 bar. For each tested condition, a minimum of 15 injections were executed.

From this experimental equipment, it was possible to establish the impact force of the spray, which is equal to the momentum flux of the spray in the axial direction (from $F = \dot{M}_{axial}$). As mentioned in section 3.2, due to the hole geometry of the injector, the liquid jets of the spray interacts with the target at an angle. To obtain the actual momentum flux of the spray, a correction for the angle is required.

$$\dot{M} = \frac{F}{6\cos(\theta)} \quad (10)$$

By employing Equation 10, the actual momentum flux of a single hole is provided; \dot{M} . F is the measured force acquired from the force transducer. The measured force is divided by 6 to obtain the momentum flux of a single hole, and the angle θ is the correction factor from the measured hole geometry, from Table 2.

3.5.1 Piezoelectric force transducer

To measure the impact force of the spray, a piezoelectric force transducer with a range of at least 0-10 newton was required [33]. Considering the short duration of the injection, the

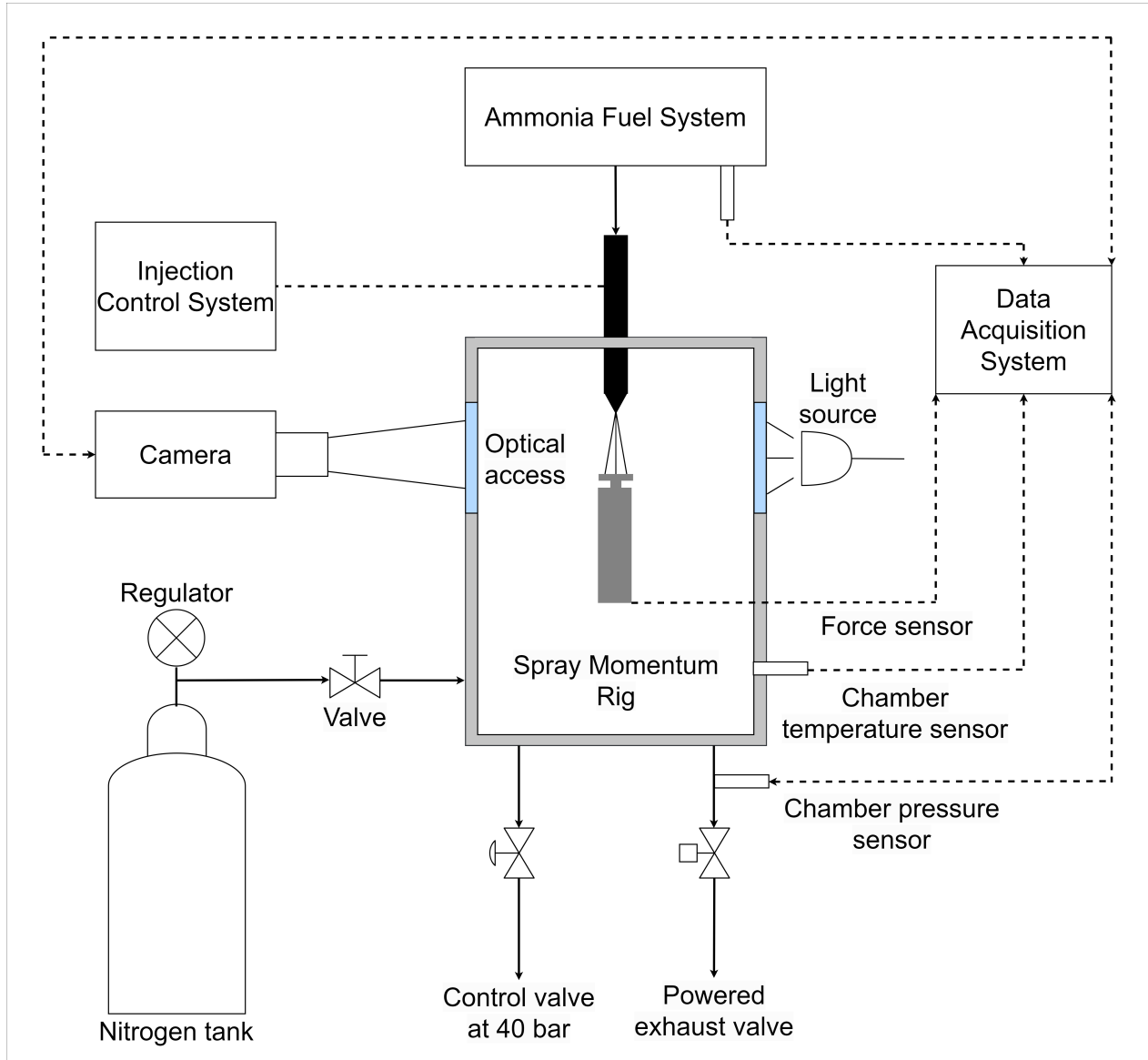


Figure 10: Illustration of the spray momentum rig.

force transducer needed to have a rise time of a few microseconds. Having a short time scale combined with the oscillatory nature of the measurements, a device with a high natural frequency of at least 50 kHz was required. As the experiments were with high-pressure ammonia, the material of the device had to be resistant to physical and chemical erosion. Consequently, the Kistler model 9215 force transducer was chosen for this study, being able to measure dynamic forces from -20 to 200 newton, capable of measuring loads down to 1 millinewton, a natural frequency in excess of 50 kHz and made in stainless steel.

The face of the force transducer consists of a 2 mm threaded bore to accept a screw. This screw is what is referred to as the spray target, and is the component introducing the impact force into the transducer's sensing component.

The piezoelectric sensor was connected to pillar posts with angle post clamps, thus giving high mobility to the placement of the spray target. This bracket design allowed for an adjustment in distance from the target to the nozzle and an adjustment in the angle of the target. An illustration of this setup is shown in Figure 11.

3.5.2 Testing different spray target sizes

Originally, the piezoelectric sensor had a spray target with a diameter of 4 mm. As the injector investigated contains six holes, the spray diameter was observed to be wider than the original spray target. Wanting to capture the entire spray, new targets were customarily made by the mechanical engineering workshop at the NV faculty at NTNU, with diameters of 6, 7, 8 and 9 mm. These targets were tested under the same conditions, with nitrogen injections at 100 bar and ambient pressure of 1 bar.

In order to access the spray targets when changing between the different sizes, the piezoelectric sensor had to be moved. To achieve the most precise comparison between the target sizes, having them located in the same position was necessary. Therefore, it was desired to minimize the number of variables between each change, meaning minimize the number of adjustments made between each change. Thus, the only part adjusted when changing the spray targets was the lower angle post clamp, referring to Figure 11, which was used to rotate the bracket.

As support when aligning the bracket, the camera was used to ensure the piezoelectric

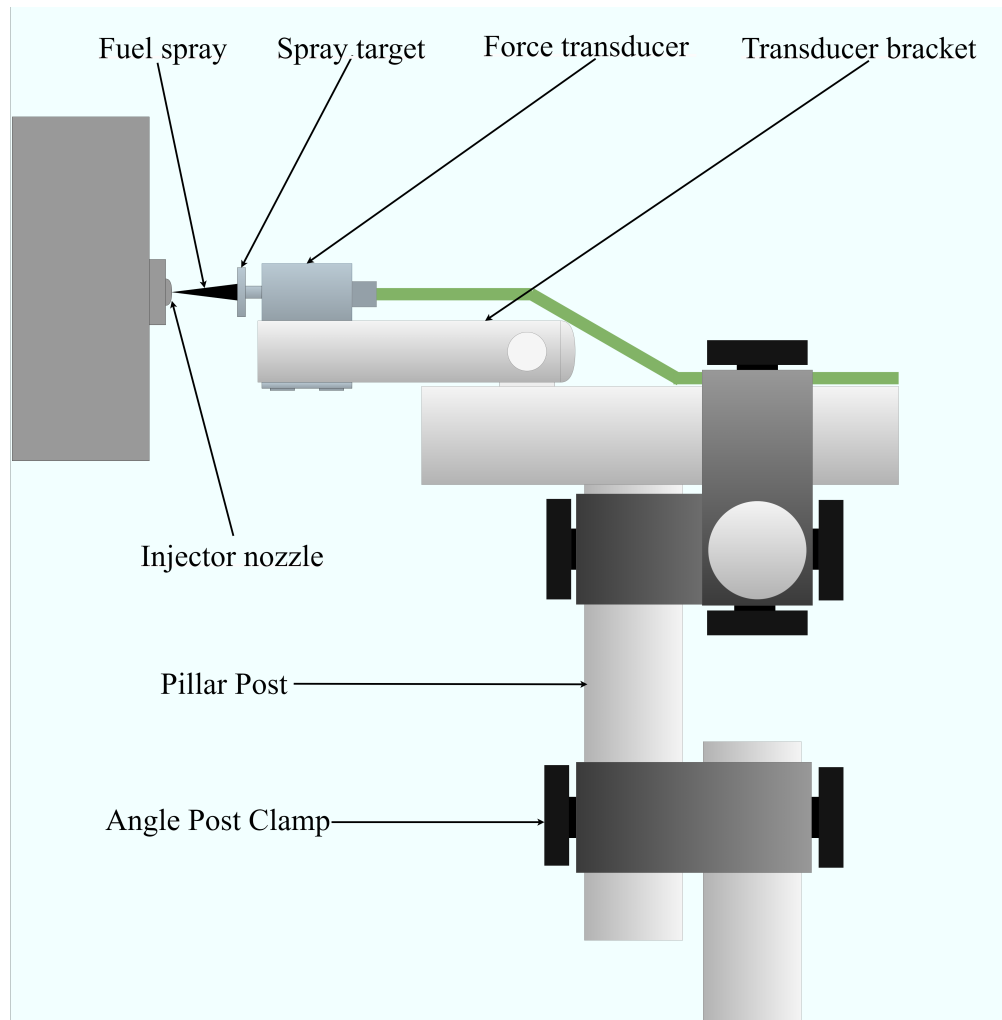


Figure 11: Illustration of the force transducer set-up with the spray target presented to the emerging fuel spray.

sensor remained in the same position for each target, pictured in Figure 12. Figure 13 displays an illustration of Figure 12, to clarify and label the different components pictured. In the figures, the injector is located to the left, the piezoelectric sensor to the right and its target is located in the centre. As shown in Figure 12, the drawing tool in the Photron Fastcam Viewer software was used to make a red line where the face of the target should be and a red box to ensure the same alignment of the piezoelectric sensor for each condition.

3.5.3 Testing spray target at different positions

Correct placement of the force transducer target is important to obtain reliable results from the momentum flux experiments. Thus, different angles and distances between the injector

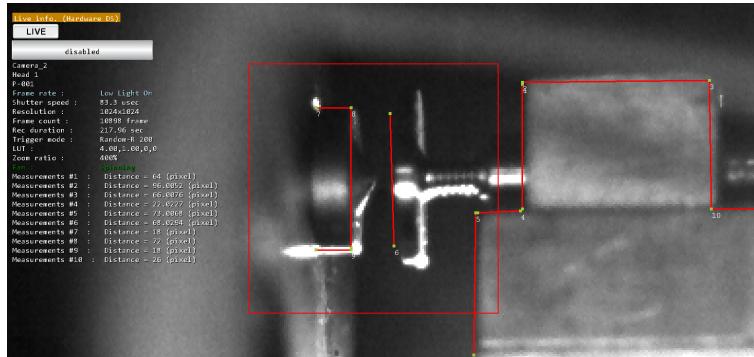


Figure 12: Picture of the camera settings used to ensure that the piezoelectric sensor remained in the same position when changing spray targets.

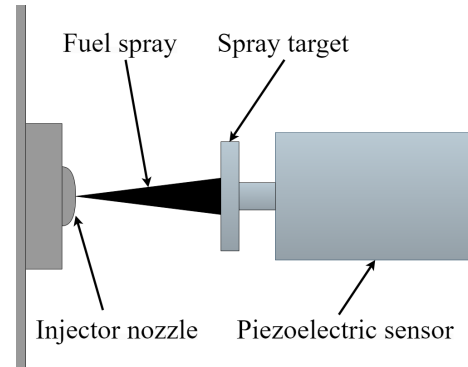


Figure 13: Illustration of the components shown in Figure 12, with labels

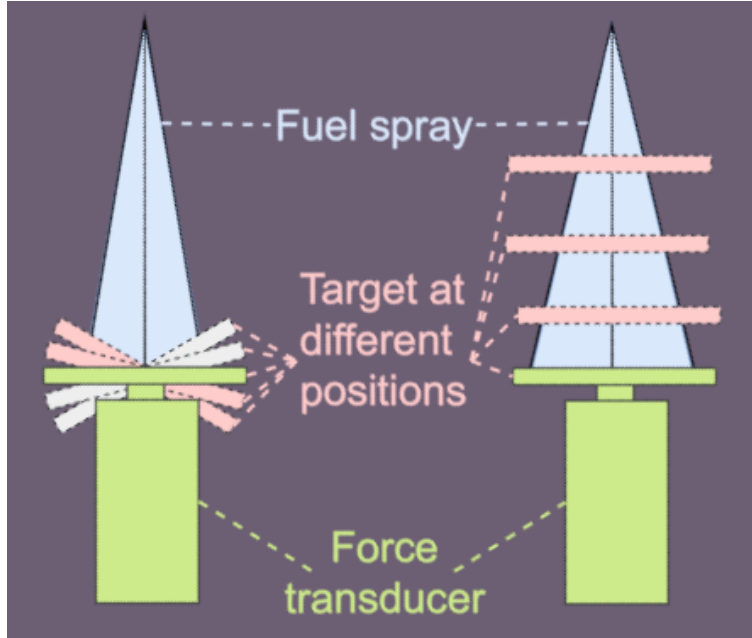
and spray target were experimentally tested, assuming the position giving the highest force measurement to be the optimum position. In addition, measuring for different positions would give an estimate of how the placement of the target affects the given results.

First, the optimum angle was found. The sensor was set at a given distance from the injector while only varying its angle. This is illustrated to the left in Figure 14a, where each of the squares illustrates a placement of the sensor target. To ensure that the distance between the injector and sensor remained constant, a circle was drawn in the Photron Fastcam Viewer software and was utilised as a reference when aligning the target, shown at the top in Figure 14b. Following, the measurement tool in the camera software was used to review the footage capturing the injection to verify that the correct distance had been used for the given position.

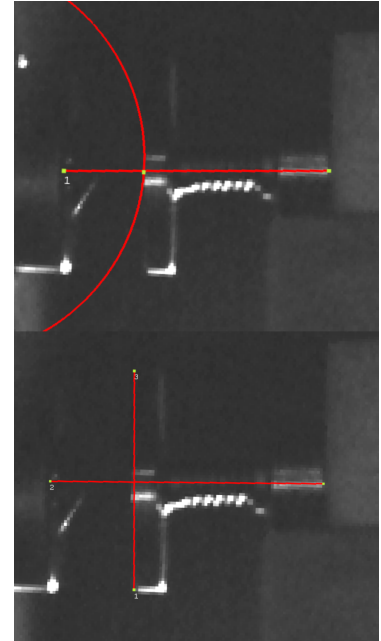
Thereafter, the optimum angle obtained from the previous testing was employed, and varying the distance was examined. An illustration of the method for varying the distance is shown to the right in Figure 14a. The camera software was used to draw a line corresponding to the optimum angle, shown at the bottom of Figure 14b. During testing at various distances, the target was placed parallel to this vertical line.

3.6 Mass flux

To enable calculations for the discharge coefficient, from equation 6, a measurement of the injected mass is required. In this work, the injected mass was acquired by adding a scale to the ammonia fuel system, enabling continuous monitoring of the weight of the fuel. An



(a) Illustration of varying the angle and distance of the spray target, with each square representing a position for the spray target.



(b) Setup for varying position, for angle above, distance below.

Figure 14: Illustration and pictures of varying position of spray target.

illustration of the injected mass measurement principle is shown in Figure 15. As shown in the figure, the tank contains both nitrogen and ammonia and when increasing the pressure, the density of both ammonia and nitrogen increases. When calculating the ammonia mass in the pressurized tank, the nitrogen content was also considered.

The injection duration was 1 ms, the chamber pressure varied from 2 to 20 bar, and the pressure of the fuel injected varied from 100 to 200 bar. Throughout the experiments, the chamber was continually flushed with nitrogen while holding a set chamber pressure. As the injected mass per injection is low, 3,500 injections were executed for each condition. As there is no combustion, frequent injections have a cooling effect on both the injector tip and the chamber. Consequently, an injection frequency of 0.33 Hz was chosen to avoid significant cooling, meaning an injection every third second. In this manner, the temperature was kept near room temperature at 16°. To support these measurements, a lower frequency was also examined, with an injection frequency of 0.11 Hz.

The mass flux was obtained by employing Equation 7, utilising the measurements for the momentum flux and injected mass.

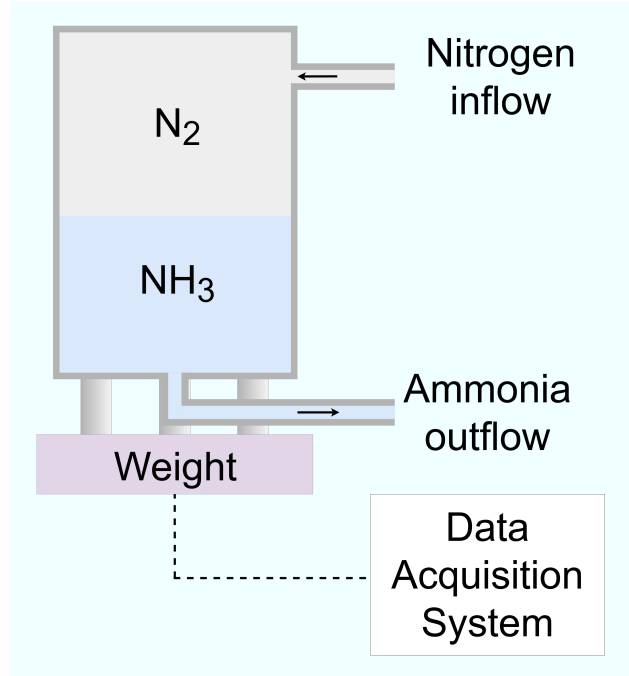


Figure 15: Illustration of injected mass measurements.

3.7 Shadowgraph

Figure 16 depicts the schematic of the experimental equipment utilised during the shadowgraph imaging, including the constant volume chamber, the ammonia fuel system, the high-speed camera and the data acquisition system. As illustrated in Figure 16, the LED light is contracted through a pin-hole, before reaching the beamsplitter, where half of the light is reflected toward the chamber. The light is sent through the chamber and then reflected by the spherical mirror before returning back through the chamber. Consequently, the light proceeds through the chamber and the ammonia spray twice, resulting in a density influence in both directions, providing a double sensitivity to the measurements. After the light is through the chamber, half of the light passes through the beamsplitter and is then contracted through the pin-hole before reaching the camera lens.

The pin-hole in front of the camera was utilised for the alignment of the equipment. During the experiments, it was wide open, hence not cutting off any significant light. Accordingly, the imaging technique is referred to as shadowgraph imaging instead of schlieren.

The chamber was equipped with two optical accessible windows and was operated at a

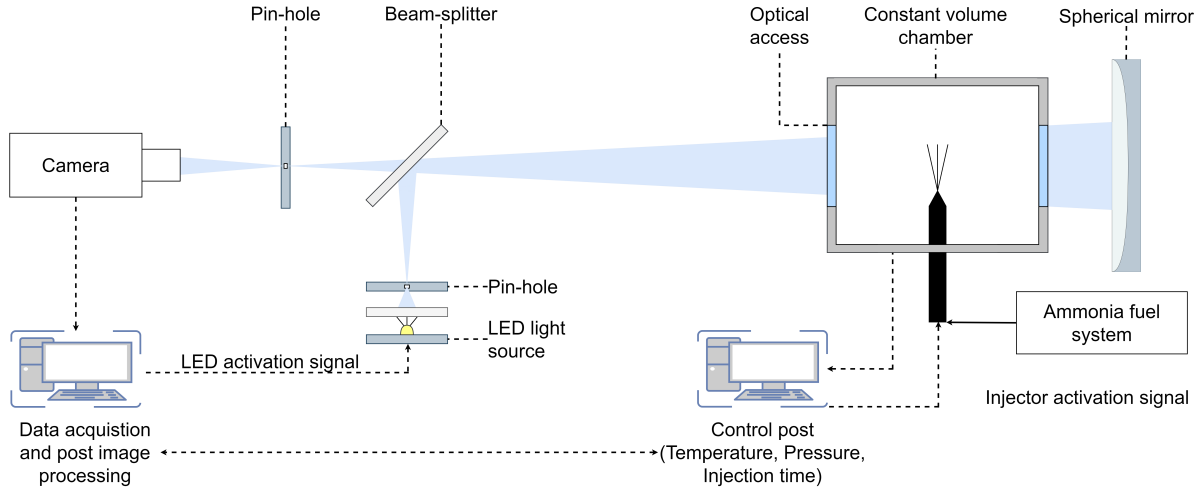


Figure 16: Illustration of the optical setup.

chamber pressure varying from 1 bar to 30 bar. An energizing time of the injector of 1 ms and 5 ms was utilised, with an injection pressure of 100 and 200 bar. For each condition tested, 5 recordings were taken, from the injection start to 1 ms after the end of injection. After each injection, the chamber was flushed using nitrogen. The period was set at 1 ms with no pulse delay. The LED pulse width was 16 μ s, the amplitude was 5, and the voltage was set at 6.5V. The equipment employed during the experiment is summarized in Table 4

Table 4: Equipment employed in shadowgraph imaging.

Equipment	Model
High-speed camera	Photron FAST-CAM Nova S16
Pulse generator	TGP110 10MHz Pulse generator
Digital storage oscilloscope	Iso-Tech IDS-2104E
Switching mode power supply	BK Precision 16
LED light	Luminus SST-90
Beamsplitter	Knight Optical BAE14507 VIS, R=50%/T=50%
Spherical mirror	D=150 f8, F=1200

To achieve clear and satisfactory imaging, the alignment of the equipment is important. As a result of the equipment being misaligned, a double image tendency, also called diplopia, was detected: meaning two equivalent images were observed as slightly displaced from one another. Due to the optical accessible windows not being cleaned prior to alignment, there were dust particles on the glass. These dust particles were used to document the double

image tendency and aid with the alignment of the equipment. An object was also placed in the position of the injector to depict where the spray would be injected.

The consequence of misalignment is depicted in Figure 17, where pink and blue shapes are included to enhance the corresponding shapes in the different images. The object is enhanced with squares in the picture. If the equipment were aligned, the locations of the pink and blue shapes would be identical.

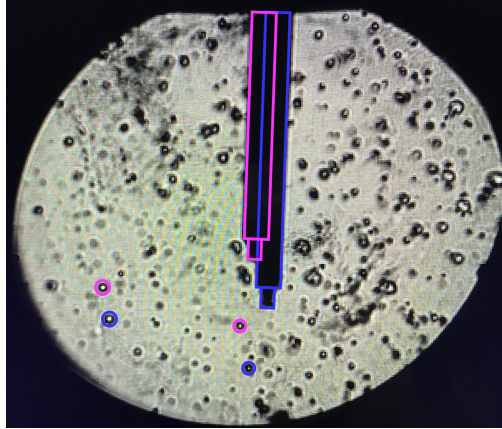
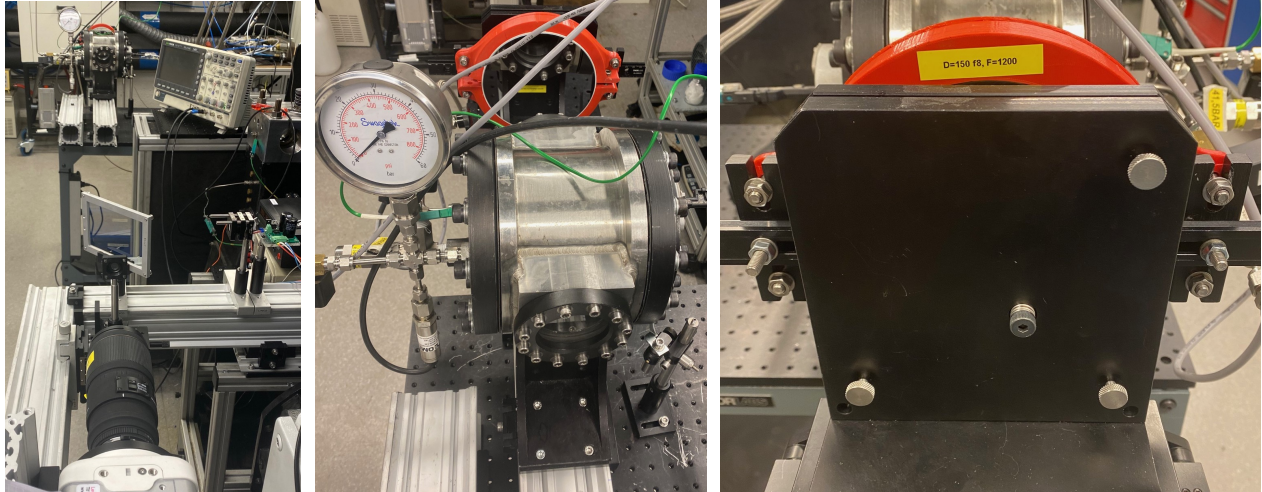


Figure 17: Picture demonstrating the double image effect during misalignment.

To obtain a precise alignment, the first step was to do a rough arrangement, meaning aligning the chamber, camera, beamsplitter and mirror. In this project, a thread was employed as assistance to lining up the chamber with the camera. The next step was measuring the pin-holes to be at corresponding heights. Thereafter, the LED light source was utilised as a support for the rest of the alignment. First, the light was used to adjust the beamsplitter, ensuring reflection through the chamber windows. Thereupon, the LED was utilised to adjust the mirror to the correct orientation, ensuring the light was reflected to the centre of the pin-hole in front of the camera. Finally, the pin-hole was moved to the point with the highest light intensity.

Figure 18 depicts pictures of the shadowgraph setup. In picture 18a, the layout is displayed from the camera point-of-view. Figure 18b shows the constant volume chamber with the spherical mirror in the background, both installed on the same rail. In Figure 18c, how to adjust the mirror is displayed. The three visible pins were used to orientate the plate attached to the mirror, giving high mobility for the mirror orientation.



(a) Layout from camera point-of-view. (b) The constant volume chamber with spherical mirror. (c) Spherical mirror with a 3-axial adjustment possibility.

Figure 18: Pictures from the shadowgraph setup.

3.8 Camera

Throughout the experiments, images of the spray have been captured using a high-speed camera, Photron FAST-CAM Nova S16. The camera has been utilised to optically inspect the spray behaviour out of the injector, by shadowgraph, in addition to achieving more precise placement of the spray target for the momentum flux experiments.

To obtain detailed pictures, the correct settings for the camera are important. For this project, frame rate and shutter speed have been tested and optimised. Frame rate is defined as the frequency at which consecutive images are displayed [37]. Increasing frame rate means the camera will capture more frames per second (fps), but will also result in a reduction of image resolution [38]. Shutter speed is the speed at which the shutter of the camera closes. A high shutter speed implies a short exposure time, resulting in a sharper image [39]. For slower shutter speeds, more light is transmitted through the lens. For a too-low shutter speed, the picture becomes over-exposed, and information in the picture may get lost. Different shutter speeds were tested to find an appropriate duration.

The settings for the two different setups are summarized in Table 5.

Table 5: Summary of the camera settings.

	Momentum flux	Shadowgraph imaging
Frame rate [fps]	160,000	40,000
Temporal resolution [data points per ms]	160	40
Resolution	128 x 128	384 x 336
Exposure time [μ s]	4.3	10.0
Zoom ratio [%]	599.2	228.0

3.8.1 Momentum flux

For the momentum flux measurements, a LED light source has been used to increase brightness. Hence, by a further increase of the light source, brighter images can be obtained with a shorter exposure time. For these images, a frame rate of 160,000 fps and an exposure time of 4.3 μ s were employed, giving a temporal resolution of 160 data points per ms.

3.8.2 Shadowgraph

The aim of the shadowgraph experiments was to capture the spray development throughout the chamber, thus wanting the camera to capture the entire optical accessible window. Consequently, as the camera was set to capture a wider area than in the momentum flux imaging, the frame rate was reduced to 40,000 fps, resulting in a temporal resolution of 40 data points per ms. The exposure time was set at 10.0 μ s.

3.9 Post-processing

3.9.1 Momentum flux

During the experiments, each injection was logged in Labview, to a TDMS file. A minimum of 15 injections were performed in each position, giving a minimum of 15 files per condition. Executing over 750 injections, resulting in more than 750 files, it was required to create a sound system for the stored data. The measurements acquired were organized and post-processed using Python.

The data obtained were separated into two parts: one for the low-speed measurements;

chamber temperature, chamber pressure and fuel pressure with low-speed time, and one for the high-speed measurements; force and injector signal with high-speed time.

The high-speed measurements had a frequency of 100,000 Hz, hence a high number of points were logged. For instance, the first injection gave 212 992 measured points for the force. For all the injections, this provides a considerable amount of data. The injections lasted between 1 ms and 3 ms, hence the injection time was a fraction of all the recorded data. As the injection occurred, a signal was registered and logged in the stored data file. Continuously, Python was employed to find this precise moment and the corresponding measurements to this point.

Python was applied to iterate through every file for a given condition/position, taking the average of all the injections and providing the trend of said condition. To take the average, the following equation was used:

$$\bar{F}(x) = \frac{1}{N} \sum_{i=1}^N F_i(x) \quad (11)$$

The mean is taken at every measured point x of the spray, \bar{F} refers to the averaged force, $i = 1, 2, \dots, N$, and N is a number of sample files.

To achieve the momentum, the integral of the momentum flux has been calculated using the built-in trapezoidal integral function in Python. The trapezoidal integral is given by the following equation:

$$M = \frac{\Delta t}{2} \sum_{i=1}^N (F(x_{i-1}) + F(x_i)) \quad (12)$$

With M being the momentum and Δt being the time-step. Further on, the Matplotlib library was used to visualise the results.

After the results had been analyzed, an infinite impulse response (IIR) filter was added from the built-in Python library SciPy, giving measurements without short-term fluctuations. The filter was added post-testing not to lose any tendencies or data during the experiments, but rather have fine-tuning afterwards. The filter utilised was Savitzky-Golay, which is a filter used to eliminate noise and improve the smoothness of a signal trend [40]. The parameters employed were a window size of 7 points and polynomial order of 3.

3.9.2 Mass flux

The Python environment was utilised for the calculations of the injected mass. The pressurized ammonia tank contained both nitrogen and ammonia, thus to obtain the weight of ammonia, both substances needed to be taken into consideration. The pressure in the tank was dependent on the injection pressure, hence varying at the different conditions. To find the densities of ammonia and nitrogen, the CoolProp library in Python was employed. For each condition, 3,500 injections were conducted. Each measured point was calculated by taking the average of the injected mass from 500 injections. Thereafter, Python was employed for calculating the mass flux, using Equation 7, and the Matplotlib library was used to visualise the results.

3.9.3 Shadowgraph imaging

For shadowgraph imaging, the raw images were processed using several steps in the Python environment. In Python, the intensity of a pixel was set between 0 and 4096, where 0 represented black and 4096 was white. The raw image files had a resolution of 384 x 336. The number of frames per image was 150 for an injection duration of 1 ms, and 350 frames for 5 ms.

Figure 19a displays the raw image of the spray, meaning the non-processed image. First, the images were zoomed in, only portraying the optical accessible window. As the injector is not perpendicular, to simplify the calculations and better visualize the angles and spray penetration, the image was slightly rotated to a vertical position. This is portrayed in Figure 19b. As the exposure of the LED can slightly vary throughout the injection, images of the background were taken before injecting ammonia. Thereafter, the background was subtracted from the raw image frame by frame, as depicted in Figure 19c.

The definition of the spray characteristics for the ammonia spray is illustrated in Figure 20. The spray penetration length (SP) is defined as the location of the spray furthest away from the injector tip, meaning the most extended distance the spray has proceeded at a given time. This is illustrated in Figure 20a by the pink line. SP was found by using a while-loop in Python, searching through the rows in the image for a pixel intensity above 1,500, calculating

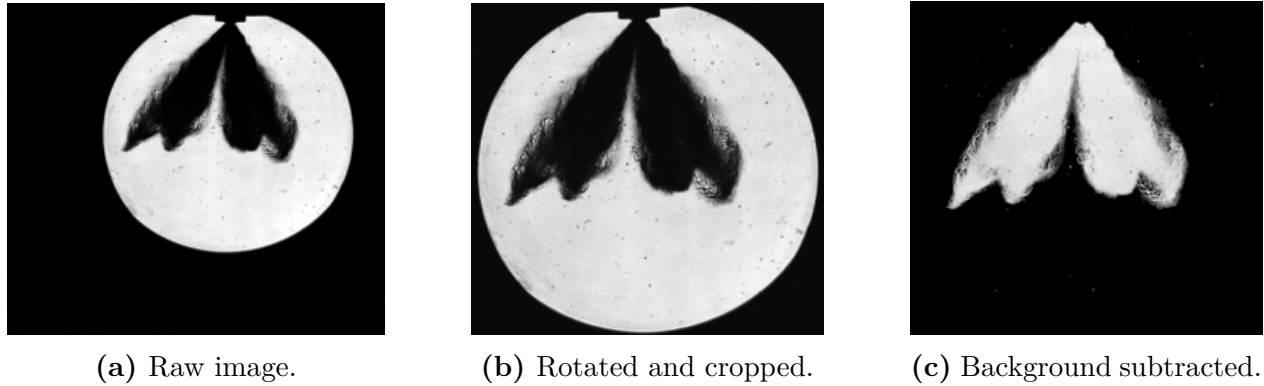
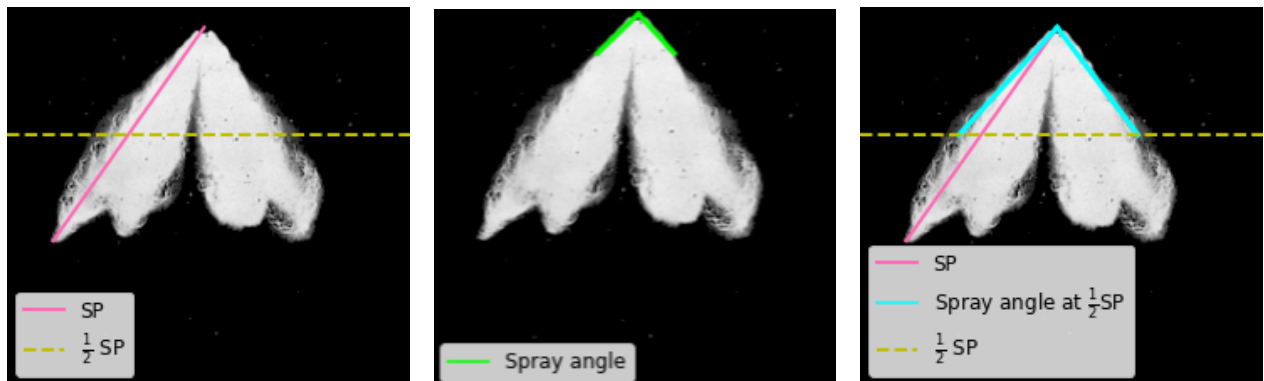


Figure 19: Post-processing of shadowgraph with liquid ammonia spray at an injection pressure of 100 bar and ambient pressure of 10 bar as an example.

the vector length to the nozzle and returning the position with the highest distance. In the same Figure, the half penetration length ($\frac{1}{2}SP$) is defined as being half the distance of the penetration length and is depicted as the yellow line.

Two spray angles have been examined in this project. The first angle is described as the spray angle. This is the angle of the spray out of the injector and is defined as the angle 6 mm from the nozzle. An illustration is shown in Figure 20b. The second angle is described as the spray angle at half penetration length and is portrayed in Figure 20c. The angles were obtained using a while-loop in the Python environment, searching at the given distance for pixels with a higher intensity than 1,500. Afterwards, the Matplotlib library was used to visualise the results, and for the spray angle at half penetration length, the IIR filter was used with a window size of 16 points and polynomial order of 3.



(a) Penetration length and half penetration length. **(b)** The spray angle out of the injector. **(c)** Spray angle at half penetration length.

Figure 20: Definition of spray characteristic for the ammonia spray.

3.10 Single-hole GDI

In this thesis, the injector investigated has six nozzle holes, as shown in Figure 21a. This is an injector where the adjacent plumes interact. As mentioned in Section 3.2, the measurements performed in this report are based on the injector geometry. Accordingly, verifying the results obtained with the six-hole GDI with results from a single-hole GDI injector is of interest.

Two approaches can be taken to obtain measurements of a single hole out of the injector. The first approach is using a lateral configuration singling out one plume. This is described by Payri et. al. in [2]. Considering the plumes being close together, it was reported uncertainties in the results due to interaction between adjacent sprays. To avoid the interactions as much as possible, the spray target had to be placed far away from the injector tip, which could cause the spray plume not to be entirely collected. This was particularly difficult when raising the ambient pressure.

Due to the uncertainties reported in the first approach, a second approach was investigated: creating a single-hole GDI injector. The idea was to weld five of the six holes, thus having an isolated spray giving more precise measurements. Consequently, the injector was delivered to Gullsméd Karlgård, where they used laser welding, which is a micro-welding technology. Laser welding is a welding process that uses a laser beam to form a weld. The laser beam is a highly concentrated heat source and concentrates the power to a very small diameter [41]. This enables a high depth-to-width ratio to the welds: the welds can have a small width: diameter, while maintaining a deep penetration: depth. Thus, making it possible to join together thin layers of metal with high precision. In Figure 21b, the welded injector is portrayed. After the injection, a single-hole GDI was obtained, as pictured in Figure 21c.

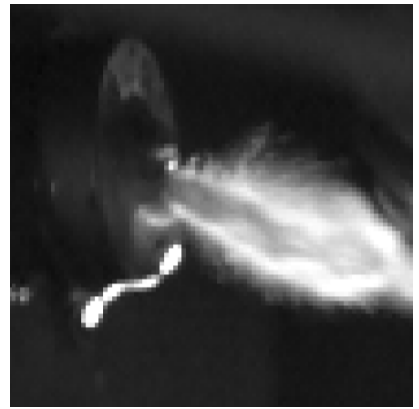
However, it was discovered a leakage after the welding, as the piston could not close after injection. A second attempt at welding the injector was conducted by sending a new injector to a cooperation group in Poland, yet, the leakage persisted.



(a) Not welded injector.



(b) Welded injector.



(c) Single-hole GDI.

Figure 21: Pictures of the GDI injector.

4 Results and Discussion

The results from the momentum flux, mass flux and shadowgraph imaging experiments will be presented in this section, with a discussion of the results obtained.

4.1 Momentum Flux

As described in Section 3.5, the force measured by the piezoelectric sensor is equal to the momentum flux in the axial direction. Figure 22 shows the ammonia spray out of the injector nozzle interacting with a target placed perpendicular to the plume, with labels to the different components portrayed. The target is placed 1.2 mm away from the injector tip.

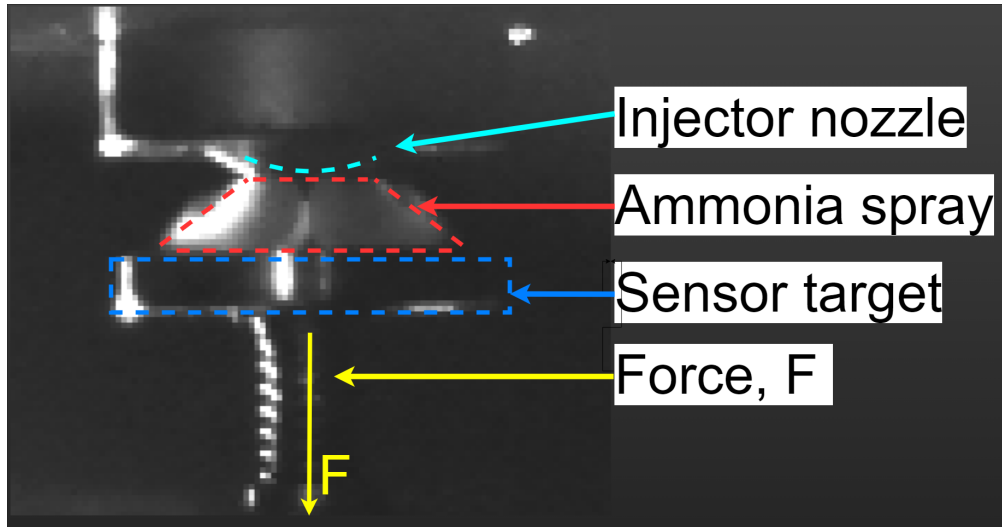
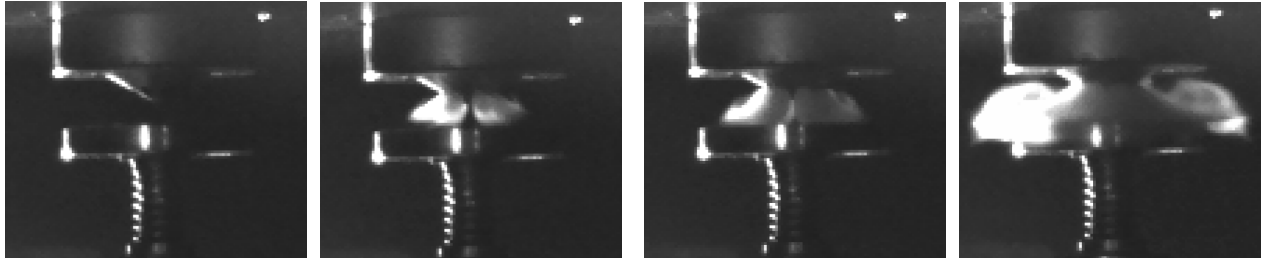


Figure 22: Spray Momentum.

Figure 23 displays the motion of the spray before and after impact with the sensor target. Figure 23a is immediately before the injection spray is visible, hence labelled as the beginning of the injection. Figure 23b is straight before the spray plume interacts with the sensor target, with the initial ammonia spray visible. In Figure 23c, the moment of impact between the spray and the target is portrayed, and Figure 23d pictures the movement of the spray while interacting with the target. The images show that the entire spray is captured by the target and is reflected in a lateral manner.

As the ammonia spray interacts with the target, the axial momentum flux is measured



(a) The beginning of the injection. (b) 0.0188 ms after injection start. (c) 0.0250 ms after injection start. (d) 0.0438 ms after injection start.

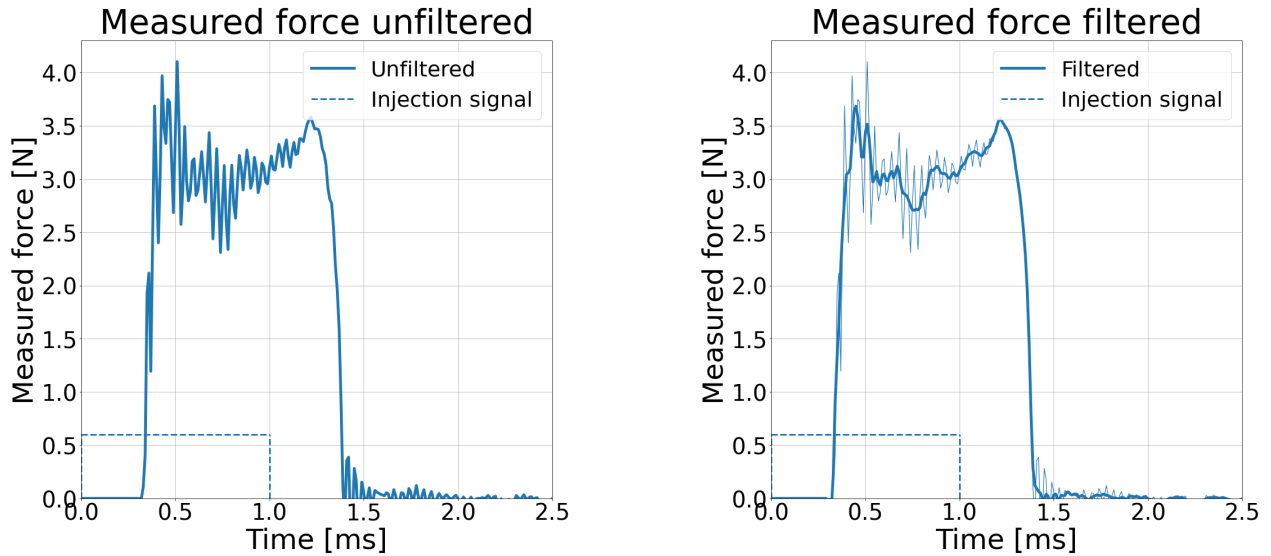
Figure 23: Ammonia spray development out of the injector, with a spray target presented to the emerging spray.

by the piezoelectric sensor. Figure 24 presents plots based on the average of 15 injections, executed at the same condition as the injection portrayed in Figure 23. The energizing time of the injections is 1 millisecond (ms), and the signal to the injector is portrayed as the dotted lines in the graphs. For the plots displayed, the injection pressure of ammonia is 200 bar, and the chamber pressure is set at 2 bar. In the graphs, the x-axis is the time scale in ms, and the y-axis is the measured force in Newton (N). The graphs show an increase in momentum during the injection period: a force is introduced by the spray to the piezoelectric sensor at approximately 0.36 ms. After the injection, at $time \approx 1.36ms$, there is no more spray exiting the injector, hence, no more force interacting with the sensor. Consequently, approximately 1.36 ms after the start of energizing, the graph declines to zero.

Figure 24a portrays the unfiltered force measurement. As seen from the plot, there is an oscillating tendency in the force signal during the injection. This tendency may be caused by noise in the measurements from external disturbances. By reviewing the beginning of the diagram, there are no oscillations, which may indicate that the external disturbances are minor. However, another explanation for the oscillation tendency can be disturbances related to the density change between the ambient nitrogen gas and the ammonia spray, with the injection particles having a vibrating effect on the sensor target, resulting in fluctuation.

Displaying the unfiltered signals from the piezoelectric sensor can give a disorganised presentation of the results. Figure 24b portrays the filtered force measurements of the injections. Here an infinite impulse response (IIR) filter has been used on the data, resulting in a clearer representation of the data. Most of the noise from the measurements is filtered out, and the

oscillations are smaller, as can be seen when compared to the original graph shown in the background of the plot.



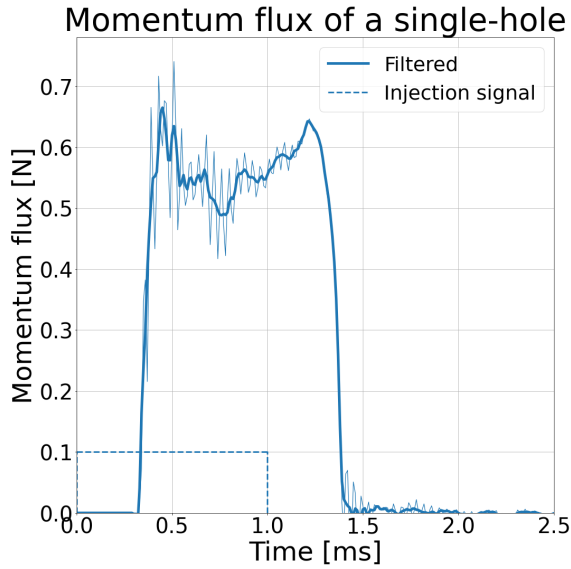
(a) The measured force signal from the transducer unfiltered.

(b) The measured force signal from the transducer filtered.

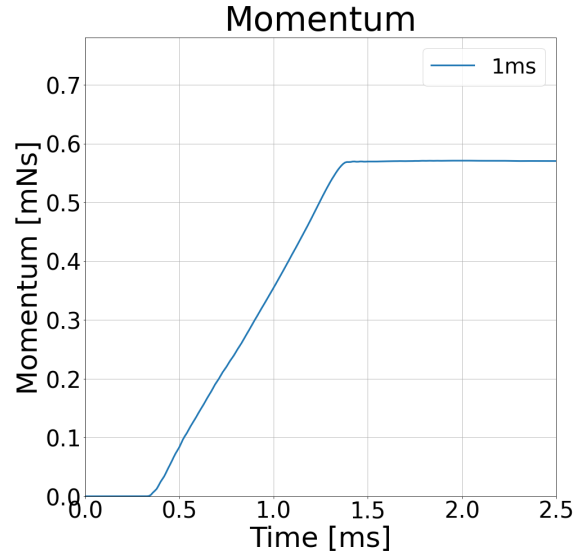
Figure 24: Graphs representing the average of 15 injections with an injection duration of 1 ms, p_{inj} at 200 bar and p_{amb} at 2 bar.

The graphs in Figure 24 portray the measured force, which is equal to the axial momentum flux of the spray. As explained in section 3.5, the sprays interact with the target at an angle which is due to the hole geometry of the injector. The momentum flux of a single hole can be obtained by employing Equation 10 on the measurements acquired on the force, combined with angle θ from Table 2. The calculated momentum flux out of a single hole of the injector is displayed in Figure 25a.

Having the momentum flux of a single hole of the GDI injector can be used to calculate its change in momentum. The integrated momentum flux is portrayed in Figure 25b. For the integrated momentum flux is the force, in Newton, multiplied with the change in time, in milliseconds, giving unit mNs.



(a) The momentum flux for a single hole of the GDI injector.



(b) The integrated spray momentum flux for a single hole of the GDI injector.

Figure 25: Graphs representing the average of 15 injections with an injection duration of 1 ms, p_{inj} at 200 bar and p_{amb} at 2 bar.

4.2 Alignment of the Piezoelectric Sensor

4.2.1 Spray target size

As mentioned in Section 3.5.2, new spray targets were produced and tested as it was suspected that the original target was too narrow to capture the entire spray impingement area. The results from the momentum measurements of the different target sizes are shown in Figure 26, where the momentum flux is illustrated in 26a and the following integrated momentum flux is displayed in Figure 26b. In both figures, each line represents the average of measurements based on 15 injections for a given target size, for an injection pressure of 200 bar and an ambient pressure of 2 bar.

As displayed in the plots, there is a distinguishable difference between the original spray target of 4 mm and the 6 mm, 7 mm, 8 mm and 9 mm spray targets. This indicates that the smallest spray target was unable to capture the entire momentum of the ammonia spray; if the impingement area of the spray is wider than the spray target, a significant portion of the spray will not be captured. Consequently, this will give a lower measurement for the momentum.

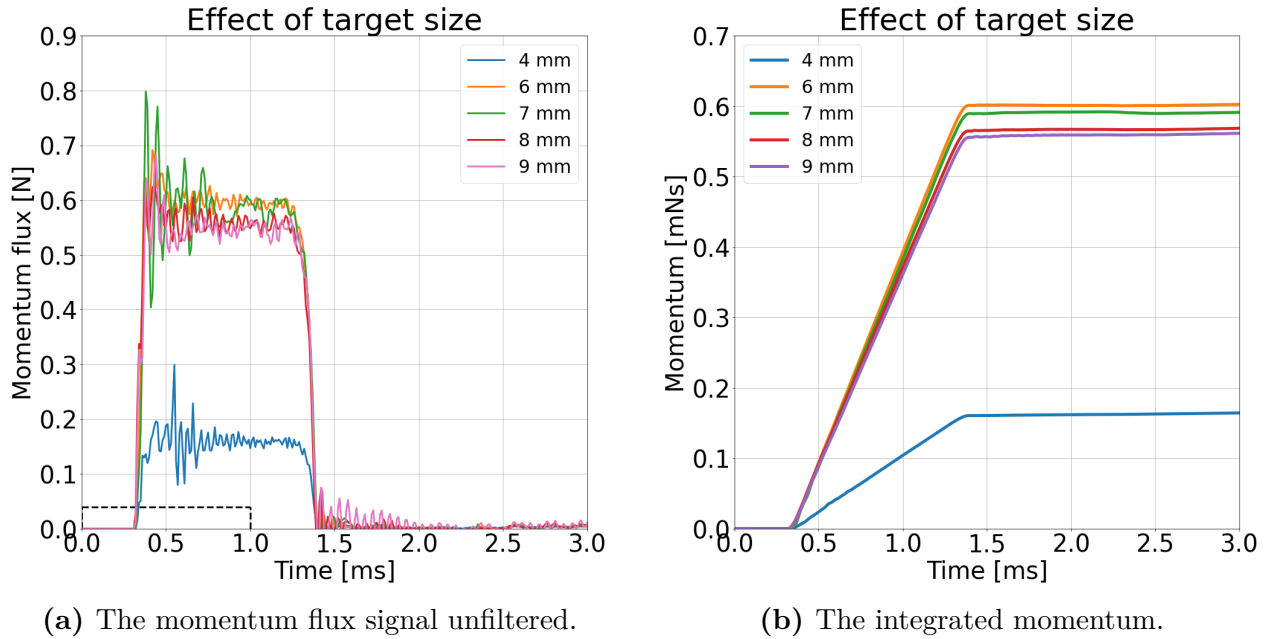


Figure 26: Graphs representing measurements performed with different target sizes, where each graph is calculated for a single hole of the GDI injector at a target size ranging from 4 mm to 9 mm.

For the wider spray targets, there are smaller differences in the measured momentum. Some of the deviations in the measurement can be caused by variations in the alignment of the spray target. An identical position for the spray target was strived for, but some deviations in position are to be expected.

It was noted that the 8 mm and 9 mm spray targets have a higher tendency of oscillation after the end of injection (EOI). This can be observed in Figure 26a from 1.4 ms after the start of energizing, and is particularly dominating for the 9 mm spray target. An explanation for this observation can be that the spray targets are too wide in comparison to the screw, resulting in more instability when the particles interact with the target, which gives more significant vibrations. This may also slightly affect the measured momentum flux during the injection process, which could explain why the measurements are lower for the 8 mm and 9 mm spray targets compared to the 6 mm and 7 mm spray targets. The instability and oscillation tendencies may partially disrupt the measurements, providing a possible explanation for why the 9 mm spray target has the lowest measurement among the four.

The spray target of 6 mm and 7 mm gave the highest measurements for the momentum while not having the oscillatory tendency after the end of energizing. Consequently,

both targets were considered suitable, and a spray target of 7 mm was chosen for further experiments.

4.2.2 Effect of distance to the spray target

The concept of varying the distance between the spray target and the injector tip was explained in Section 3.5.1. The assumption is that the position giving the highest momentum is considered to be the optimum position. The results from varying the distance are summarized in Figure 27. In the figure, each point represents the average of the integrated momentum flux from 15 injections for the given position.

The plot shows a reduction in momentum for measurements further away than 3.5 mm, and these are marked as green points in the plot. An explanation for the reduction in momentum can be due to the spray impingement area being too wide for the spray target. If the spray impingement area is wider than the sensor target, naturally, some of the spray momenta will not be captured.

Another observation is that the further away the target is from the injector, the more significant the drop in momentum. This is shown as the gap between the two green points. This can be explained by a more substantial portion of the spray not interacting with the force transducer due to the spray becoming wider as it penetrates further away from the nozzle holes. Accordingly, less of the momentum of the spray is captured by the spray target.

For the positions marked as blue in the plot in Figure 27, there was no significant change in the integrated momentum. Hence, the length from the spray target to the injector tip did not significantly affect the momentum.

This is similar to results gathered by Payri et al., who presented outcomes for measurements at 1.8, 2.3 and 2.8 mm [29]. It was noted for low ambient pressures, there was no significant difference in the mean value of the momentum flux for the different distances. However, this changed when ambient pressure was increased, which caused the spray to become wider. This resulted in lower measurements of the momentum flux for spray targets placed further away.

There are some uncertainties in the results presented. The measurements shown in Figure 27 are based on an ambient pressure of 2 bar. However, the momentum flux experiments were

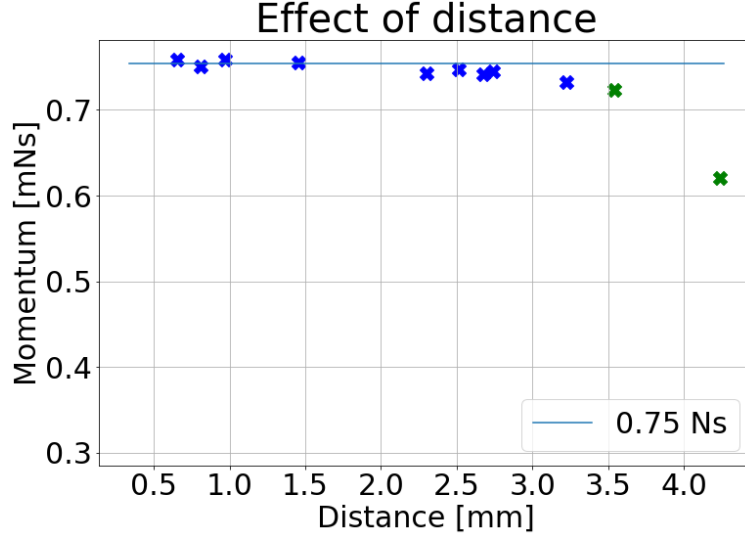


Figure 27: Momentum results from varying the distance between the spray target and injector tip. Each point represents one position, which is the average of 15 injections in the given position, for $p_{inj} = 205$ bar, $p_{amb} = 2$ bar. A line is included to show the maximum momentum obtained.

conducted at an ambient pressure ranging from 2 bar up to 20 bar. Considering the results obtained by Payri et al. when increasing the ambient pressure, the distance to the spray target was more influential as the ambient gas obstructed the spray propagation. Accordingly, it was regarded as important to keep the spray target close to the injector tip.

Consequently, for the experiments in this thesis, the spray target was kept near the injector, approximately 1.2 mm away from the injector tip.

4.2.3 Effect of spray target angle

The concept of varying the target angle relative to the spray was explained in Section 3.5.1, and the results from varying the angle are summarized in Figure 28. Each point in the plot represents the average momentum for that given position, calculated by taking the average of 15 injections.

As illustrated in the plot, the position giving the highest measurement for momentum is perpendicular to the spray. This position is labelled as M_{max} and marked with a green point in the plot.

As M_{max} is the position giving the highest measurement for the momentum, this is consid-

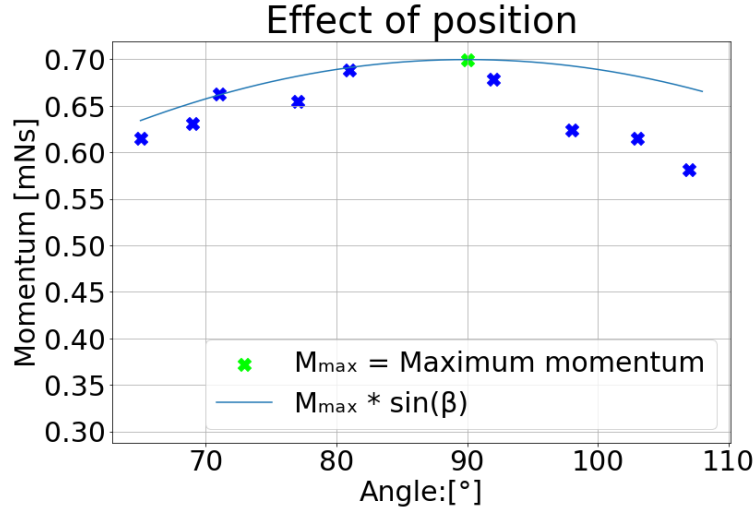


Figure 28: Momentum results from varying the angle of the spray target relative to the injector tip. Each point represents one position, taking an average of 15 injections of said position, for $p_{inj} = 200$ bar, $p_{amb} = 2$ bar. The graph includes $M_{max} \sin(\beta)$: the theoretical measurement of the momentum, and the green point represents M_{max} .

ered to be the optimum angle for the spray target. This can also be evaluated by performing a force analysis of the spray target relative to the injector spray.

Figure 29 displays a force analysis of the sensor being placed at different angles β relative to the spray. In the figure, F refers to the measured momentum flux, and S refers to the axial momentum flux of the Spray. For a perpendicular position: $\beta = 90^\circ$, accordingly $\sin(\beta) = 1$. Thus, the measured momentum flux is equal to the axial momentum flux of the spray: $S = F$.

This is confirmed in the plot in Figure 28, as the highest obtained momentum flux is for a target placed 90° relative to the spray. Therefore, placing the spray target perpendicular to the spray gives the most precise measurement of the momentum.

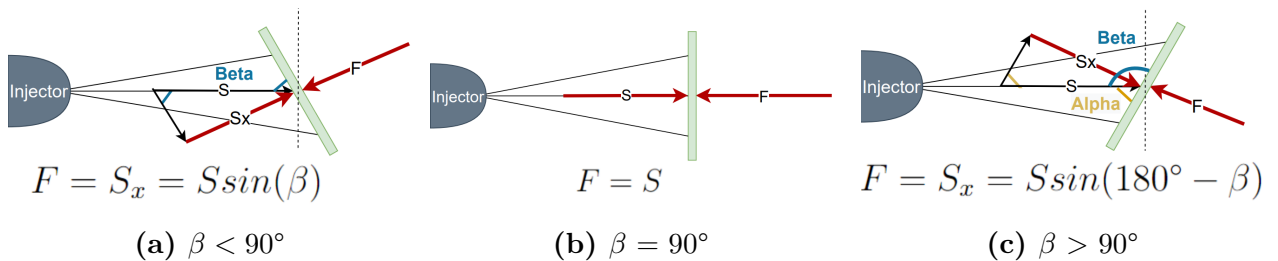


Figure 29: Varying the angle of the sensor relative to the spray, β , from a steep (a) to a perpendicular (b) to an obtuse (c) angle. In the figures, vector S is equal to the actual momentum flux of the spray, and F equals the momentum flux measured by the piezoelectric sensor.

4.3 Momentum flux results

4.3.1 Varying the injection pressure

Results from varying the injection pressure from 100 bar, 150 bar to 200 bar are shown in Figure 30, where Figure 30a show the momentum flux and Figure 30b displays the integrated momentum flux. For these measurements, the ambient pressure was kept constant at 2 bar, and the energizing time was 1 ms.

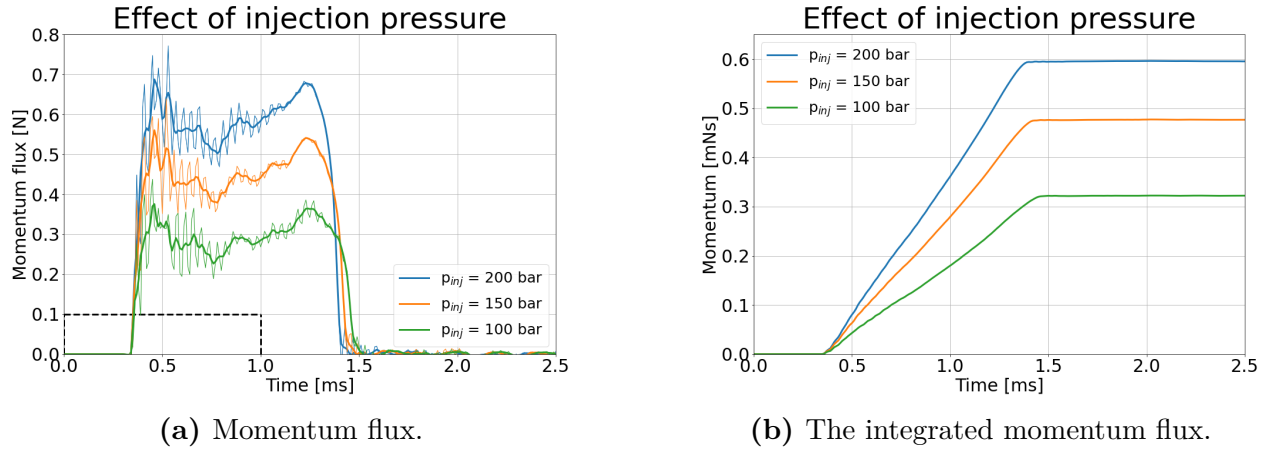


Figure 30: Graphs representing the average of 15 injections with an injection duration of 1 ms and p_{amb} at 2 bar, with varying injection pressure.

As observed in Figure 30a, the momentum flux peak is reached for all the injections approximately 0.48 ms after the start of energizing (ASE). The momentum flux decreases between 0.48 ms to 0.77 ms ASE. Then the momentum flux increases again until 1.25 ms ASE, before the injector needle closes and the momentum flux declines to zero.

From Figure 30b is observed that an increase in injection pressure gives an increase in the momentum flux of the spray. This can be correlated to Bernoulli's equation and the momentum flux equation from the Theory chapter.

From the Bernoulli equation, a correspondence between the pressure difference and the velocity of the liquid jet was obtained:

$$u_{th} = \sqrt{\frac{2\Delta P}{\rho_l}} \implies u_{th} \propto \sqrt{\Delta P} \quad (13)$$

Similarly, from the equation for the measured momentum flux, 9, a correspondence be-

tween the measured momentum flux and the velocity of the liquid jet can be obtained:

$$\dot{M} = \rho A u_{eff}^2 \implies u_{eff} \propto \sqrt{\dot{M}} \quad (14)$$

By combining Equation 13 and 14, a correlation between the momentum flux, \dot{M} and the pressure change, ΔP , is acquired, portraying that the momentum flux is proportional to the pressure change: $\Delta P \propto \dot{M}$

From Figure 30, the correlation is affirmed: a more significant pressure drop between the injector and back pressure, ΔP , provides a higher momentum flux. For an injection pressure of 200 bar, 150 bar and 100 bar, the integrated momentum flux is 0.60 mNs, 0.48 mNs and 0.32 mNs, respectively.

The ratio for the change in pressure from the injector to the chamber, for an injection pressure between 200 bar and 100 bar, is given in Equation 15. The ratio for the change in pressure is compared to the corresponding ratio for the momentum flux, which is given in Equation 16.

$$\Delta P_{200bar/100bar} = \frac{200bar - 2bar}{100bar - 2bar} = 2.02 \quad (15)$$

$$\dot{M}_{200bar/100bar} = \frac{0.60N}{0.32N} = 1.88 \quad (16)$$

Similarly, the results for an injection pressure of 150 bar were compared to an injection pressure of 100 bar, giving the following results for the ratios:

$$\Delta P_{150bar/100bar} = \frac{150bar - 2bar}{100bar - 2bar} = 1.51 \quad (17)$$

$$\dot{M}_{150bar/100bar} = \frac{0.48N}{0.32N} = 1.50 \quad (18)$$

As shown by these equations, the ratios for the change in pressure and momentum flux are comparable. This indicates that the main portion of the momentum flux decrease is connected to the decrease in the injection pressure. From the results in Equations 17 and 18, it is observed a good correspondence between the pressure change and momentum change for injection pressures of 150 bar and 100 bar, confirming the correlation between the change

in pressure and the momentum flux.

However, there is a greater dissimilarity for the injection pressure of 200 bar, referring to Equations 15 and 16. The momentum flux for an injection pressure of 200 bar is smaller than expected. It is reported that when increasing the injection pressure of the ammonia spray, more turbulence is induced in the spray [42]. An explanation for the slightly lower measurements of momentum flux for an increasing injection pressure may be related to this increased turbulence in the spray. Having a more turbulent spray may influence the direction of the spray particles, resulting in some of the spray particles not interacting perpendicularly with the spray target; thus, a portion of the momentum flux may not be entirely collected by the force transducer.

4.3.2 Varying the ambient pressure

Results from varying the ambient pressure from 2 bar, 10 bar to 20 bar are shown in Figure 30, where Figure 30a show the momentum flux and Figure 30b displays the integrated momentum flux. For these measurements, the injection pressure was kept constant at 200 bar, and the energizing time was 1 ms.

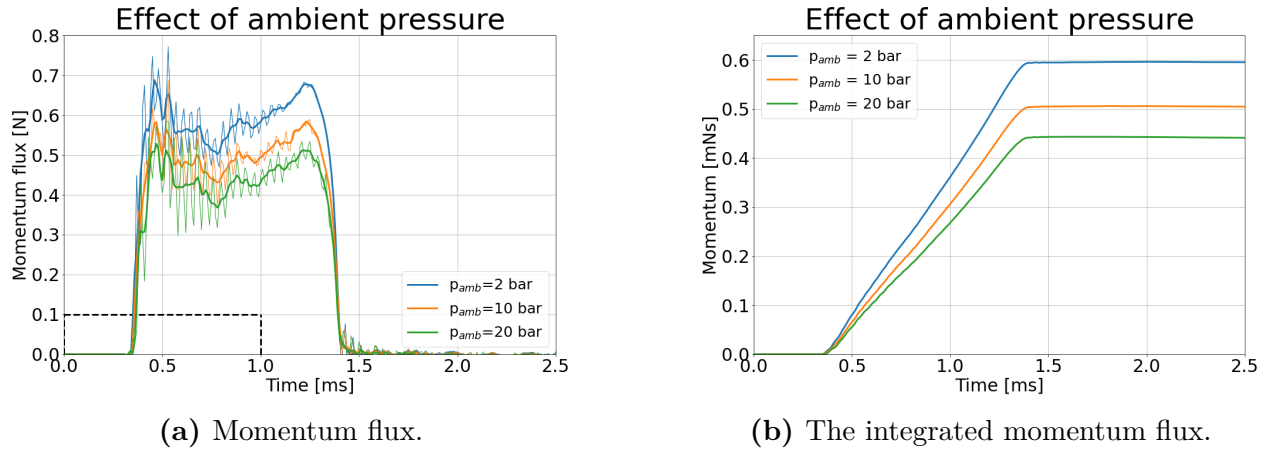


Figure 31: Graphs representing the average of 15 injections with an injection duration of 1 ms and p_{inj} at 200 bar, with varying ambient pressure.

From Figure 31, it is observed as the ambient pressure increases, the momentum flux decreases. This can be related to the fact that as the ambient pressure increases, the chamber density increases, resulting in a larger ambient drag force which obstructs the spray

propagation.

To achieve an estimate of the influence of the increased chamber density, followed by an obstruction of the spray propagation, the change in pressure can be compared to the momentum flux. Similarly as in Section 4.3.1, Equation 19 shows the calculated ratio of the change in pressure and Equation 20 shows the ratio of the momentum flux.

$$\Delta P_{2bar/20bar} = \frac{200bar - 2bar}{200bar - 20bar} = 1.1 \quad (19)$$

$$\dot{M}_{2bar/20bar} = \frac{0.60N}{0.44N} = 1.36 \quad (20)$$

As observed from the ratios calculated in Equations 19 and 20, there is a greater discrepancy for varying the ambient pressure than when varying the injection pressure. This is expected due to the higher density obstructing the spray propagation, as mentioned above.

Consequently, this can cause uncertainties in the measurements for the momentum flux, indicating that the ambient gas interferes with the spray propagation, causing a lower measurement for the momentum flux. This is similar to the results obtained by Payri et al. [29], hence strengthening the motivation for keeping the spray target closer to the injector and thereby minimizing the disturbance from the ambient gas to the spray momentum.

4.3.3 Injection energizing

Figure 32 shows the measured momentum flux for different injector energizing periods of 1 ms, 2 ms and 3 ms, with time. The corresponding energizing periods of the injector are illustrated as the dashed lines in the bottom left of the graph.

As observed in the figure, there is a good correspondence between each of the injection energizing periods, as each of the graphs overlaps. Hence, the variations seem to be equivalent at a given time after the start of energizing.

From the figure, it is observed a fluctuating tendency, with the most prominent declination being between 0.48 ms and 0.77 ms after the start of energizing (ASE). This initial declination can be caused by the injector being unable to keep the pressure at the initiation of the injection due to the sudden flow of ammonia once the needle is opened. This results in a dip in the pressure, hence a drop in the measured momentum flux.

Afterwards, the pressure steadily builds up until the peak at 1.5 ms ASE. However, there is a smaller declination between the peak in 1.5 ms ASE and 2.25 ms ASE, before the momentum flux again increases to 3.25 ms ASE. This variation may be caused by the pressure fluctuations. The pressure is not entirely constant but fluctuates as the nitrogen is supplied, thereby not keeping a constant ammonia flow out of the injector once the needle is open.

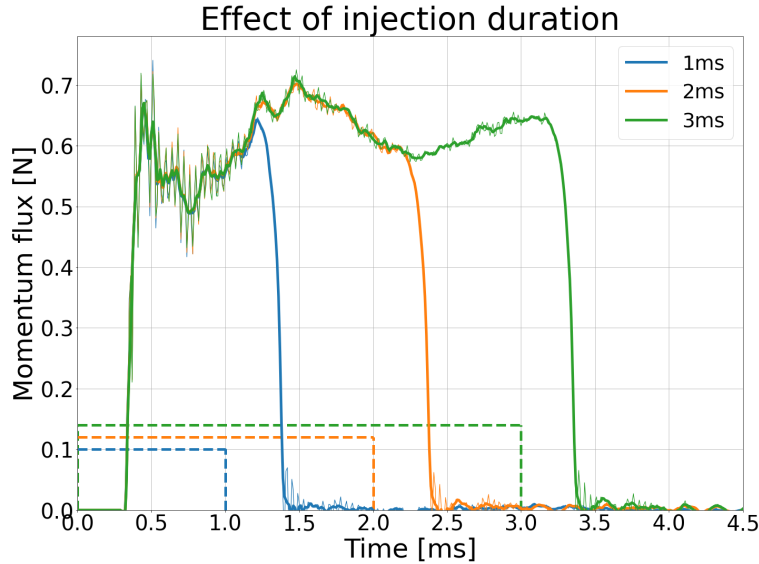


Figure 32: Spray momentum flux at different energizing durations, varying from 1 ms to 3 ms.

4.3.4 Injection timing and delay

As mentioned in Section 2.3, injection strategies, including injection timing, are important for determining engine performance. Thus, having insight into the timing of the current injector is of interest.

The energizing time of the injections is 1 ms for the measurements portrayed in Figure 25. As can be observed in the graphs, the piezoelectric sensor is activated between 0.36 ms and 1.36 ms, meaning the signal is read by the force transducer 0.36 ms after the start of energizing (ASE). Accordingly, there is a delay from the start of energizing in the control software to the measurement of momentum flux is occurring.

Part of the delay can be caused by an "electronic delay" in the control hardware, likely

dominated by a delay in the injector driver [33]. Considering the delay is caused by the electronics, this portion of the delay is assumed to be constant for all injections.

As mentioned by Emberson et al. in [33], part of the delay can also be from a "hydraulic delay", which is the portion of the delay depending on the given conditions for the injection. It is observed that a change in the ambient pressure (hence ambient density) impacts the start of injection (SOI), as portrayed in Figure 33a. From this figure, it is noticed that increasing the ambient pressure causes an increased delay of the SOI. As the ambient pressure is increased from 2 bar to 20 bar, the SOI is delayed with 15 μ s.

An explanation for this occurrence could be from the injector geometry. The injector has a mushroom valve which is held closed by a spring and the fuel system pressure. In Figure 33a, the fuel system pressure is set at 200 bar. By reducing the ambient pressure, the pressure drop over the nozzle is higher, which could result in a higher force keeping the injector shut.

If the pressure drop has an impact on the SOI, can be inspected by changing the fuel system pressure while keeping the chamber pressure constant. This was investigated by decreasing the injection pressure from 200 bar to 100 bar while keeping the chamber pressure at 2 bar, as presented in Figure 33b. However, as portrayed in this figure, the SOI is occurring at the same moment, hence, the SOI appears to be independent of the injection pressure.

An explanation for the delay in SOI (depicted in Figure 33a) could be a decreased velocity of the spray out of the injector, affected by the increased chamber density, meaning the spray takes longer to reach the spray target.

The end of injection (EOI) appears at the same instant for constant injection pressure, as pictured in 33a. Hence, EOI appears to be independent of the chamber pressure. The explanation for this could be at a given injection pressure, the mushroom valve is shut at the same instant. The EOI is delayed by decreasing the injection pressure, as depicted in Figure 33b. This could be caused by the mushroom valve being operated at a different condition when the pressure in the nozzle changes. By having a higher injection pressure, a greater force is introduced when shutting the injector, leaving the injector to close faster. For a lower injection pressure, a smaller force is needed, and the injector takes longer to shut. This can be supported by the last apexes of the graphs, which occur at approximately the same time

(at 1.25 ms). Hence it seems the injector begins closing at the same instant but takes longer at a lower injection pressure.

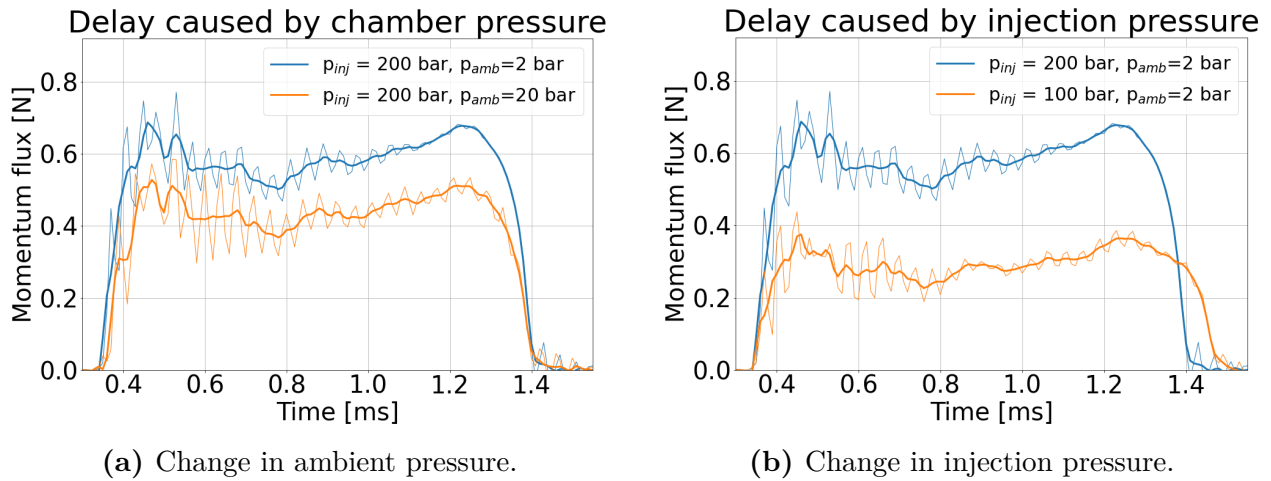


Figure 33: Graphs to review any correlations between delay and chamber pressure or injection pressure.

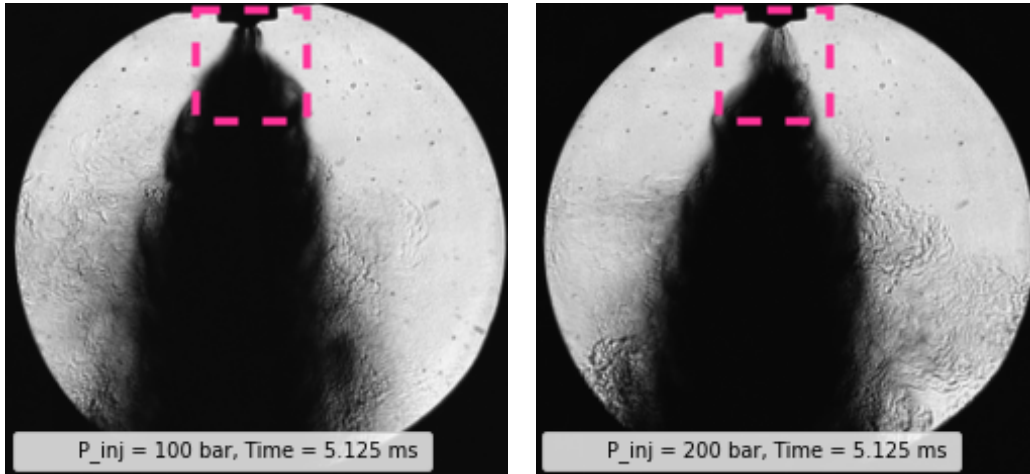
Two consequences regarding delay were experienced: by increasing the chamber pressure, the injection period was slightly shortened. By decreasing the injection pressure, the injection period was slightly increased.

Shadowgraph imaging was used to confirm that the end of injection occurred at different periods for a change in injection pressure, as portrayed in Figure 34. In the figure, the two images are at the same instant. The pictures portray the ammonia flow out of the injector, highlighted with dotted squares, showing that the injection ceases earlier for an injection pressure of 200 bar than 100 bar.

4.4 Mass injected

The injected mass flux was measured at an ambient pressure of 2 bar, 10 bar and 20 bar, portrayed in Figure 35 as green, red and blue markers, respectively. Each injection was for a duration of 1 ms. The pressure of the fuel injected varied from 100 to 200 bar. The x-axis in the figure shows the square root of the change in pressure, where dp is the difference between the injection pressure and the chamber pressure.

Each marker represents the average injected mass for 500 injections, with the exception of the black marker representing the average of 2,500 injections. The frequency of injections



(a) Picture of injection at 100 bar, 5.125 ms after SOI. (b) Picture of injection at 200 bar, 5.125 ms after SOI.

Figure 34: Pictures from shadowgraph imaging at the end of injection.

marked with colours was 0.33 Hz, meaning an injection every third second. The injections marked as black had an injection frequency of 0.11 Hz.

From Figure 35, there is a linear dependency between the measured injected mass and the pressure change between the ambient pressure and the injection pressure. This linear dependency is illustrated as the dotted lines in the plot.

An injection frequency of 0.33 Hz was chosen to have frequent injections without having any significant cooling of the injector tip and chamber. By having this frequency, combined with constant flushing of the chamber, the chamber temperature was kept close to room temperature at 16°C. These measurements were verified by the injection frequency of 0.11 Hz, illustrated as the black point.

However, due to there not being any combustion and the injector being operated for approximately 8,000 injections each day on repeat, the injector tip was presumably cooled down. During the experiments performed on mass flux, two injectors began leaking, being unable to shut at elevated pressures. Hence, this leaves uncertainties in the results obtained: the leakage could have occurred before it was discovered. However, there is a good alignment to the linear tendency with several experiments conducted with different injectors.

Another uncertainty can be related to the temperature of the injector tip. The temperature of the injector tip was unknown, but considering the saturation temperature of ammonia,

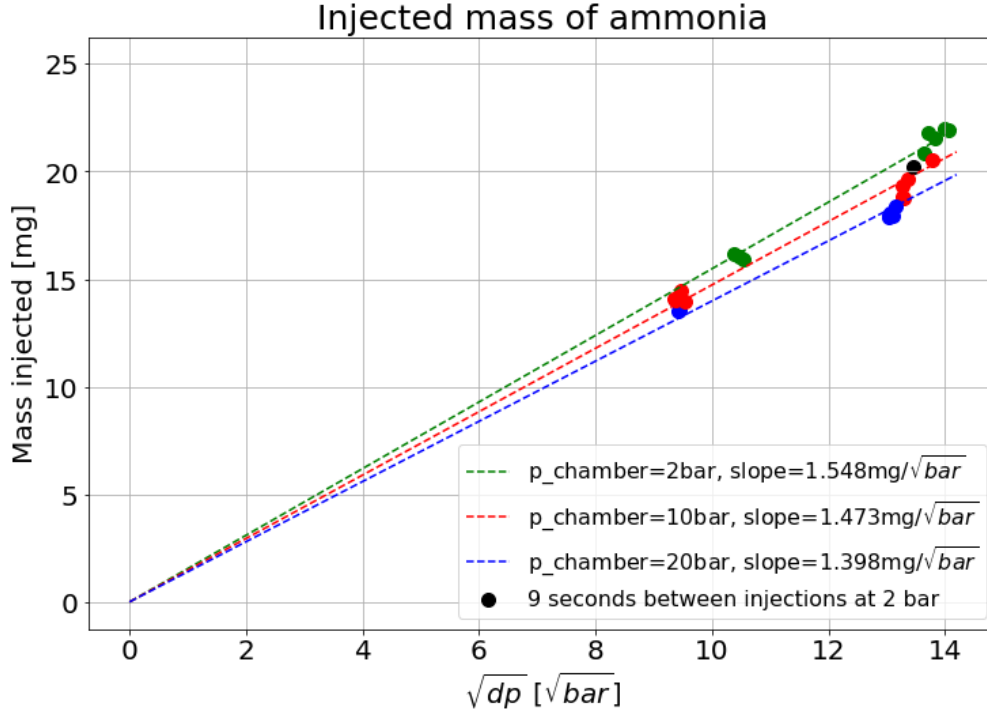


Figure 35: The injected mass of ammonia, where each of the coloured markers represents the average injected mass for 500 injections. One exception of the black point which represents the average of 2500 injections

it was potentially cooled down during the experiments. Hence, there is uncertainty as to how much the tip was cooled and how this temperature would affect the flow through the injector.

4.5 Mass flux and discharge coefficient

From Equations 6 and 7 presented in the theory section, using the momentum flux measurements combined with the measurements on the injected mass of ammonia, the mass flow rate and the discharge coefficient were calculated and plotted.

In Figure 36a, the calculated mass flow rate of ammonia is depicted. The plot shows the mass flow rate dependent on time for an energizing time of 1 ms. In the graph, the total mass injected for all 6 holes is portrayed at an injection pressure of 200 bar and a chamber pressure of 2 bar, 10 bar and 20 bar. The unfiltered mass flow rate is illustrated in the background of the plot.

Figure 36b portrays the calculated discharge coefficient, using the mass flow rate from Figure 36a. As the discharge coefficient portrays the actual mass flux over the theoretical

mass flux, the discharge coefficient is an indication of how smoothly the flow passes through the nozzle orifice. In the plot, the discharge coefficient is displayed dependent on time, and the corresponding calculated discharge coefficients are shown in the top corner of the plot.

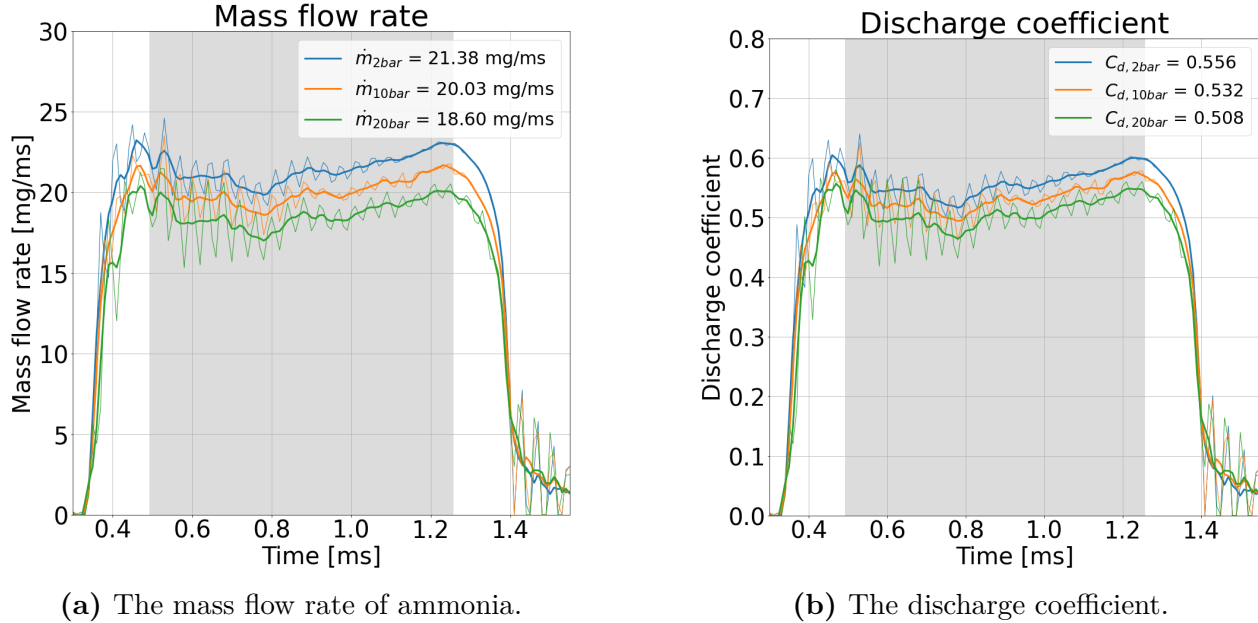


Figure 36: Graphs showing calculations of mass flow rate and discharge coefficient for $p_{inj}=200$ bar with a chamber pressure at 2 bar, 10 bar and 20 bar.

As seen from Figure 36b, the discharge coefficient was found to be 0.556 for a chamber pressure of 2 bar, 0.532 for a chamber pressure of 10 bar and 0.508 for a chamber pressure of 20 bar. The discharge coefficient is considerably lower for ammonia than for conventional fuels. As described in [33], the discharge coefficient for conventional fuels such as diesel is above 0.8.

An explanation for the lower discharge coefficient of ammonia compared to conventional fuels can be related to the shape of the injector combined with ammonia's high saturation pressure, causing ammonia to be vaporized inside the nozzle. Due to the cavitation behaviour, more vapour is injected, resulting in a lower liquid fraction of the spray; hence less mass is injected.

An observation from the results is that the discharge coefficient decreases with increasing chamber pressure. Thus, an increase in ambient density in the chamber resulted in a reduction in the discharge coefficient. This is surprising, as it was expected that a lower chamber

pressure would influence the cavitation behaviour, resulting in a lower discharge coefficient for 2 bar than for 10 bar due to more vapour injected.

However, the decrease in the discharge coefficient with an increase in chamber pressure can be linked to the pressure drop across the nozzle. When the pressure drop increases from 180 bar (at $p_{amb} = 20$ bar) to 198 bar (at $p_{amb} = 2$ bar), the discharge coefficient increases from 0.508 to 0.556. Having a higher pressure drop resulted in both a higher mass flow rate and a higher discharge coefficient. The higher mass flow rate can be connected to the pressure drop across the nozzle, as Payri et al. [29] found a correlation between the injected mass and the square root of the pressure drop. However, this was noted for non-cavitation conditions.

As reported in [29]: under cavitation conditions, the mass flow does not increase further when the discharge pressure (ambient pressure) is reduced if the injection pressure is kept constant. As shown in Figure 36a, when the discharge pressure is reduced from 20 bar to 2 bar, the mass flow rate increases, which could indicate that there is no significant cavitation in the injector at a chamber pressure of 10 bar and 20 bar. However, the mass flow rate at pressures between 2 bar and 10 bar is unknown; thus, it remains unknown when the mass flow collapses due to cavitation. Consequently, for further work, inspecting the mass flow at ambient pressures between 2 bar and 10 bar could be of interest.

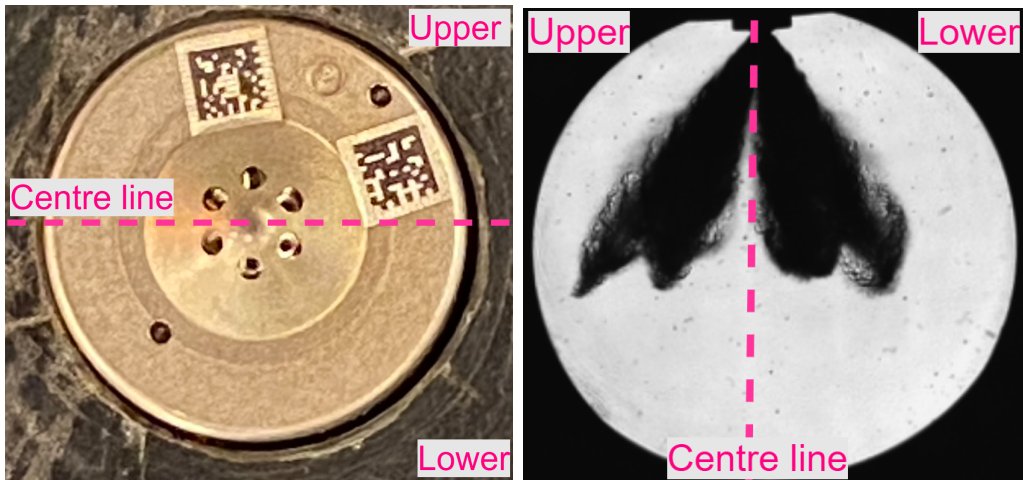
4.6 Shadowgraph imaging

Table 6 and Table 7 portrays how the ammonia spray behaved in the high-pressure chamber at a given time after the start of injection (SOI), for an injection pressure of 200 bar and 100 bar, respectively. The tables are included for a comparison of the spray shape at different moments after SOI. Using the shadowgraph imaging technique, both the phase of fluid and vapour are visible, with the fluid being completely black and the vapour appearing grey in the pictures.

In the tables, the ammonia spray at 0.25 ms, 0.50 ms, 0.75 ms, 1.0 ms, 3.0 ms and 5.0 ms after the SOI is included. The behaviour is shown at the different ambient pressures investigated, from 1 bar, 2 bar, 4 bar, 8 bar, 10 bar, 20 bar and 30 bar; hence, the saturation-to-ambient pressure ratios (R_p) investigated were 8.6, 4.3, 2.1, 1.1, 0.9, 0.4 and 0.3

respectively. The reason for including a chamber pressure of 1 bar was to see how ammonia behaved at a fully flashing condition. It was also desired to investigate how ammonia behaves at different pressures below the saturation pressure of 8.57 bar at 20°C; thus, 2 bar, 4 bar and 8 bar were included. How ammonia is influenced at higher chamber densities is of interest; hence, 10 bar, 20 bar and 30 bar was included.

As shown in the tables, for a chamber pressure above 4 bar, there is a gap between what appears as two spray jets. In Figure 37a, the orientation of the GDI injector is depicted. Figure 37b shows the injection spray for the given orientation. In both figures, the corresponding centre line is included. From Figure 37b, the portion of the spray to the left of the centre line corresponds to the three holes above the centre line in Figure 37a, and the portion of the spray to the right of the centre line from Figure 37b corresponds to the three holes below the centre line in Figure 37a. As depicted by the figures, due to the chosen orientation, three and three of the spray jets overlap.



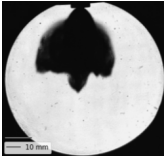
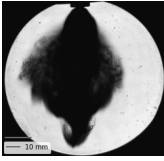
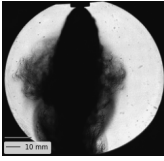
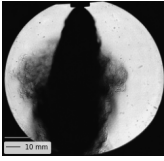
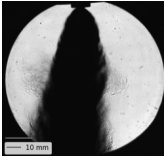
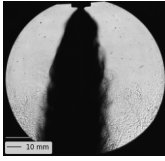
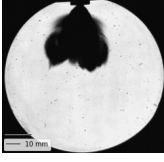
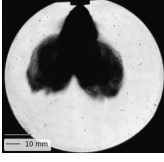
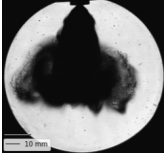
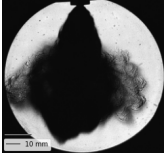
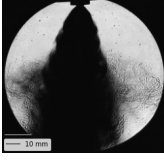
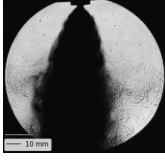
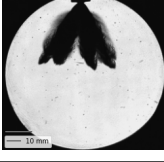


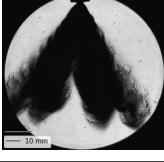
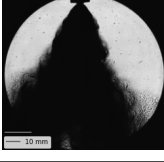
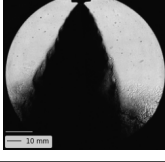
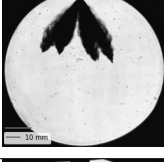
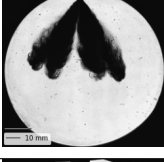
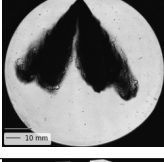
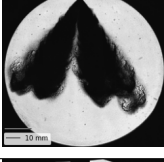
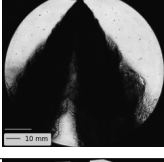
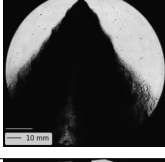
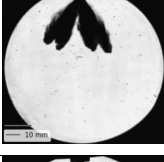
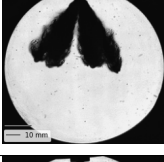
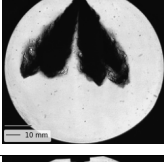
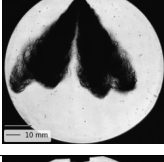
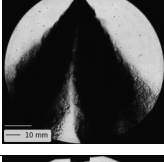
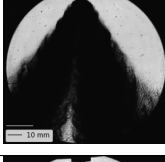
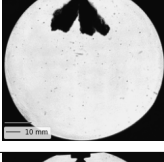
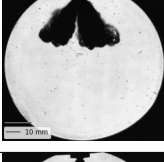
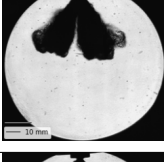
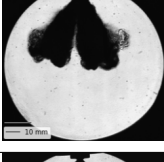
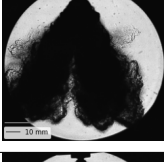
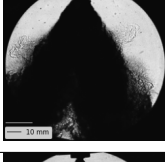
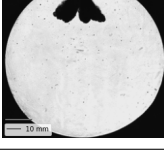
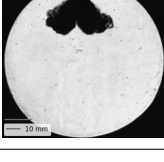
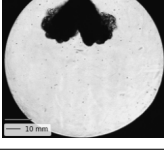
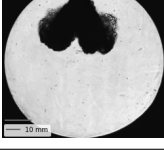
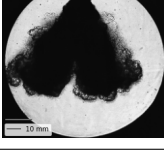
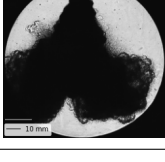
(a) Picture showing the orientation of the injector. (b) Picture of the spray out of injector with overlapping jets.

Figure 37: Pictures of the injector orientation.

4.6.1 Spray shapes

Due to ammonia’s saturation pressure of 8.57 bar at 20°C, different fuel characteristics and spray shapes are expected for a decreasing ambient pressure. This is related to the spray becoming superheated, resulting in different flash boiling conditions. A chamber pressure

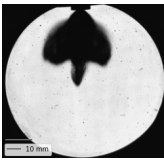
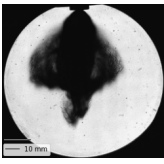
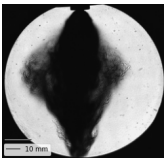
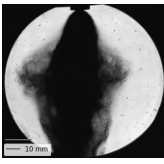
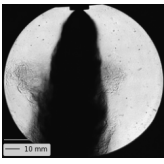
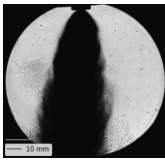
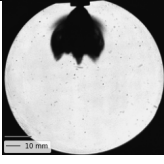
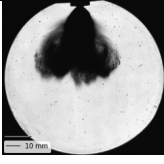
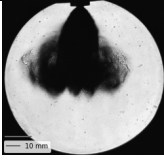
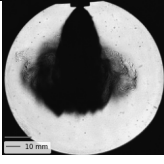
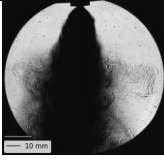
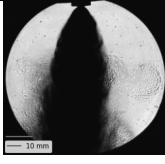
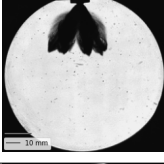
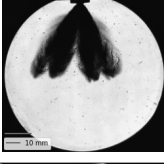
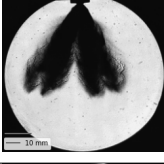
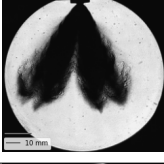
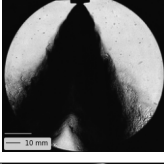
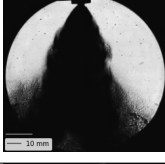
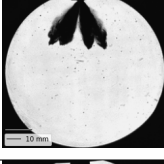
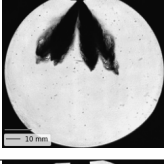
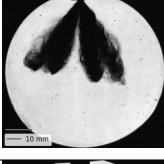
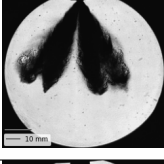
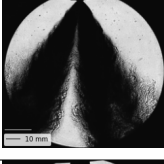
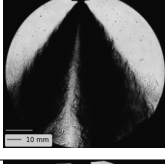
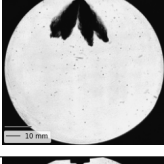
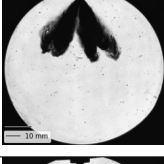
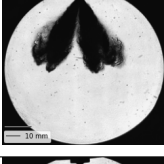
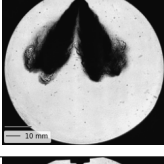
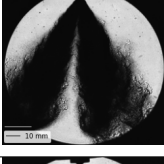
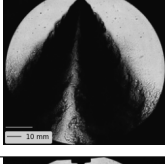
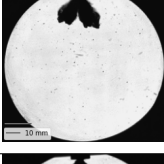
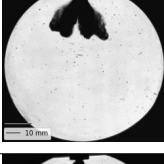
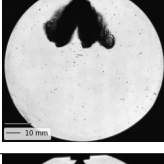
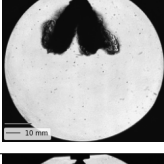
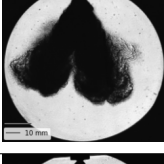
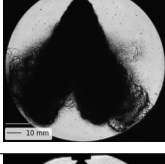
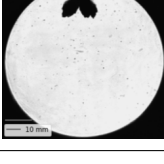
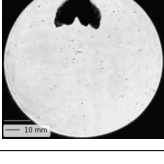
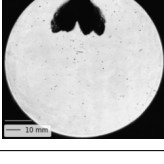
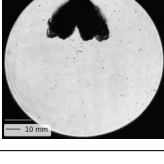
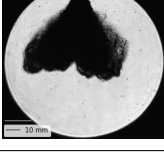
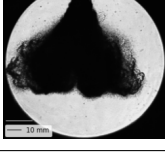
Table 6: Comparison of spray shape at 0.25 ms, 0.5 ms, 0.75 ms, 1 ms, 3 ms and 5 ms after the start of injection (SOI) for an injection pressure of 200 bar.

p_{amb}	0.25 ms	0.50 ms	0.75 ms	1.0 ms	3.0 ms	5.0 ms
1 bar						
2 bar						
4 bar						
8 bar						
10 bar						
20 bar						
30 bar						

equal to the saturation pressure is referred to as critical flashing, and a pressure just below the critical flashing is defined as initial flashing (for $1.0 < R_p < 2.0$).

From Table 7, looking at time 0.50 ms after SOI: a chamber pressure of 1 bar results in a significantly different spray shape. The picture is a good presentation of a fully flashing, or flare-flashing, spray. Looking at the picture, there is a cloud surrounding the spray centre; hence, a liquid core and droplets become superheated and generate a large number of

Table 7: Comparison of spray shape at 0.25 ms, 0.5 ms, 0.75 ms, 1 ms, 3 ms and 5 ms after the start of injection (SOI) for an injection pressure of 100 bar.

p_{amb}	0.25 ms	0.50 ms	0.75 ms	1.0 ms	3.0 ms	5.0 ms
1 bar						
2 bar						
4 bar						
8 bar						
10 bar						
20 bar						
30 bar						

internal bubbles. This can be explained by flash boiling phenomena, resulting in the droplets being nucleated and emerging with the gas layer surrounding the spray. The flare flashing phenomena is expected for an ambient pressure of 1 bar and has been reported in similar studies performed on single-hole GDI injectors [31] [43].

Additionally, there is an unexpected tendency of the spray observed. For a chamber pressure of 1 bar, the direction of the longest penetration of the spray is straight down. Hence,

the ammonia spray out of the six-hole GDI appears as a single jet, referring to Table 6 at 0.5 ms after SOI. This differs from the spray shapes for the other ambient pressures depicted at 0.50 ms after SOI, where the spray jets move in the direction of the nozzle holes. This can be explained by the flash boiling effect. As mentioned, when the nucleated bubbles burst, smaller droplets will be ejected along with the vapour gas into the surroundings simultaneously. Compared to traditional non-flashing liquid spray, flash boiling will accelerate both the atomization and evaporation process of the spray. Accordingly, the intensity and the efficiency of the flashing process are heightened compared to simple evaporation [31]. The appearance of the spray at 1 bar can be explained by the spray jets interacting out of the nozzle and by flash boiling, accelerating the spray in the centre of the jets, thus, leaving the spray to appear as a single jet.

For a chamber density of 2 bar, the spray shape also differs from the shape of the spray for the higher ambient pressures. The spray appears close to the flare-flashing condition. The spray has a saturation-to-ambient ratio (R_p) of 4.3, meaning it is in the transitional region ($2 < R_p < 5$), near a fully flashing condition (R_p). Initially, the liquid jets move in the direction of the nozzle holes, resulting in a shorter initial penetration length of 2 bar compared to 1 bar. However, at 0.75 ms after SOI, the spray jets interact, leaving the spray to appear like a single jet. Vortices start to form from 0.25 ms, and as the spray propagates, the vortices travel downwards. The flash boiling effect is less significant for an ambient pressure of 2 bar compared to 1 bar; this is expected due to the ambient pressure being slightly higher.

Both ambient pressures of 1 and 2 bar result in the spray jets merging into one spray jet as a result of flash boiling, significantly separating these two chamber pressures from the remaining.

When the chamber pressure increases to 4 bar, the spray shape appears to be merging toward a more similar shape to the higher ambient pressures. The shape is a characteristic triangular shape with more defined spray jets, referring to Table 7. As observed from the table, the spray is not fully flashing. For a chamber pressure of 4 bar, the pressure ratio is in the transitional flashing region, as the saturation-to-ambient pressure ratio is 2.1. There is a vapour zone surrounding the spray and a visual collapse of the spray.

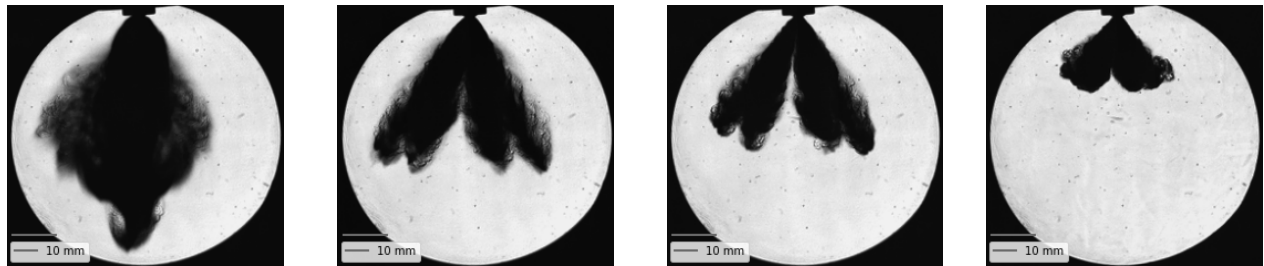
From the tables, it is observed that bubble behaviour gradually dominates the penetration

evolution under both transitional and flare flashing conditions. This behaviour of the spray is similar to results presented in [31].

Having an ambient pressure of 8 bar and 10 bar result in a relatively similar behaviour of the spray, referring to Table 6. A chamber pressure of 8 bar portrays the spray as initial flashing, being close to the critical flashing stage at the saturation pressure of ammonia, while 10 bar is just above the saturation pressure.

For an ambient pressure of 20 bar and 30 bar, the pressure in the chamber is considerably above the saturation pressure. For these pressures, the influence of the chamber density on the spray propagation is especially noteworthy, as the increased chamber density results in shorter penetration length with time and a more compact spray shape.

A summary of the different spray shapes for the different flash boiling conditions is shown in Figure 38: flare flashing at a chamber pressure of 1 bar (shown in Figure 38a), transitional flashing spray at a chamber pressure of 4 bar (shown in Figure 38b), initial flashing at a chamber pressure of 8 bar (shown in Figure 38c), and above critical conditions at a chamber pressure of 30 bar (shown in Figure 38d). Each of the images is for an injection pressure of 200 bar at 0.5 ms after SOI.



(a) Flare flashing spray: $P_{amb} = 1$ bar.

(b) Transitional flashing: $P_{amb}=4$ bar.

(c) Initial flashing spray: $P_{amb} = 8$ bar.

(d) Spray at $P_{amb} = 30$ bar.

Figure 38: Summary of the different spray shapes for the different flash boiling conditions: flare flashing, transitional flashing, initial flashing and above critical conditions. All pictures are for an injection pressure of 200 bar at 0.5 ms after SOI.

4.6.2 Spray penetration length and velocity

The penetration length of the spray was found by employing Python to iterate through the images, finding the point of the spray furthest away from the injector tip. Figure 39 depicts

an example from the post-processing of the spray penetration length for an injection pressure of 200 bar, referring to Table 6. The images show the spray at the same instant, 0.25 ms after SOI, at different ambient pressures. In the pictures, the spray penetration length, SP, and the angle at half penetration length are included. To provide a high sensitivity to the spray penetration length, the length scale is in pixel-lengths instead of mm, where 1 pixel-length is equal to 0.244 mm.

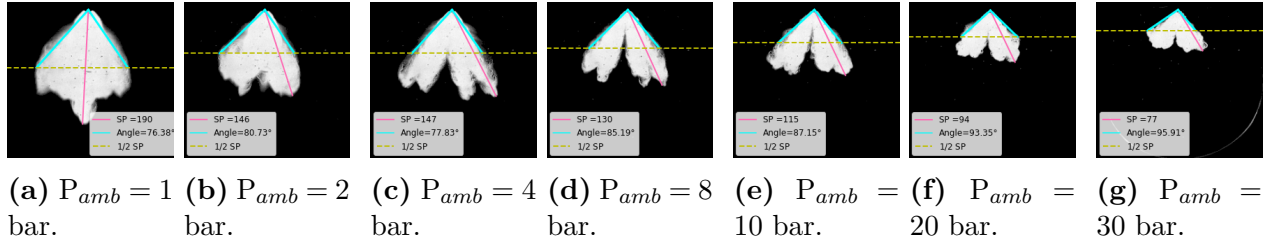


Figure 39: Example from the post-processing of the spray penetration length for an injection pressure of 200 bar at 0.25 ms after SOI, at different ambient pressures.

The measurements obtained through the post-processing of the images were used to create a plot of the spray penetration length. Figure 40a shows the measured spray penetration length for an injection pressure of 200 bar. Different chamber pressures are included as the different curves, portraying the spray propagation through the chamber. The plots become constant when reaching the end of the optical accessible window.

From the spray penetration length, the spray penetration velocity can be calculated. The results are shown in Figure 40b. The plots confirm what was observed from Table 6 and 7; the spray penetration velocity remained the highest for an ambient pressure of 1 bar, illustrated as the blue line, and the penetration velocity remained the lowest for an ambient pressure above the saturation pressure, such as 20 bar and 30 bar, illustrated as brown and pink curves, respectively.

From the velocity graph 40b: for the injections with an ambient pressure below the saturation pressure, meaning 1 bar, 2 bar, 4 bar and 8 bar, the velocity out of the injector is approximately the same: 140 m/s. As the chamber pressure increases to higher than the saturation pressure, the velocity out of the injector decreases. This is portrayed at time 0.0 ms in the plot. Consequently, an increase in the chamber pressure results in a shorter spray penetration, thus, a lower spray penetration velocity.

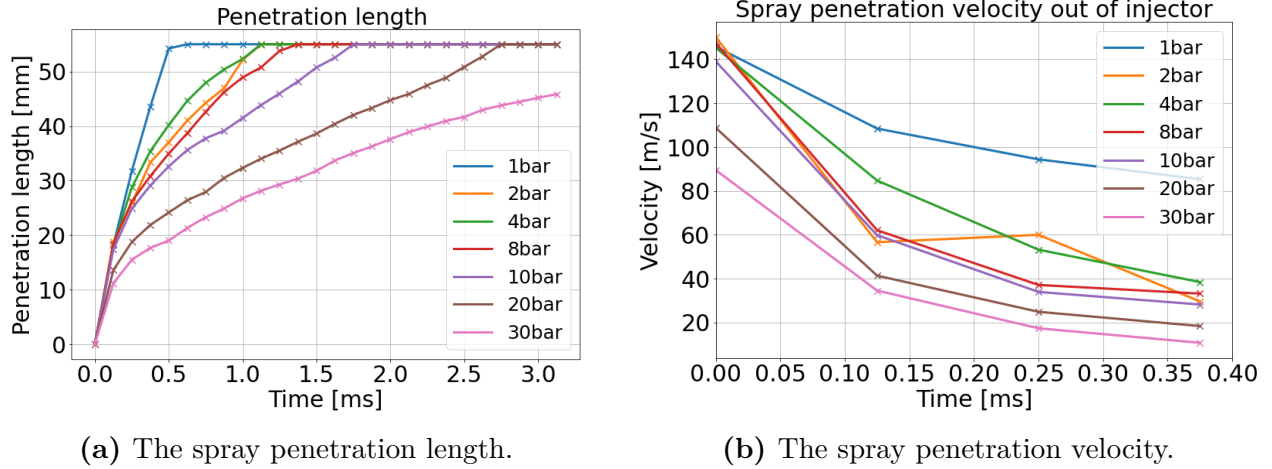


Figure 40: The spray penetration length and velocity of ammonia at different ambient pressures for an injection pressure of 200 bar.

An explanation for this occurrence can be related to the increased chamber pressure leading to a higher chamber density, which results in a larger drag force that obstructs the spray propagation. A similar occurrence has been reported in [42], as increasing chamber pressure leads to a decrease in spray penetration length. This also strengthens the possible explanation for the increase in delay related to the increase in ambient pressure in Section 4.3.4; the velocity of the spray decreases when the ambient pressure increases.

As noted above, the velocity out of the injector remains close to constant for ambient pressures ranging from 1 bar to 8 bar: at 140 m/s. However, from the Bernoulli equation, the theoretical velocity out of the injector is proportional to the change in pressure (repeating Equation 13):

$$u_{th} = \sqrt{\frac{2\Delta P}{\rho_l}} \implies u_{th} \propto \sqrt{\Delta P} \quad (21)$$

The actual spray velocities remain constant at higher pressure drops across the nozzle for ambient pressures below the saturation pressure, which can imply cavitation behaviour. Accordingly, the cavitation behaviour makes the velocity out of the nozzle appear independent of the pressure drop. A deeper investigation into the mass flows at ambient pressures ranging from 1 bar to 8 bar could be of interest to confirm this notion.

From Figure 40a and 40b, the orange line represents the spray propagation for an ambient pressure of 2 bar. As seen from the plots, the spray penetration velocity curve behaves

differently for 2 bar, having a lower velocity than 4 bar between 0.0 ms and 0.225 ms after SOI, then a higher velocity between 0.225 ms and 0.30 ms after SOI, before again declining. A possible explanation for this occurrence can be connected to the shape of the spray, referring to Table 6. While a chamber pressure of 4 bar results in defined spray jets, a chamber pressure of 2 bar presents a more collapsed spray shape. As the spray jets are more defined for an ambient pressure of 4 bar, this provides a more constant spray propagation. For an ambient pressure of 2 bar, as the spray distinctly collapses, this may provide a more inconsistent measurement of the spray propagation, hence giving a more inconsistent spray penetration length and velocity in the plot. This occurrence is especially clear in the spray penetration velocity plot in Figure 40b, resulting in a different behaviour of the curve.

This explanation can be inspected by reviewing the spray penetration length for the ambient pressures of 2 bar and 4 bar. Pictures from the post-processing are shown in Figure 41, comparing the spray penetration length at different points after SOI. In the pictures, the length scale is in pixel-lengths instead of mm for higher accuracy, where 1 pixel-length is equal to 0.244 mm. In the figure, two images for each chamber pressure are included; 0.13 ms and 0.25 after SOI. As illustrated in Figure 41a and 41c, at 0.13 ms after SOI, the spray penetration length for $P_{amb} = 4$ bar is slightly higher than for $P_{amb} = 2$ bar. This indicates the spray penetration velocity is slightly higher for an ambient pressure of 4 bar than 2 bar at this instant. However, at 0.25 ms after SOI, portrayed in Figures 41b and 41d, the penetration lengths are approximately the same, meaning the spray penetration velocity at an ambient pressure of 2 bar is higher during this period. This occurrence can explain the spike in the spray penetration velocity graph in Figure 40b.

Considering only five images were taken of each condition, there are uncertainties to this tendency. However, observing from the penetration plot in Figure 40a, the penetration length is comparable for both an ambient pressure of 2 and 4 bar. Hence, a conclusion can be drawn; the transitional flashing sprays give a comparable spray penetration.

Fang et al. [43] measured the liquid penetration of ammonia at 1 bar, 10 bar, 20 bar, 30 bar and 40 bar under an injection pressure of 500 bar. In this article, for an ambient pressure of 1 bar, the initial spray penetration propagation was much lower than for the remaining ambient pressures. Accordingly, different from the results obtained in this thesis, where a chamber

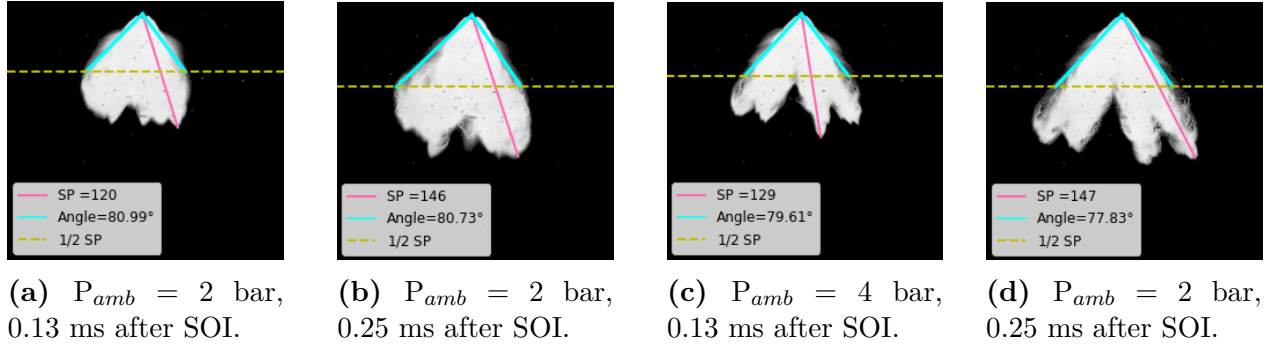


Figure 41: Illustration of the spray post-processing, for chamber pressures of 2 bar and 4 bar, at 0.13 ms and 0.25 ms after SOI. In the pictures, to achieve a higher sensitivity of the spray penetration length, the length has the unit of pixel lengths.

pressure of 1 bar resulted in the highest initial penetration velocity. However, the injector type employed in the article was a single-hole diesel injector. Having a different type of injector combined with a different injection pressure may account for the difference in results for the initiation of the injection. Nevertheless, after approximately 0.3 ms, the penetration of 1 bar surpassed the remaining ambient pressures, resulting in a similar tendency as the results presented in Figure 40a.

There are some uncertainties to the results presented on the spray penetration length. The pictures captured of the spray show the spray propagation in two dimensions. However, as mentioned in Table 2, each of the nozzle holes has an angle out of the injector. Consequently, the spray jets that exit the injector are turned in different directions, meaning the camera is not faced perpendicular to the jets. Accordingly, when analyzing the penetration length, the longest penetration length can be in the plane toward the camera, hence not visible in the imaging.

4.6.3 Angle of spray out of injector

Analyzing the spray angle out of the injector can give an indication of how the spray emerges out of the injector and how the ammonia allocates in the chamber under different conditions.

Figure 42 depicts an example from the post-processing of the angle of the spray out of the injector at an injection pressure of 200 bar, referring to Table 6. The images show the spray at the same instant, 3 ms after SOI, at different ambient pressures.

As observed in Table 6 and 7, the spray characteristics of ammonia are much dependent

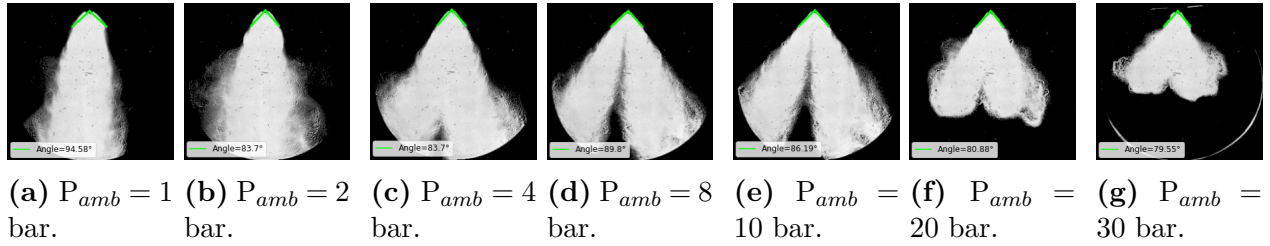


Figure 42: Example from the post-processing of the angle of the spray near the injector at an injection pressure of 200 bar at 3.0 ms after SOI, at different ambient pressures.

on the ambient pressure. Figure 43 portrays the angle of the spray near the injector (y-axis), with the ambient pressure (x-axis). These figures were included to examine if there were any correspondences between the pressure in the chamber and the angle out of the injector. In the figures, three curves are included, depicting the angles at three different moments: 1 ms, 3 ms and 5 ms after SOI, with the variance in the measurements presented in the background of the plot. Figure 43a shows the angle of the spray at an injection pressure of 100 bar, while 43b shows the angle of the spray at an injection pressure of 200 bar. The figures illustrate the same tendency, showing a relatively adequate correspondence between the two injection pressures.

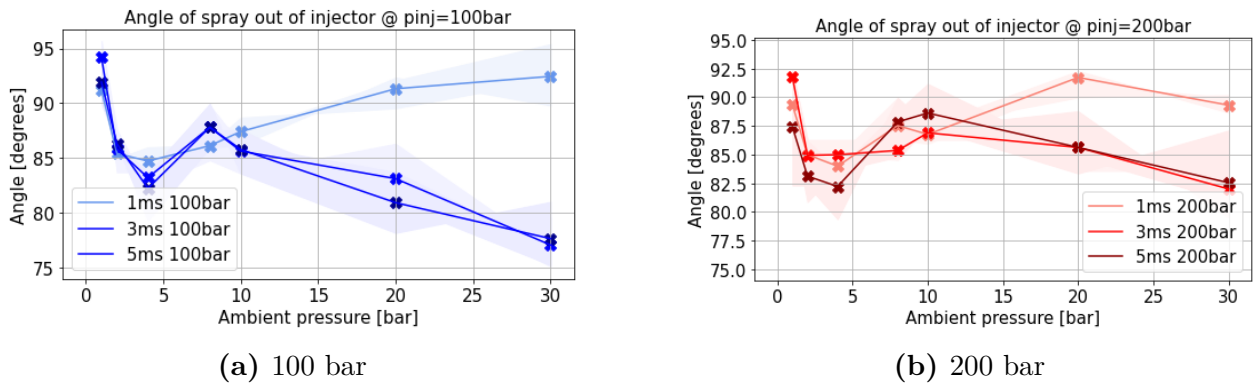


Figure 43: Graphs representing the spray angle near the injector. Here, the x-axis shows the ambient pressure, the y-axis is the angle in degrees. The three graphs represent the angles for different moments of the injection, 1 ms, 3 ms and 5 ms after the start of injection.

First, looking at the curve for 1 ms after SOI in Figure 43. The spray angle increases for an increasing chamber pressure (with the exception of an ambient pressure of 1 bar). This can be explained by the increasing chamber density obstructing the initial spray propagation, where the bigger angle can indicate a bigger obstruction in the chamber.

However, as the spray propagates through the chamber, the angle of the spray out of the injector significantly decreases for higher chamber densities. This can be observed by the curves of 3 ms and 5 ms at ambient pressures of 20 bar and 30 bar. An explanation for this can be connected to the spray penetration length in Figure 40a, where there is an exponential increase in the penetration length up to 1 ms after SOI, before the curve adjusts to a linear increase. An explanation can be that the spray takes some time to stabilize once the needle is opened, before adjusting to a linear, stable behaviour.

However, the spray angle of 1 bar is an exception, remaining high for all measurements. This phenomenon can be explained by the spray being in a fully flashing condition, resulting in a wider spray area out of the injector due to more vapour in the spray.

There is also a significant increase in spray angle at the ambient pressure of 8 bar. This can be explained by the spray being in critical flashing condition. A similar tendency was found by Pele et al. in article [1], where it was noted the spray angle at half penetration length was maximum at the saturation pressure of ammonia. However, this slightly deviates from the findings here, as it was found the angle near the injector was maximum at the saturation pressure, with the exception of the angle at the ambient pressure of 1 bar.

The spray penetration length and spray angles calculated are much dependent on the definition of the angle measurement. Examples of definitions; how much of the vapour zone is included in the measurements, how the spray penetration length is defined, and at what location of the spray is the angle measurement. Accordingly, this can provide uncertainties when comparing the results acquired with other studies.

4.6.4 Spray angle at half penetration length

The stages of flashing of ammonia spray can also be analyzed by evaluating the spray angle at half penetration length. Four ambient pressure were chosen to emphasise the changes in spray angle connected to the different flash boiling conditions: 1 bar was chosen to portray a fully flashing condition, 4 bar to show the transitional flashing condition, 8 bar to portray the initial flashing and 30 bar to portray the behaviour at a high chamber density. Figure 44 portrays the spray angle at half penetration length for these conditions, for time after SOI in ms. In the figure, the variance is shown in the background of the plot, the average of the

measurements is shown as the cross-points, while an IIR filter has been employed to present the tendency of the spray angle more clearly.

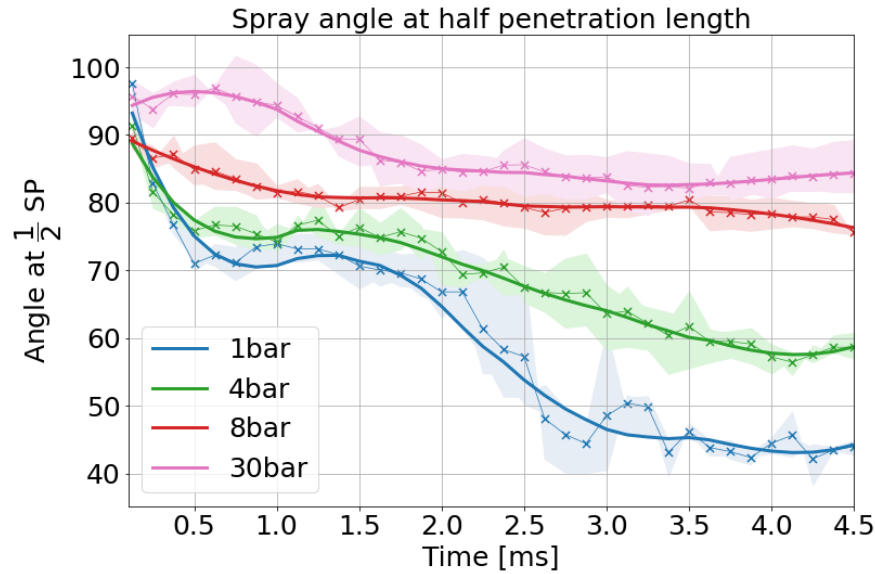


Figure 44: Spray angle at half penetration length at an injection pressure of 200 bar. The actual measurements in the background of the plots.

From Figure 44, it is observed that higher chamber densities result in higher spray angles at half penetration length.

The smallest spray angle is observed for a chamber pressure for the fully flashing condition, here implying 1 bar. From the graph, it is noted a significant declination from 1.5 ms to 3.0 ms after SOI. This declination is related to the liquid-vapour zone surrounding the liquid core being included in the angle measurement before the vapour zone gradually lessens with the spray propagation. This can be observed in Table 6 by looking at the ambient pressure of 1 bar at 1 ms and 3 ms after SOI. At 1 ms, the liquid-vapour zone (appearing as a cloud) is substantial, while at 3 ms, this vapour zone has almost vanished. As the zone is included in the angle measurements, it has an impact on the spray angle result of 1 bar.

There is also observed a fluctuating tendency of the measurements from 2.5 ms to 4.5 ms after SOI, for an ambient pressure of 1 bar. This is shown in the background of the plot in Figure 44. The explanation for this fluctuation tendency is related to the vapour zone surrounding the liquid core periodically being registered due to the chosen pixel intensity (explained in the post-processing section).

This fluctuating tendency can be demonstrated by reviewing the post-processed images. Figure 45 shows the spray at a chamber pressure of 1 bar with an injection pressure of 200 bar. In the Figure, the spray is depicted at different instances after SOI: showing how the vapour zone is first included in the measurements (in Figure 45a), then only the core of the spray (in Figure 45b), before vortices in the spray are included in the measurements (in Figure 45c), followed by only the core of the spray being included (in Figure 45d).

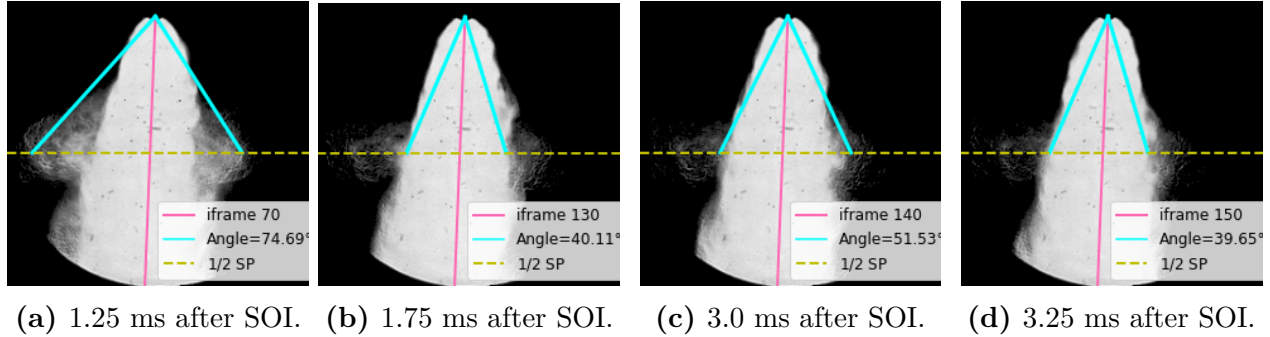


Figure 45: Pictures to explain the fluctuating tendency of the curve for fully flashing spray in Figure 44. The pictures portray the spray at a chamber pressure of 1 bar and injection pressure of 200 bar, displaying how the vapour zone with droplets surrounding the liquid core periodically gets detected in the script. The pictures are at different instants after the start of energizing, from 1.25 ms to 3.25 ms after SOI.

The spray angle at half penetration length for the transitional flashing region, meaning 4 bar, is marked as green in Figure 44. The curve is linearly decreasing, with the exception between 0.0 ms to 1.0 ms after SOI. Looking at Table 6 for an ambient pressure of 4 bar, this occurrence can be explained by the liquid-vapour zone surrounding the spray. This vapour zone with droplets is particularly visible at 0.25 ms after SOI, giving a higher angle measurement at this point. The spray collapses at 1.0 ms after SOI. As the spray is in a transition phase between 0.25 ms to 1.0 ms, the angle measurements become non-linear, resulting in a dip in the spray angle at 0.75 ms. From 1.25 ms after SOI, the angle again decreases, as can be observed in Table 6.

For the initial flashing, referring to an ambient pressure of 8 bar, the spray angle at half penetration remains close to constant, slightly linearly decreasing. Reviewing Table 6, this can be explained by the spray being close to the saturation pressure of ammonia. Hence, only initial flashing and less influenced by the vapour zone in comparison to the flare and

transitional flashing sprays.

An ambient pressure of 30 bar is shown as the pink graph in Figure 44. The spray angle at half penetration length is significantly higher in the beginning, having an apex at around 0.5 ms after SOI, before declining and stabilizing to a linear trend around 1.5 ms after SOI. An explanation for this tendency can be obtained by reviewing the Figure for spray penetration length, 40a. First, the penetration length is exponentially increasing before stabilizing at around 1 ms. The spray propagation takes some time to stabilize due to the higher chamber density, which obstructs the spray propagation and may influence the angle measurements during the same period.

From Figure 44, the spray angle at half penetration length appears dependent on the flashing conditions: a fully flashing spray gives a significantly lower angle measurement, for a spray close to the critical conditions, the spray angle decreases linearly, the transitional region appears in between the critical flashing and fully flashing, while the highest ambient density appears to obstruct the spray propagation, resulting in a more compressed spray and the highest angle at the half penetration length.

5 Conclusion

The test rig for momentum flux was successfully set up, and the optimum placement of the piezoelectric sensor was located. The results obtained confirmed the optimum placement to measure the momentum flux to be perpendicular to the spray. It was concluded that the location giving the most accurate measurement primarily depended on the angle between the plume and sensor, conditioned that the spray impingement area was significantly smaller than the target area. However, the distance between the spray target and injector was concluded to be more influential at elevated chamber densities.

The momentum flux, mass flow, instantaneous mass flow, discharge coefficient, spray shape, spray penetration length, spray penetration velocity and spray angle have been measured and examined.

The momentum flux was obtained using a force transducer and was observed to increase with increasing injection pressure while decreasing with an increased ambient density. Two consequences regarding delay were experienced: by increasing the chamber pressure, the injection period was slightly shortened. By decreasing the injection pressure, the injection period was slightly increased.

The injected mass was found by including a weight in the ammonia fuel system and was observed to be linearly increasing with the square root of the pressure difference and decreasing for higher ambient pressure. The instantaneous mass flow was acquired using a normalised form of the momentum flux measurement combined with measurements of the total mass injected. From the results obtained, an increase in the chamber pressure from 2 bar to 20 bar resulted in a decrease in the discharge coefficient from 0.56 to 0.51 for an injection pressure of 200 bar.

The spray behaviour out of the injector was captured using a shadowgraph imaging technique. The spray penetration length and velocity were found to be highly dependent on the chamber pressure, with an increasing ambient density resulting in a lower spray penetration velocity. Flash boiling conditions were found to influence the behaviour of the ammonia spray out of the injector. At a flare flashing condition, the shape of the spray changed significantly. The angle out of the injector was found to be dependent on the superheated properties and

showed an increasing tendency at the critical flashing pressure of ammonia. The spray angle at half penetration length was found to be dependent on the flashing condition, resulting in different shapes of the spray angle curve based on the flashing condition.

6 Further Work

For further work, some of the uncertainties for this thesis could be revised. A single-hole GDI would be valuable to validate the measurements of the six-hole GDI. The calculations in this thesis for each nozzle hole are based on geometry; hence a validation of the results is desired. Attempts at acquiring a single-hole GDI were made by delivering the injector for processing at two different establishments. The technique attempted was laser welding, which led to the injector needle being unable to shut. Hence, exploring a method without a heating device could be attempted.

Additionally, having a single-hole GDI could improve shadowgraph imaging. The injector could be orientated with the nozzle hole facing downwards. Accordingly, the spray would be perpendicular to the camera lens, thus, minimising the uncertainty in the measurements by not having a more significant portion of the spray propagating toward the camera. By employing a single-hole GDI for the shadowgraph imaging, the spray jets would not overlap; hence, more information would also be obtained from the imaging.

Applying a secondary imaging technique would be interesting for further optical investigations of the ammonia spray. Combining techniques for exclusively capturing the liquid of the spray with techniques capturing both the liquid and vapour could prove helpful in gaining additional insight into the spray behaviour. Accordingly, an estimate of the liquid ratio of the spray at different conditions would be achieved. Combining the current setup, a flow visualisation imaging technique, with an imaging technique that only captures the liquid could be executed. A higher sensitivity of the vapour phase could also be acquired by narrowing the pin-hole in the current optical setup. Additionally, considering the optical measurements in this thesis are based on five images in each condition for each injection duration, a further optical investigation into the spray would be advantageous to verify the results obtained.

The temperature of the injector tip during injections remains unknown. Including a thermal camera in the setup could be beneficial to acquire information on how significant the cooling is, and if this cooling has any effect on the flow through the injector. This could be conducted to confirm the measurements of the injected mass and possibly explain why two

injectors started leaking during the injected mass experiments.

As the mass flow rate at pressures between 2 bar and 10 bar is unknown, it remains unknown when the mass flow collapses. Consequently, inspecting the mass flow at ambient pressures between 2 bar and 10 bar would be interesting. Moreover, employing a transparent nozzle would be advantageous to reveal any cavitation behaviour in the nozzle.

It would be beneficial to introduce a universally utilized fuel, like iso-octane, into the injector to serve as a reference for analyzing the performance characteristics of ammonia when injected from the same injector under identical operating conditions.

For future work, comparing the results obtained from the experiments to the numerical simulations performed by the group would be beneficial, where the experimental results can be used to validate the simulations.

References

- [1] R. Pelé; C. Mounaïm-Rousselle; P. Bréquigny; C. Hespel; J. Bellettre. First study on ammonia spray characteristics with a current GDI engine injector. *Fuels* 2021, 2021. DOI <https://doi.org/10.3390/fuels2030015>, Last accessed: 03.04.2023.
- [2] R. Payri; J. Gimeno; P. Marti-Aldaravi; D. Vaquerizo. Internal flow characterization on an ecn gdi injector. *Experimental Techniques*, 2003. DOI [10.1615/AtomizSpr.2015013930](https://doi.org/10.1615/AtomizSpr.2015013930), Last accessed: 11.04.2023.
- [3] H. Blanco; E. Taib; D. Gielen; R. Roesch; C. Fernandez et al. Global hydrogen trade to meet the 1.5°C climate goal - part ii: Technology review of hydrogen carriers. *International Renewable Energy Agency (IRENA)*, 2022. URL <https://www.irena.org/publications/2022/Apr/Global-hydrogen-trade-Part-II>, Last accessed: 11.12.2022.
- [4] LR award mitsui with approval in principle for ammonia-fuelled gas carrier. *Lloyd's Register*, 2023. URL <https://www.lr.org/en/latest-news/lr-aip-for-mitsui-ammonia-carrier/>, Last accessed: 23.05.2023.
- [5] MI News Network. Maritime consortium completes ammonia co-firing test using ammonia-fueled engine. *Marine Insight*, 2023. URL <https://www.marineinsight.com/shipping-news/maritime-consortium-completes-ammonia-co-firing-test-using-ammonia-fueled-engine/>, Last accessed: 23.05.2023.
- [6] A. Habibic. New range of injection systems for low-carbon fuels in the making. *Offshore energy*, 2023. URL <https://www.offshore-energy.biz/new-range-of-injection-systems-for-low-carbon-fuels-in-the-making/>, Last accessed: 23.05.2023.
- [7] E. Nadimi; G. Przybyła; M. T. Lewandowski; W. Adamczyk. Effects of ammonia on combustion, emissions, and performance of the ammonia/diesel dual-fuel compression

- ignition engine. *Journal of the Energy Institute*, 2023. DOI <https://doi.org/10.1016/j.joei.2022.101158>, Last accessed: 23.05.2023.
- [8] D. Zhu; B. Shu. Recent progress on combustion characteristics of ammonia-based fuel blends and their potential in internal combustion engines. *International Journal of Automotive Manufacturing and Materials*, 2023. DOI <https://doi.org/10.53941/ijamm0201001>, Last accessed: 23.05.2023.
- [9] K.O. Bjørgen; N. Borsheim; T. Løvås. Momentum flux measurements of liquid injection of ammonia using a GDI injector. *11th European Combustion Meeting 2023*, 2023. URL https://www.researchgate.net/publication/370444698_Momentum_Flux_Measurements_of_Liquid_Injection_of_Ammonia_using_a_GDI_Injector, Last accessed: 23.05.2023.
- [10] N. Borsheim. Ammonia spray characterization. Project work, NTNU, 2022. Internal Report.
- [11] Understanding the differences in pfi and gdi engines. *Innospec*, 2022. URL <https://innospec.com/fuel-additives/understanding-the-difference-between-gdi-and-pfi-engines/>, Last accessed: 11.12.2022.
- [12] H. Brinks; E. A. Hektor. Ammonia as a marine fuel. *DNV*, 2020. URL <https://www.dnv.com/Publications/ammonia-as-a-marine-fuel-191385>, Last accessed: 01.06.2023.
- [13] A. Montanaro; L. Allocca; M. Lazzaro. Iso-octane spray from a gdi multi-hole injector under non- and flash boiling conditions. 10 2017. DOI <https://doi.org/10.4271/2017-01-2319>, Last accessed: 01.06.2023.
- [14] Y. Chen; Z. Zhang. Mechanism of flash boiling and spray analysis with gasoline, iso-octane, n-pentane and ethanol from a novel heated tip gdi injector. *Applied Thermal Engineering*, 115, 01 2017. DOI <https://doi.org/10.1016/j.applthermaleng.2016.12.101>, Last accessed: 01.06.2023.

- [15] K.L. Tay; W. Yang; S.K. Chou; D. Zhou; J. Li; W. Yu; F. Zhao; B. Mohan. Effects of injection timing and pilot fuel on the combustion of a kerosene-diesel/ammonia dual fuel engine: A numerical study. *Energy Procedia*, 105:4621–4626, 2017. DOI <https://doi.org/10.1016/j.egypro.2017.03.1002>, Last accessed: 23.05.2023.
- [16] Ammonia - vapour pressure at gas-liquid equilibrium. *The Engineering ToolBox*, 2023. URL https://www.engineeringtoolbox.com/ammonia-pressure-temperature-d_361.html, Last accessed: 23.05.2023.
- [17] S. C. Gad. Diesel fuel. In Philip Wexler, editor, *Encyclopedia of Toxicology (Second Edition)*, pages 19–22. Elsevier, New York, second edition edition, 2005. DOI <https://doi.org/10.1016/B0-12-369400-0/00320-3>, Last accessed: 01.06.2023.
- [18] Isooctane (marukasol 8). *Chemistry Maruzen Petrochemical CO*, 2023. URL https://www.chemiway.co.jp/en/product/data/i_data01.html, Last accessed: 01.06.2023.
- [19] W. Cornelius; L. W. Huellmantel; H. R. Mitchell. Ammonia as an engine fuel. *SAE Transactions*, 74:300–326, 1966. URL <https://www.jstor.org/stable/44460524>, Last accessed: 08.06.2023.
- [20] D. Lanni; E. Galloni; G. Fontana; G D’Antuono. Assessment of the operation of an si engine fueled with ammonia. *Energies*, 2022. URL <https://doi.org/10.3390/en15228583>, Last accessed: 19.04.2023.
- [21] C. S. Mørch; A. Bjerre; M. P. Gøttrup; S. C. Sorenson; J. Schramm. Ammonia/hydrogen mixtures in an SI-engine: Engine performance and analysis of a proposed fuel system. *Fuel*, 2011. DOI <https://doi.org/10.1016/j.fuel.2010.09.042>, Last accessed: 02.06.2023.
- [22] K. Ryu; G. E. Zacharakis-Jutz; S.-C. Kong. Ammonia/hydrogen mixtures in an si-engine: Engine performance and analysis of a proposed fuel system. *Applied Energy*, Pages: 206-215, 2014. DOI <https://doi.org/10.1016/j.apenergy.2013.11.067>, Last accessed: 19.12.2022.

- [23] J. Gaucherand; C. Netzer; M. T. Lewandowski; T. Løvås. Modelling of liquid injection of ammonia in a direct injector using reynolds-averaged navier–stokes simulation. *Scandinavian Simulation Society*, 2022. DOI <https://doi.org/10.3384/ecp192058>, Last accessed: 11.12.2022.
- [24] E. Nadimi; G. Przybyła; D. Emberson; T. Løvås; L. Ziółkowski; W. Adamczyk. Effects of using ammonia as a primary fuel on engine performance and emissions in an ammonia/biodiesel dual-fuel CI engine. *International journal of energy research*, 2022. DOI <https://doi.org/10.1002/er.8235>, Last accessed: 04.02.2023.
- [25] A. Valera-Medina; H. Xiao; M. Owen-Jones; W.I.F.David; P.J.Bowen. Ammonia for power. *Progress in Energy and Combustion Science*, 2018. DOI <https://doi.org/10.1016/j.pecs.2018.07.001>, Last accessed: 12.04.2023.
- [26] A.J. Reiter; S.-C. Kong. Diesel engine operation using ammonia as a carbon-free fuel. *Internal Combustion Engine Division Fall Technical Conference*, 2010. URL <https://doi.org/10.1002/er.8235>, Last accessed: 19.12.2022.
- [27] N. Raeie; S. Emami; O.K. Sadaghiyani. Effects of injection timing, before and after top dead center on the propulsion and power in a diesel engine. *Propulsion and Power Research*, 3(2):59–67, 2014. DOI <https://doi.org/10.1016/j.jprr.2014.06.001>, Last accessed: 23.05.2023.
- [28] H. A. Dhahad; M. A. Fayad; M. T. Chaichan; A.A. Jaber; T. Megaritis. Influence of fuel injection timing strategies on performance, combustion, emissions and particulate matter characteristics fueled with rapeseed methyl ester in modern diesel engine. *Fuel*, 306:121589, 2021. DOI <https://doi.org/10.1016/j.fuel.2021.121589>, Last accessed: 23.05.2023.
- [29] R. Payri; J.M. Garcia; F.J. Salvador; J. Gimeno. Using spray momentum flux measurements to understand the influence of diesel nozzle geometry on spray characteristics. *FuelFirst*, 2004. DOI <https://doi.org/10.1016/j.fuel.2004.10.009>, Last accessed: 17.04.2023.

- [30] B. Mohan; W. Yang; S. Chou. Cavitation in injector nozzle holes - a parametric study. *Taylor and Francis Group*, 2014. DOI <https://doi.org/10.1080/19942060.2014.11015498>, Last accessed: 11.12.2022.
- [31] S. Li; T. Li; N. Wang; X. Zhou; R. Chen; P. Yi. An investigation on near-field and far-field characteristics of superheated ammonia spray. *Fuel*, 324:124683, 2022. DOI <https://doi.org/10.1016/j.fuel.2022.124683>, Last accessed: 01.06.2023.
- [32] C. Mengzhao; L. Ziyong; P. Sungwook; P. Suhan. Characteristics of flash boiling and its effects on spray behavior in gasoline direct injection injectors: A review. *Fuel*, 271:117600, 2020. DOI <https://doi.org/10.1016/j.fuel.2020.117600>, Last accessed: 01.06.2023.
- [33] D.R. Emberson; B. Ihracska; S. Imran; A. Diez; M. Lancaster; T. Korakianitis. Hydraulic characterization of diesel and water emulsions using momentum flux. *Fuel*, 2015. DOI <https://doi.org/10.1016/j.fuel.2015.08.016>, Last accessed: 23.05.2023.
- [34] R. Payri; G. Bracho; P. Martí-Aldaraví; A. Moreno. Using momentum flux measurements to determine the injection rate of a commercial urea water solution injector. *Flow Measurement and Instrumentation*, 80:101999, 2021. DOI <https://doi.org/10.1016/j.flowmeasinst.2021.101999>, Last accessed: 01.06.2023.
- [35] M. Dowling; M. Penfold; J. Faber; J. Király; R. van der Ven; E. Pang; A. van Grinsven R. Laursen; D. Barcarolo; H. Patel. Potential of ammonia as fuel in shipping. *European Maritime Safety Agency (2022), Update on potential of biofuels in shipping, EMSA, Lisbon*, 16.09.2022. URL <https://www.emsa.europa.eu/publications/item/4833-potential-of-ammonia-as-fuel-in-shipping.html>, Last accessed: 11.04.2023.
- [36] L. Schulster; R. Y.W. Chinn. Guidelines for environmental infection control in health-care facilities. *Centers for Disease Control and Prevention*, 2003. URL <https://www.cdc.gov/infectioncontrol/guidelines/environmental/background/air.html>, Last accessed: 08.05.2023.

- [37] Mary Elizabeth. What is frame rate? URL <https://www.easytechjunkie.com/what-is-frame-rate.htm>. Last accessed: 07.12.2022.
- [38] Photron. Product datasheet Nova S. URL <https://photron.com/fastcam-nova-s/>. Last accessed: 07.12.2022.
- [39] D. E. Knuth. About shutter speed. *Illustrated Photography*, Archived 18.06.2016. URL <https://web.archive.org/web/20160618082252/http://www.illustratedphotography.net/basic-photography/understanding-shutter-speed>, Last accessed: 07.12.2022.
- [40] Scipy signal savgol filter. *SciPy documentation*, 2022. URL https://docs.scipy.org/doc/scipy/reference/generated/scipy.signal.savgol_filter.html, Last accessed: 11.12.2022.
- [41] What is laser welding and how does it work? URL <https://www.twi-global.com/technical-knowledge/faqs/faq-how-does-laser-welding-work>. Last accessed: 12.12.2022.
- [42] C. Qiang; K. Ojanen; Y. Diao; O. Kaario; M. Larimi. Dynamics of the ammonia spray using high-speed schlieren imaging. volume 4, 03 2022. DOI <https://doi.org/10.4271/2022-01-0053>, Last accessed: 01.06.2023.
- [43] Y. Fang; X. Ma; Y. Zhang; Y. Li; K. Zhang; C. Jiang; Z. Wang; S. Shuai. Experimental investigation of high-pressure liquid ammonia injection under non-flash boiling and flash boiling conditions. *Energies*, 16(6), 2023. DOI <https://doi.org/10.3390/en16062843>, Last accessed: 01.06.2023.

A Appendix

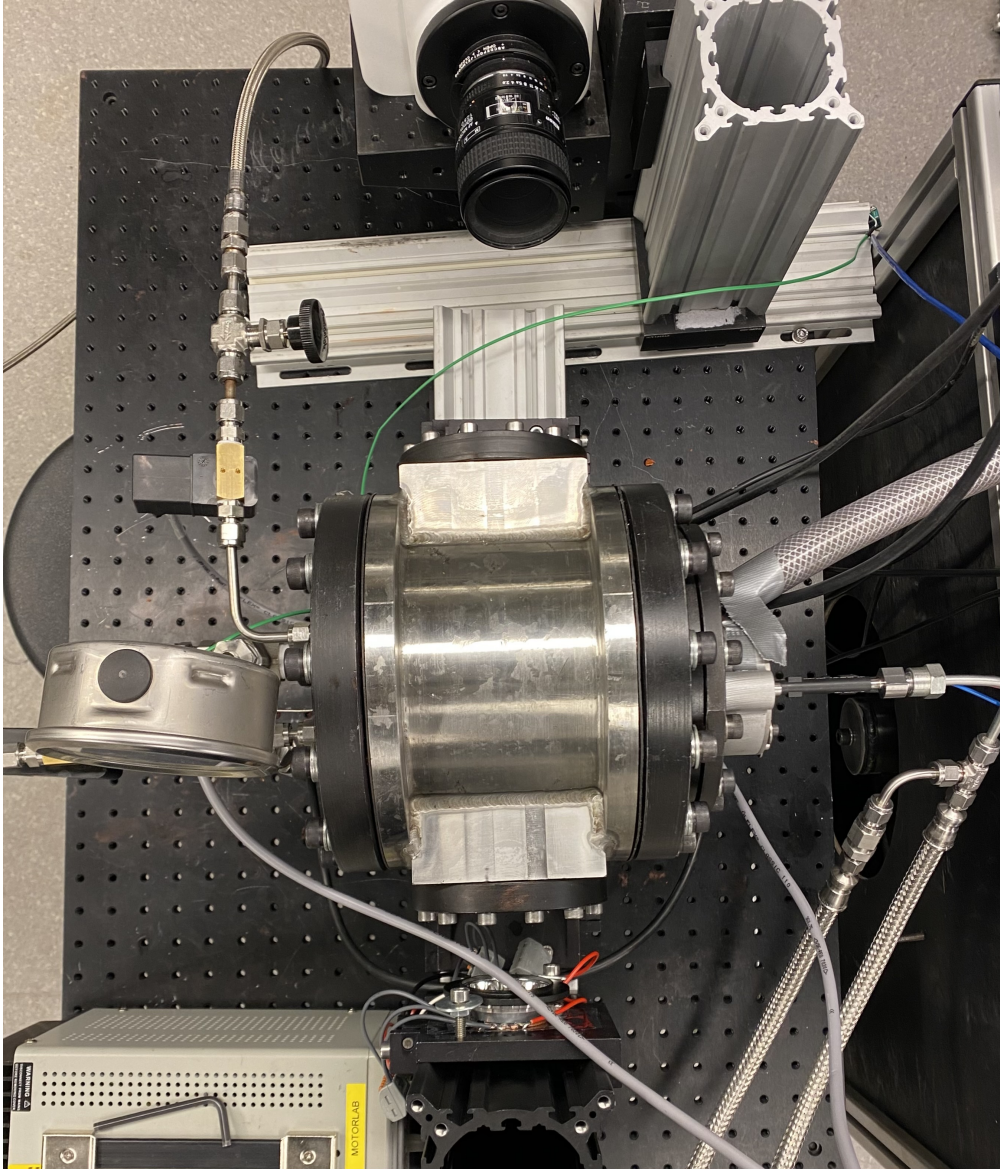


Figure 46: Picture of the high-pressure chamber during the momentum flux testing. Showing the position of the camera and the LED light.

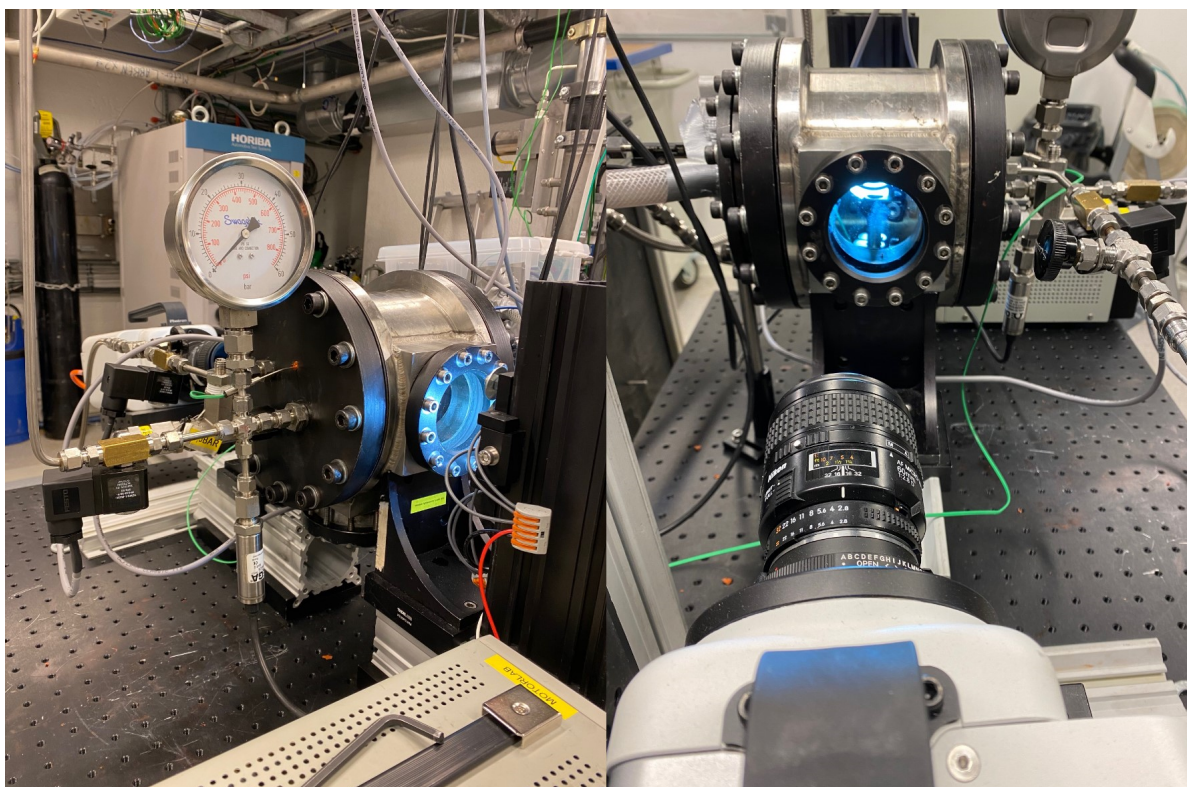


Figure 47: Picture of the high-pressure chamber during the momentum flux testing. Showing the position of the camera and the LED light.



Figure 48: Pictures of the cylindrical fuel tank on the weight (to the left), the ammonia supply tank (grey in the centre) and the nitrogen supply tanks (blue and black, to the right).

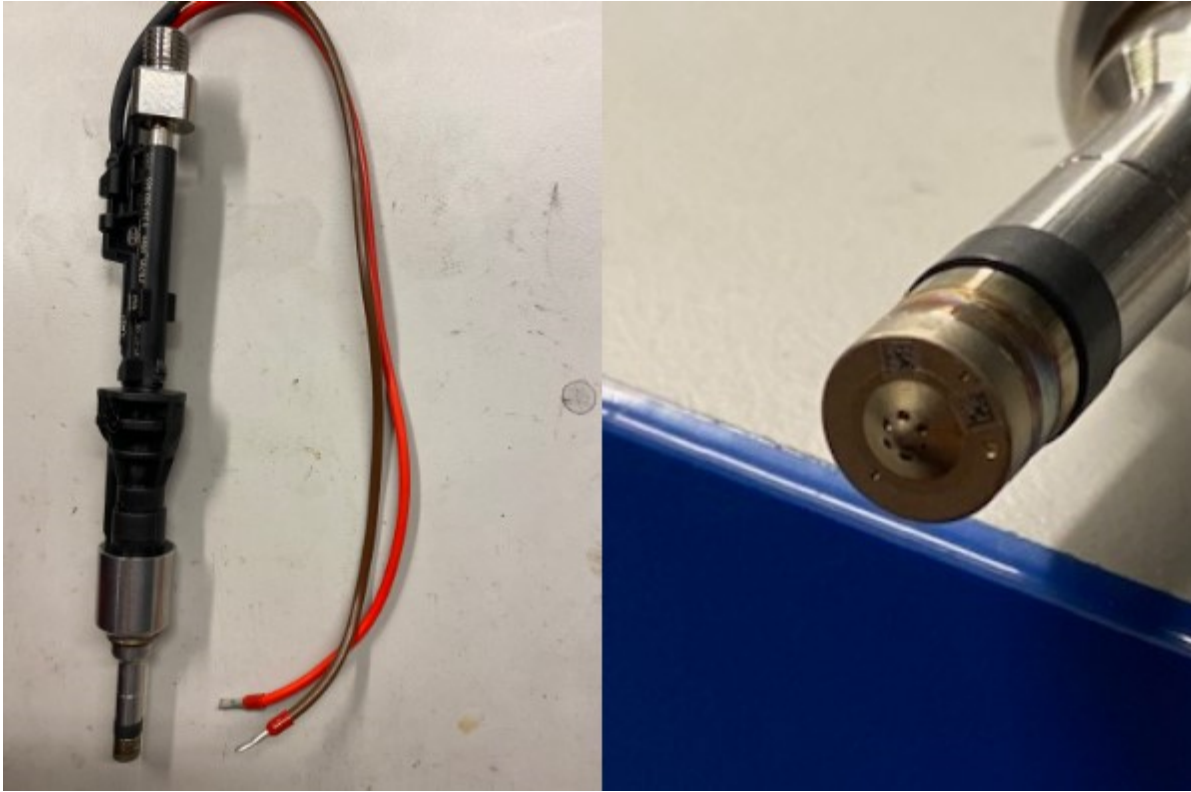


Figure 49: Pictures of the injector employed.



Figure 50: Picture of the different spray targets.

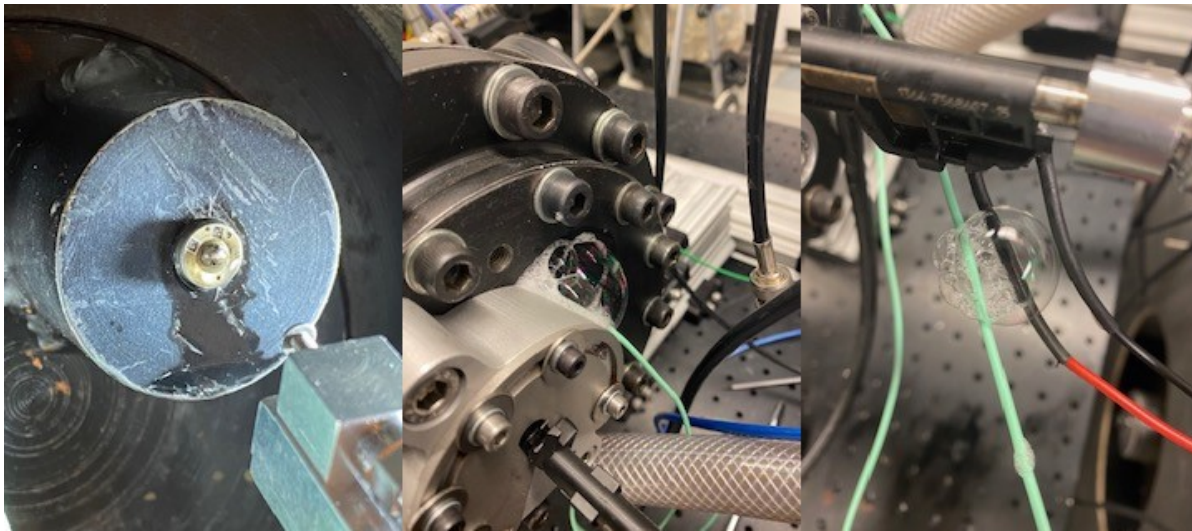
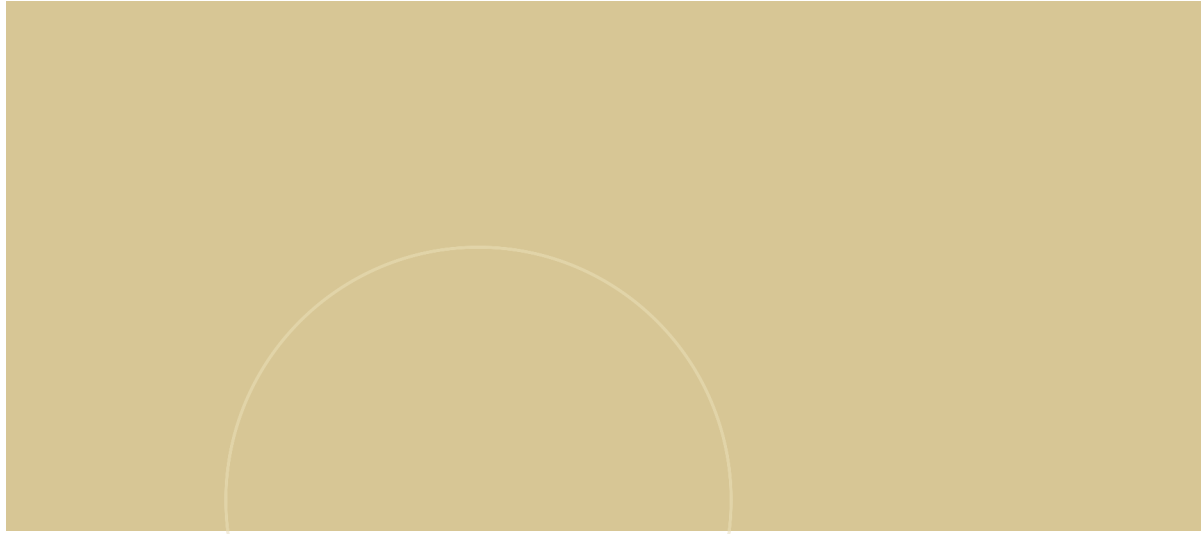


Figure 51: Pictures of some leakages that occurred during testing: a leakage from the single-hole GDI, an initial leakage from the high-pressure chamber (found by using soap water and later fixed), and a smaller leakage from the cable to the force transducer (found by using soap water).



 **NTNU**

Norwegian University of
Science and Technology